Novel Liquid Phase Routes for the Synthesis of Metal Sulphide Nanomaterials and Their Thin Films

A thesis submitted in fulfilment of the requirements for the degree of Doctor of Philosophy

Rhiannon Maree Clark

B. Sc. (Nanotechnology), RMIT University

B. Sc. (Applied Chemistry), RMIT University

School of Engineering

College of Science, Engineering and Health

RMIT University

August 2017

Novel Liquid Phase Routes for the Synthesis of Metal Sulphide Nanomaterials and Their Thin Films

Rhiannon Maree Clark, RMIT University

Declaration

I certify that except where due acknowledgement has been made, the work is that of the author alone; the work has not been submitted previously, in whole or in part, to qualify for any other academic award; the content of the thesis is the result of work which has been carried out since the official commencement date of the approved research program; any editorial work, paid or unpaid, carried out by a third party is acknowledged; and, ethics procedures and guidelines have been followed.

I acknowledge the support I have received for my research through the provision of an Australian Government Research Training Program Scholarship.

……..

Rhiannon Maree Clark

1st August 2017

Acknowledgements

This research would not have been possible without the amazing bunch of people involved or the funding provided by the Australian government and from the Commonwealth Scientific and Industrial Research Organisation (CSIRO).

Firstly, I would like to thank my senior supervisor Kourosh Kalantar-zadeh for giving me this opportunity. Your constant scientific input as well as advice and encouragement have gotten me to where I am today. I also appreciate the contributions from the other members of my supervisory team Ivan Cole, Kay Latham, Adrian Trinchi and Madhu Bhaskaran, who all offered their time and expertise at various stages throughout my candidature.

Special thanks to Torben Daeneke, who was often my first point of call when I needed advice about both science and life in general. He has been extremely generous, encouraging and helpful.

I would like to acknowledge the help of every one of my co-authors and other team members for their contributions to my work and their smiling faces on a day-to-day basis. I would particularly like to thank Emily Nguyen, Ben Carey, Chris Harrison and Paul Atkin, we were all in this together and there were plenty of days that I know I couldn't have gotten through alone.

To my family and friends outside the scientific community, thanks for not asking too many questions. Also thanks for providing distractions and keeping me sane.

Mum and Dad, you've been there for me every step of the way. Although you didn't completely understand what it was that I was actually trying to do, you never gave up believing that I could do it and that means the world to me.

It's been a long road. The start was hard, the middle was harder and the end was hardest. So, thank you all for helping me through.

Abstract of thesis

The unique properties exhibited by many metal sulphide nanomaterials have driven research interest in recent years. As new dimensionalities and morphologies continue to be isolated, a vast array of useful materials is discovered and their emerging applications are realised. Amongst these morphologies, two-dimensional transition metal dichalcogenides have gained significant attention. This PhD research focuses on some of the most important aspects of two-dimensional metal sulphides: their exfoliation, conversion of their dispersions into thin films and eventually enhancing their optical properties.

Due to the general dimension-dependent properties of layered metal sulphide crystals, it is important to have control over the thickness and lateral size during preparation of such two-dimensional nanosheets. Despite many past advances, there is still ample opportunity to develop improved exfoliation techniques, which becomes one of the main focuses of this research.

Traditionally, liquid-phase exfoliation of layered sulphide materials is performed using organic solvents, due to their surface energies providing superior nanoflake dispersibility. More recently, the use of surfactants has been established, to improve the nanoflake yield in alternative solvents. During this PhD research, the author established a new sonication-assisted biocompatible molybdenum disulphide (MoS_2) exfoliation technique using the bile salt, chenodeoxycholic acid, in a water-ethanol solution. The method was shown to produce high quality nanoflakes in a reasonable yield. A mechanically gentle, reductive exfoliation method was also explored for the synthesis of laterally large ultrathin nanosheets of MoS_2.

Following successful exfoliation of layered MoS_2, the method was then further explored to exfoliate quasi-stratified Bi_2S_3 crystals. The crystal structure of Bi_2S_3 comprises rows of stacked ribbons which are held together through van der Waals forces in two directions. The anisotropic structure favours the formation of one-dimensional nanomaterials and exfoliation of two-dimensional layers has not previously been demonstrated. As such, the work presented in this thesis introduces the first report of exfoliation of Bi_2S_3 into micron-scale ultrathin nanosheets as a novel step in creating planar structures from crystals that are not completely stratified. The lateral dimensions of the sheets were in the order of 10s of μm wide, with thickness reduced to one or two fundamental layers. The p-type nanosheets, which contained sulphur vacancies, were shown to be selectively sensitive to NO_2 gas, with a fast response attributed to strong physisorption.

Another area that requires research attention is the translation of suspended exfoliated metal sulphide nanoflakes into thin films; especially for the development of future functional systems. In most cases, techniques such as spin-coating and drop-casting are used to deposit suspended two-dimensional materials, resulting in films that are non-uniform and have poor coverage. A recent report outlines the treatment of exfoliated transition metal dichalcogenide nanoflakes with chemical modifiers, before injection into a pre-defined liquid-liquid interface, resulting in an assembled film. In this PhD research, the author explored a more efficient assembly process for exfoliated nanoflakes, where a liquid-liquid interface was established directly from the suspended particles without the addition of

any inducing agents. Advantageously, avoiding chemical processing reduced the influence on the properties of the nanoflakes in the resulting film.

Controlled deposition of thin films from assembled nanoflakes was also achieved through the use of hydrophobic patterned substrates. An efficient film assembly and dip coating of the substrates results in large-scale uniform patterned thin films of tungsten disulphide (WS_2) and MoS_2 nanoflakes. Composite films are also established through simply mixing two different nanoflake suspensions prior to the formation of the liquid-liquid interface. Film characterisation showed that the MoS_2 and WS_2 were evenly dispersed throughout the composite thin film, with no isolated regions of the individual materials.

One of the most promising properties of monolayer MoS_2 is that it displays photoluminescence, although the low emission is not ideal for practical optical applications. Extensive studies on quantum dot emission optimisation, through surface passivation, drew our attention to the possibility of incorporating MoS_2 into a hybrid structure to enhance its photoluminescence. Recent studied report composites of MoS_2 nanosheets with nanoparticle decoration, or stacked in layered heterostructures, but no hybrid quantum dots have been demonstrated.

In this thesis, the author presents the hydrothermal conversion of MoS_2 nanoflakes into quantum dots with simultaneous ZnS growth. The hybrid particles were found to have a narrow size distribution and enhanced photoluminescence quantum yield compared to the exfoliated nanoflakes. The emission was found to be excitation-wavelength-independent, which would make it easier to monitor their response in optical sensing applications. The developed water-stable hybrid quantum dots provide a biocompatible alternative to the traditional synthesis of toxic core-shell quantum dots in harsh organic solvents.

Overall, the author of this thesis believes that this research contributed to the advancement of nanotechnology through the development of several new morphologies of metal sulphides and added to the ever-growing body of knowledge in the field of two-dimensional materials.

Table of contents

List of figures

Abbreviations

2D	Two-dimensional
AFM	Atomic force microscopy
CDCA	Chenodeoxycholic acid
DLS	Dynamic light scattering
DMF	Dimethyl formamide
EBL	Electron beam lithography
EDX	Energy dispersive x-ray spectroscopy
FFT	Fast Fourier transform
HRTEM	High resolution transmission electron microscopy
I-V	Current-voltage
ODE	Octadecene
PESA	Photoelectron spectroscopy in air
PFDTES	1H, 1H, 2H, 2H-Perfluorodecyl triethoxysilane
PL	Photoluminescence
QDs	Quantum dots
SAED	Selected area electron diffraction
SEM	Scanning electron microscopy
TEM	Transmission electron microscopy

TMDs	Transition metal dichalcogenides
UV-vis	Ultraviolet-visible spectroscopy
XPS	X-ray photoelectron spectroscopy
XRD	X-ray diffraction

Chapter 1

Background

1.1 Motivation

Semiconductor nanomaterials show vastly different properties to their bulk counterparts and are thus highly researched for developing new functional materials and devices with a broad range of applications. There is vast scope for continued investigation of new nanomaterials, alternative morphologies, more efficient synthesis techniques and applications in emerging technologies.

1.1.1 Metal sulphides

Metal sulphides are a class of materials with a wide variety of crystal structures and properties. There are examples of metallic, insulating and semiconducting sulphides and thus, selection of a suitable metal sulphide material can assist in development of a huge variety of advanced systems.

In their native states, it is difficult to tune bulk metal sulphides and they have limited surface area to provide the needed functionalities. However, by manipulating the dimensions of a metal sulphide, we

can increase our ability to control the band structure and electronic properties of the resulting nanomaterials. Synthesis of metal sulphide nanomaterials is possible through many bottom-up and top-down approaches. Tailoring reaction conditions can result in variations to morphology, stoichiometry and crystal phase of the resulting nanocrystals. As such, vast possibilities are available to be explored.

1.1.2 Morphology

The crystal structure and phase of a metal sulphide determine the possible nanostructure morphologies available. An interesting property is the layered crystal structures of some sulphides provide the opportunity to exfoliate the crystal into freestanding monolayers. The most common example of a monolayer metal sulphide is molybdenum disulphide (MoS_2), which has been extensively studied in recent years.[1-4] Monolayer MoS_2 has an altered band structure arising from confinement to a two-dimensional structure. This band cross-over results in a direct bandgap, which gives rise to photoluminescent properties in the monolayer material.[1] Interesting and useful properties like this are the reason that the PhD candidate wishes to further explore the synthesis of new morphologies of various metal sulphides, in the hope of uncovering novel nanostructures.

Following the discovery of graphene, development of alternative two-dimensional materials has received much research attention.[3, 5] These atomically thin structures possess a huge surface area, which provides a platform for efficient environmental interaction. As such, there is potential for incorporation of two-dimensional nanomaterials into a variety of sensors, optical and electronic devices.

An extensively investigated metal sulphide morphology is zero-dimensional quantum dots. There have been many examples of useful applications developed through measuring the optical emission from particles, which occurs due to quantum confinement.[6-8] However, the vast majority of quantum dots are unstable in aqueous environments (requiring capping agents) and contain toxic elements such as cadmium and selenium. Further studies of biocompatible alternatives present another key area of investigation.

Another important consideration is the translation of the developed nanomaterials into useable formats. Deposition of the particles onto manageable substrates, in a controlled manner, is critical. Traditional techniques of particle deposition are usually inefficient and result in non-uniform films, with little control over the orientation of the particles. Predictable deposition would increase the ability to produce useful devices with electrode connections and also contribute to the ease of composite build-up through layering.

1.1.3 Composite nanomaterials

A booming field, which contributes to different properties and applications, is the incorporation of multiple materials into hybrid structures. Combinations of multiple nanomaterials result in a huge array of new structures with enhanced applicability through improved control over desired characteristics.

Core-shell quantum dots are one example of a hybrid nanostructure which has been extensively studied and explored for optimisation. The shelling process has been shown to protect the core and enhance the optical emission through passivation.[9]

In recent years, composite structures have been developed using two-dimensional nanoflakes as a base for nanoparticle growth.[10] Many combinations have been developed, with a variety of applications.[11] Layered heterostructures of stacked two-dimensional sheets have also been demonstrated to show enhanced electrical properties.[12]

As such, further investigation of new hybrid structures and incorporation of multiple materials into mixed films will continue to expand the range of useful composite nanomaterials.

1.1.4 Liquid-phase preparation

Both top-down and bottom-up approaches to nanomaterial synthesis are available, with various methods including reactive intercalation,[13-15] sonication-assisted exfoliation,[2, 16] mechanical exfoliation,[17] hydrothermal growth,[18] chemical vapour deposition[19] and chemical synthesis.[20]

Liquid-phase preparations of metal sulphides provide more control over the material dimensions and morphology. Liquid-phase methods are advantageous over chemical vapour deposition techniques because they can be achieved at relatively low temperature and result in suspensions which can be manipulated. Chemical functionalisation or incorporation into mixtures becomes possible when the nanomaterials are suspended in a solvent.

There is a remarkable amount of control over the dimensions and phase of the resulting sulphide nanomaterials when liquid-phase synthesis routes are used. By studying the effects of various reaction conditions, a material's properties can be carefully tailored to produce a desired combination to suit a specific application.

1.2 Objectives

After identifying potential areas for further development of the area of metal sulphide nanomaterials, the author was able to focus the scope of their PhD research. As such, the main focus areas were identified to be: the development of new morphologies of metal sulphide nanomaterials (i.e. hybrid structures and unique dimensionalities), implementation of more user-friendly interfaces (i.e. aqueous suspensions and deposited thin films), identification and exploitation of tuneable properties, and exploration of possible applications for the developed materials.

The first area of research is to develop a biocompatible synthesis route and achieve high quality sulphide materials with useful optical emission. Building on prior research which presents suitable solvents for high yield exfoliation of MoS_2, the author aims to avoid the use of harsh organic solvents. This project aims to successfully make use of a biocompatible surfactant in an aqueous environment, as the medium for the exfoliation reaction. The first research question is 'Can a biocompatible exfoliation process be developed, to produce high yield MoS_2 nanoflakes in a stable suspension?'. Further to this, a second biocompatible step will be explored, for the hydrothermal synthesis of zinc sulphide (ZnS). The role of the ZnS will be to enhance the optical emission from the MoS_2. The second research question is "How will the synthesis of a composite material change the optical properties of the exfoliated MoS_2 and can the photoluminescence quantum yield be increased?".

The next area of interest is to study the behaviour of the suspended nanomaterials and achieve a controlled method to manipulate their orientation. The third research question is “How can a controlled large-scale thin film deposition of exfoliated material be developed and can a patterned film be achieved?”. Substrate patterning, to form hydrophilic and hydrophobic domains, is a convenient way of controlling the behaviour of a liquid on a surface. However, further control over the concentration and packing arrangement of suspended particles is necessary to achieve patterned films. The aim of this stage of the research is to make use of a liquid-liquid interface as a trap for suspended particles, to form a uniform, densely-packed film of nanomaterial. The author of this PhD thesis then aims to extract this assembled film onto a patterned substrate, thus producing a controlled patterned uniform film. In addition, it is expected that this method can be extended to a range of metal sulphides, the author will also explore the incorporation of multiple materials into a mixed film.

In the final stage, the PhD candidate aims to explore efficient exfoliation techniques that produce large-scale ultrathin metal sulphides by reducing the mechanical forces which alter the crystal structure and reduce the size of the sheets. Reduced nanosheet size is a major issue resulting from harsh and energetic exfoliation techniques. In this work, optimisation of the nanosheet dimensions will be of high priority. The final research question is “Can a mechanically-gentle exfoliation be achieved, such that laterally large nanosheets are produced? Is it possible to extend this method to the exfoliation of quasi-stratified crystals into two-dimensional structures?”. The author aims to introduce a new reductive exfoliation method, which doesn’t fracture or alter the crystal phase of the resulting nanosheets. The mechanically gentle technique will be explored as a possible method for exfoliation of quasi-stratified crystals, which usually form one-dimensional nanostructures. Further to this, the large-area sheets will be incorporated into devices to test their electrical performance and response as gas sensors.

1.3 Outline of thesis

This thesis is primarily focussed on the investigation of new morphologies of metal sulphide nanomaterials, through the development of new liquid-phase synthesis methods. There will be an

emphasis on reducing processing times to present facile routes to efficiently produce a variety of high quality metal sulphide materials.

In Chapter 2, a thorough review of recent literature in relevant areas will be presented in such a way as to draw attention to the areas which lack fully developed concepts and present research gaps that will become the focus of this thesis.

Chapter 3 will cover the topic of biocompatible synthesis of hybrid quantum dots. The author will present a new hydrothermal synthesis method and fully characterises the morphology and optical properties of the products. A two-step route will be presented, to limit the thickness of the MoS_2 first, and then restrict the lateral dimensions whilst simultaneously growing a ZnS coating, to develop hybrid quantum dots.

The investigation of controlled particle deposition will be presented in Chapter 4. A facile assembly technique will be shown, using a liquid-liquid interface to control the particle orientation and film formation. A substrate patterning technique will be used to drive the particles into a uniform densely-packed film which covers pre-defined large scale areas. The technique will be demonstrated for the two most common transition metal disulphide materials, MoS_2 and WS_2. The method will also be tested for the formation of mixed structures, by incorporation of the two materials into a composite film.

In Chapter 5, the exfoliation of micron-scale two-dimensional metal sulphides will be presented. A new reductive exfoliation process will be developed, to avoid the use of mechanical agitation, thus preventing the nanosheets from being broken into smaller fragments. This method will be tested on different metal sulphide materials, to test its effectiveness, even when the structure of the bulk crystal is only quasi-stratified.

The overall conclusions and potential for extension to future studies will be presented in Chapter 6 of this thesis. The author will discuss potential for further refinement of the new synthesis methods, where applicable to other materials, as well as potential for applications of the current product metal sulphide nanomaterials.

1.4 References

1. Mak, K. F.; Lee, C.; Hone, J.; Shan, J.; Heinz, T. F. Atomically Thin MoS_2: A New Direct-Gap Semiconductor. *Phys. Rev. Lett.* **2010**, 105, 136805.

2. Coleman, J. N.; Lotya, M.; O'Neill, A.; Bergin, S. D.; King, P. J.; Khan, U.; Young, K.; Gaucher, A.; De, S.; Smith, R. J.; Shvets, I. V.; Arora, S. K.; Stanton, G.; Kim, H.-Y.; Lee, K.; Kim, G. T.; Duesberg, G. S.; Hallam, T.; Boland, J. J.; Wang, J. J.; Donegan, J. F.; Grunlan, J. C.; Moriarty, G.; Shmeliov, A.; Nicholls, R. J.; Perkins, J. M.; Grieveson, E. M.; Theuwissen, K.; McComb, D. W.; Nellist, P. D.; Nicolosi, V. Two-Dimensional Nanosheets Produced by Liquid Exfoliation of Layered Materials. *Science* **2011**, 331, 568-571.

3. Wang, Q. H.; Kalantar-Zadeh, K.; Kis, A.; Coleman, J. N.; Strano, M. S. Electronics and optoelectronics of two-dimensional transition metal dichalcogenides. *Nat. Nanotechnol.* **2012**, 7, 699-712.

4. Chhowalla, M.; Shin, H. S.; Eda, G.; Li, L. J.; Loh, K. P.; Zhang, H. The chemistry of two-dimensional layered transition metal dichalcogenide nanosheets. *Nat. Chem.* **2013**, 5, 263-275.

5. Butler, S. Z.; Hollen, S. M.; Cao, L. Y.; Cui, Y.; Gupta, J. A.; Gutierrez, H. R.; Heinz, T. F.; Hong, S. S.; Huang, J. X.; Ismach, A. F.; Johnston-Halperin, E.; Kuno, M.; Plashnitsa, V. V.; Robinson, R. D.; Ruoff, R. S.; Salahuddin, S.; Shan, J.; Shi, L.; Spencer, M. G.; Terrones, M.; Windl, W.; Goldberger, J. E. Progress, Challenges, and Opportunities in Two-Dimensional Materials Beyond Graphene. *ACS Nano* **2013**, 7, 2898-2926.

6. Bera, D.; Qian, L.; Tseng, T. K.; Holloway, P. H. Quantum Dots and Their Multimodal Applications: A Review. *Materials* **2010**, 3, 2260-2345.

7. Kim, J. Y.; Voznyy, O.; Zhitomirsky, D.; Sargent, E. H. 25th Anniversary Article: Colloidal Quantum Dot Materials and Devices: A Quarter-Century of Advances. *Adv. Mater.* **2013**, 25, 4986-5010.

8. Frasco, M. F.; Chaniotakis, N. Semiconductor quantum dots in chemical sensors and biosensors. *Sensors* **2009**, 9, 7266-7286.

9. Reiss, P.; Protiere, M.; Li, L. Core/Shell Semiconductor Nanocrystals. *Small* **2009**, 5, 154-168.

10. Cheng, Z. H.; He, B. Z.; Zhou, L. A general one-step approach for in situ decoration of MoS_2 nanosheets with inorganic nanoparticles. *J. Mater. Chem. A* **2015**, 3, 1042-1048.

11. Huang, X.; Tan, C. L.; Yin, Z. Y.; Zhang, H. 25th Anniversary Article: Hybrid Nanostructures Based on Two-Dimensional Nanomaterials. *Adv. Mater.* **2014**, 26, 2185-2204.

12. Gong, Y.; Lin, J.; Wang, X.; Shi, G.; Lei, S.; Lin, Z.; Zou, X.; Ye, G.; Vajtai, R.; Yakobson, B. I.; Terrones, H.; Terrones, M.; Tay, B K.; Lou, J.; Pantelides, S. T.; Liu, Z.; Zhou, W.; Ajayan, P. M. Vertical and in-plane heterostructures from WS_2/MoS_2 monolayers. *Nat. Mater.* **2014**, 13, 1135-1142.

13. Eda, G.; Yamaguchi, H.; Voiry, D.; Fujita, T.; Chen, M.; Chhowalla, M. Photoluminescence from Chemically Exfoliated MoS_2. *Nano Lett.* **2011**, 11, 5111-5116.

14. Ambrosi, A.; Sofer, Z.; Pumera, M. Lithium Intercalation Compound Dramatically Influences the Electrochemical Properties of Exfoliated MoS_2. *Small* **2015**, 11, 605-612.

15. Ren, L.; Qi, X.; Liu, Y.; Hao, G.; Huang, Z.; Zou, X.; Yang, L.; Li, J.; Zhong, J. Large-scale production of ultrathin topological insulator bismuth telluride nanosheets by a hydrothermal intercalation and exfoliation route. *J. Mater. Chem.* **2012**, 22, 4921-4926.

16. O'Neill, A.; Khan, U.; Coleman, J. N. Preparation of High Concentration Dispersions of Exfoliated MoS_2 with Increased Flake Size. *Chem. Mater.* **2012**, 24, 2414-2421.

17. Lee, C.; Yan, H.; Brus, L. E.; Heinz, T. F.; Hone, J.; Ryu, S. Anomalous Lattice Vibrations of Single- and Few-Layer MoS_2. *ACS Nano* **2010**, 4, 2695-2700.

18. Wang, G.; Huang, B.; Li, Z.; Lou, Z.; Wang, Z.; Dai, Y.; Whangbo, M.-H. Synthesis and characterization of ZnS with controlled amount of S vacancies for photocatalytic H_2 production under visible light. *Sci. Rep.* **2015**, 5, 8544.

19. Kim, I. S.; Sangwan, V. K.; Jariwala, D.; Wood, J. D.; Park, S.; Chen, K. S.; Shi, F. Y.; Ruiz-Zepeda, F.; Ponce, A.; Jose-Yacaman, M.; Dravid, V. P.; Marks, T. J.; Hersam, M. C.; Lauhon, L. J. Influence of Stoichiometry on the Optical and Electrical Properties of Chemical Vapor Deposition Derived MoS_2. *ACS Nano* **2014**, 8, 10551-10558.

20. Nam, D. E.; Song, W. S.; Yang, H. Noninjection, one-pot synthesis of Cu-deficient $CuInS_2$/ZnS core/shell quantum dots and their fluorescent properties. *J. Colloid Interface Sci.* **2011**, 361, 491-496.

Chapter 2

Literature review

2.1 Introduction

In this thesis the focus is on metal sulphide nanomaterials, in particular zero and two-dimensional structures. Metal sulphides have significantly grown in popularity in recent years, with the development of zero-dimensional semiconductor quantum dots and two-dimensional structures.[1, 2] These materials can be produced through a range of reactions, using both bottom-up and top-down processes.[3-5] Now extensive research can be found in the literature regarding optimisation of synthesis processes for a significant number of metal sulphide nanomaterials, offering controlled dimensions and desirable properties.[6-8]

Recent progress in combining multiple materials has resulted in a range of interesting new composite structures such as core-shell nanoparticles, decorated nanosheets and layered heterostructures.[9-11] These emerging observations open windows into an enormous range of previously unexplored possibilities.

There is ongoing research interest in development of new nanostructured metal sulphides and opportunities for advancement of existing processes with further optimisation of synthesis techniques and incorporation into functional devices. As such, relevant literature is reviewed here to identify research gaps that will be address in this PhD thesis.

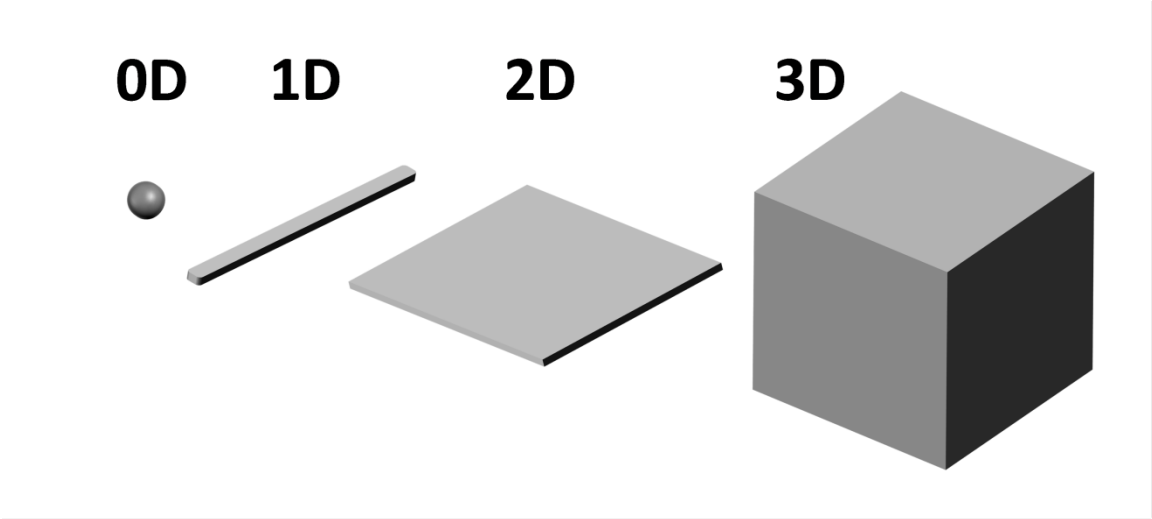

Figure 2.1 Representation of nanomaterials with different dimensions compared to 3D bulk material.

2.2 Two-dimensional materials

Two-dimensional (2D) materials are those which have one few-atom-thick dimension and are relatively large in the other two dimensions, as shown in Figure 2.1. These structures can be produced by isolation of free-standing layers from the naturally occurring crystals or by synthesising defined planar structures. 2D morphology results in extremely high surface-to-volume ratio and presents altered tunable electronic properties. The most well-known 2D material, graphene, is the one-atom-thick sheet made up of repeating units of hexagonally bonded carbon. Graphene was first isolated from graphite through a simple mechanical exfoliation process, using scotch-tape to isolate sheets down to monolayer thickness.[12] This discovery of graphene sparked interest into the exfoliation of other layered crystals such as boron nitride, transition metal dichalcogenides and phosphorene.[5, 13, 14]

2.2.1 Transition metal dichalcogenides

Transition metal dichalcogenides (TMDs) are a class of layered crystals which constitute a layer of metal atoms sandwiched between two layers of chalcogenide atoms (*i.e*. S, Se or Te). These 3-atom-thick layers are covalently bonded in two directions and are held together by weak van der Waals forces between layers in the bulk crystals, and can thus be isolated into atomically thin monolayers through a range of exfoliation techniques. TMDs have gained significant interest in recent years, due to their thickness dependent properties rendering them useful for new and diverse applications in electronic and optoelectronic devices.[2, 6, 15]

There are many compositions of TMDs, with the most extensively studied example being molybdenum disulphide (MoS_2). The crystal structure of native 2H-MoS_2 is hexagonal, with molybdenum atoms sandwiched between two layers of sulphur atoms in a trigonal prismatic bonding structure.[6] Covalent bonds link the unit cells in two directions across a planar structure and the weak forces holding the layers together are easily overcome through a range of exfoliation techniques.

2.2.2 Synthesis methods

Free-standing monolayer TMDs can be realised through either bottom-up (synthesis) or top-down (exfoliation) approaches. Extensive investigation of the exfoliation process has been conducted for many layered materials, through techniques such as mechanical transfer,[16] lithium ion intercalation[17] and solvent assisted processes.[13]

Mechanical transfer involves manually peeling apart bulk crystals, using scotch-tape, to isolate individual layers. The scotch-tape method can produce large scale ultrathin samples, however it is very time consuming and not easy to scale-up.[12, 18]

The method of intercalation involves the insertion of small ions into the inter-layer gaps followed by reaction with water, to force the layers apart. Intercalation-assisted methods are very efficient at producing a high yield of monolayer sheets, however the crystal quality is often compromised during the reactive process.[17, 19, 20]

Solvent assisted exfoliation makes use of sonication as the method for separation. Sonication-assisted methods tend to be less detrimental to the crystal quality, however the size and thickness of the product are hard to control and the yield of the exfoliation process is often quite low.[13, 14] For these reasons, there have been extensive studies into the optimisation of liquid-phase exfoliation processes. The yield of 2D sheets has been significantly improved through application of different solvents and surfactants which help to promote the exfoliation process.[21, 22]

To date, various methods for liquid-phase exfoliation of stratified TMD crystals have been investigated to obtain suspensions of atomically thin nanoflakes.[13, 14, 22-24] There are, however, still challenges that deal with increasing nanosheet yield and quality, in terms of optimised size, stoichiometry and crystallinity.[21, 25, 26]

An example of surfactant-assisted exfoliation was demonstrated by Smith *et al.*[22] using cholate molecules for the successful exfoliation of layered materials. Careful selection of the surfactant and solvent combination introduces the possibility of biocompatible exfoliation techniques.

2.2.3 Photoluminescence

Many 2D TMDs show photoluminescence (PL) when they are exfoliated from their stratified bulk into monolayers, due to electronic band structure changes.[2, 6] The most conspicuous of such PL emergences is seen in monolayer MoS_2. MoS_2 does not feature PL in its 2H bulk form due to an indirect bandgap. Exfoliation of the bulk MoS_2, to thin layers, alters the electronic band structure such that an indirect-to-direct bandgap transition occurs.[27] Single layer MoS_2 features intense optical absorption, PL and a direct bandgap which is significantly wider than the bandgap of multi-layer MoS_2.[28] Pristine monolayer MoS_2 displays only a modest PL yield of 0.4%,[27] and certainly increasing this yield would improve its suitability for imaging and sensing applications. One extensively reported method for PL enhancement is the surface passivation of quantum dots, using a higher bandgap material. As such, this thesis will explore the incorporation of MoS_2 into a hybrid nanostructure to explore the changes to its PL emission.

2.3 Quantum dots

Semiconductor quantum dots (QDs) have been explored for many years, with vast improvement to their controlled synthesis and development of many applications. QDs have been intensely investigated for their interesting size dependent optical and electronic properties. These properties emerge due to bandgap widening when the dimensions of QDs are reduced below the exciton Bohr radius of the respective material.[3] To date, QDs have been optimised for numerous applications including solar cells, light emitting diodes, sensors and bio-imaging,[1, 3] with several products becoming commercially available. Several previously reported examples of QDs are not safe for commercialisation because they are toxic and unstable in many environments.[1, 29] As such, alternative QD materials are still highly sought after. A suitable material would feature a favorable toxicological profile, stability in air or biological media, a high extinction coefficient and a sufficient PL yield.

2.3.1 MoS_2 quantum dots

Confinement of the lateral dimensions of MoS_2 has been shown to lead to further changes of the optical properties.[30, 31] In particles where the radius is comparable to the exciton Bohr radius, the band structure is tuned by quantum confinement. The dual effects of minimised thickness and reduced lateral size further alter the electronic band energy of the material, resulting in shorter wavelength emission. Wilcoxon *et al.*[31] found that the lateral dimensions of MoS_2 have a relatively stronger effect on its optical properties than the thickness does. The lateral dimensions of the particles control the spin-orbit splitting of the valance band causing a blue shift of absorbance and emission peaks.[31]

Recently, several methods have been developed to prepare MoS_2 QDs that produce blue shifted PL. These methods make use of either electrochemical etching,[32, 33] ultra-centrifugation[30] or pre-defined starting dimensions (nanoparticles)[34] to isolate small sized QDs. Very recently a solvothermal method was presented[35] using organic solvents, but was unsuccessful in aqueous solution.

One of the problems of MoS_2 QDs, synthesised using liquid based processes, is that the procedure may introduce defects and also generally form metallic edges.[19] These issues reduce the quality of

MoS_2 QDs in terms of possible PL yield. A typical strategy to reduce such effects is passivation using a wider bandgap material, which minimally interferes with the light absorption.

2.3.2 Surface passivation

Surface passivation protects the core and prevents non-radiative recombination occurring in surface trap sites, resulting in enhanced emission from the core.[10] This method has been extensively demonstrated for various QD compositions with different core-shell combinations.[3, 10] It is believed that a similar coating could help to enhance the optical emission from MoS_2 in 2D or QD states.

Amongst the passivation materials, zinc sulphide (ZnS) is a popular candidate as its shelling properties have been successfully demonstrated against other QDs.[3] Advantageously, ZnS is a stable, semiconducting sulphide that can exist in either of two crystal structures (i.e. sphalerite or wurtzite). The wurtzite crystal structure is hexagonal, with lattice parameters close to those of MoS_2 encouraging in-registry growth. Considering that ZnS is also a sulphur based compound, its synthesis procedures have good synergy with MoS_2 synthesis processes. Therefore ZnS can potentially be a suitable passivation candidate for use with MoS_2 QDs.

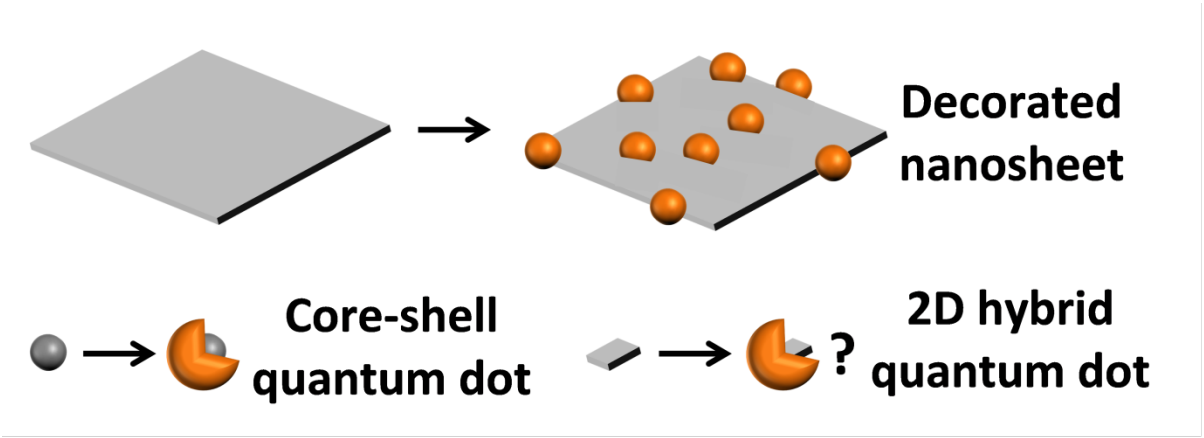

Figure 2.2 Demonstrated hybrid structures of nanoparticles grown on 2D sheets as well as core-shell QDs suggest that it may be possible to create hybrid QDs based on a 2D core.

2.3.3 Composite structures of exfoliated materials

There has been a recent interest in the synthesis of composites using layered materials,[9, 11] including nanoparticle growth on the surface of MoS_2.[36-39] These hybrid structures often show enhanced

properties compared to their individual components, making them useful in a range of applications such as photodetectors and catalysts.

At the time of this PhD research, no previous examples of hybrid QDs based on MoS_2 had been demonstrated. As such, this presents a gap in the research surrounding composite nanostructures, which will be investigated as a focus of this thesis.

2.4 Particle deposition techniques

Another important consideration when preparing nanoparticle suspensions is the translation of the particles into useable forms such as functional thin films. Suspensions can be used as printable inks for depositing films made of highly porous two-dimensional (2D) nanoflakes, with important applications for creating high efficiency energy conversion, sensing, semiconducting and optical devices.[40-42] The translation of resulting nanoflakes suspensions into useable films is currently a matter of intense investigation, to develop reliable and scalable printing and patterning methods.[43]

2.4.1 Thin films

Traditional thin film deposition techniques from suspended particles include drop-casting and spin-coating. These techniques usually result in non-uniform coatings of particles.[44] Uneven coverage prevents the films from interacting with their environment in a predictable and measurable way. Additionally, pin holes and inhomogeneities are detrimental for the fabrication of many devices.[45] Developing uniform and controlled deposition techniques is still of high importance for metal sulphide nanoparticles, especially for suspensions of exfoliated 2D materials.

2.4.2 Liquid-liquid interfaces

Liquid-liquid interfaces have been long studied for synthesis of particles and, more recently, for directed film assembly.[46-49] In the case of two-dimensional particles, there is a limitation in the orientation of the particles to lie flat at the interface.[49] This provides an opportunity to establish continuous films from 2D nanoflake suspensions, where flakes ideally assemble into a densely-packed thin film through edge-to-edge or overlapping edge-to-basal face contacts. Graphene has been

extensively reported to form films at liquid-liquid interfaces through either emulsification or separation.[50-54] There are also recent reports of TMD nanoflake based film formation by space-confined self-assembly, with the exfoliated nanoflakes being injected into a pre-formed liquid-liquid interface.[43, 55] However, the spontaneous liquid-liquid assembly of TMD based films, along with a patterned deposition, has not been studied. This thesis investigates a liquid-liquid assembly method which does not require any additional chemicals or initiators (inducing agents) which saves processing time and preserves the native chemistry of the nanosheets.[56-58] In order to make use of the assembled films, extraction is a critical step which can be achieved through deposition onto a suitable substrate.

2.4.3 Controlled patterned deposition

Large scale deposition of nanomaterial films in a controlled and directed manner is critical for developing useable devices. This is, in particular, important for forming thin films from suspensions of 2D materials. The deposition of particles can be controlled by restricting the accessible locations through substrate patterning.

Hydrophobic patterning for controlled deposition of graphene has been demonstrated previously by Wang *et al*.[59] Yet, such possibilities have not been shown for assembled 2D TMDs. As such, the extraction of assembled TMD films will be explored, using the recently developed technique for patterned deposition of monolayer semiconductor materials.[60]

In order to produce functional films with uniform coverage, large-scale 2D sheets are required, thus reducing the number of grain boundaries. This thesis will further investigate methods of micron-scale ultrathin nanosheet exfoliation.

2.5 Quasi-stratified crystals

Ultrathin 2D materials are produced from layered crystals such as graphite, transition metal dichalcogenides, boron nitride as well as many others.[5] Extensive research has been conducted to optimise the exfoliation of individual isolated planes to produce monolayer sheets.[2, 14] To continue

building the body of knowledge surrounding 2D nanosheets it would be beneficial to expand the target bulk materials to include crystals which are not fully-stratified and may possess interesting alternative properties. In a bid to introduce new 2D materials, exfoliation processes for alternative van der Waals crystals should also be investigated.

Crystals that are weakly bonded in two directions usually favour the formation of one-dimensional structures.[61] However, these van der Waals bonds may constitute different energies. As such, exfoliation of these crystals may contribute to the introduction of a new class of 2D materials. Monolayers formed from these crystals are expected to possess anisotropic properties due to their directional structures.[62] As such, exploration of these alternative 2D materials could present a useful new category of planar structures for incorporation into devices that benefit from anisotropic properties.

2.5.1 Bismuth sulphide

Bismuth sulphide (Bi_2S_3) exists as an orthorhombic crystal with isolated ribbons held together by van der Waals forces in two directions. Among the group V-VI semiconductors, Bi_2S_3 has recently attracted attention as an emerging functional material in nano morphologies. This metal chalcogenide compound has been shown to demonstrate a range of useful properties for applications in photodetectors,[63-67] photocatalysts,[68-70] thin film electrodes,[71] gas sensors,[72, 73] thermoelectrics,[62, 74, 75] lithium ion batteries[76] and solar cells.[77, 78]

To date, the reports on Bi_2S_3 have mostly been focused on the fully stoichiometric n-type phase of this material. Native bulk Bi_2S_3 has a direct band gap of 1.3 eV.[65] This value can be tuned by altering the dimensions of the material, increasing to values as high as 2.0 eV for Bi_2S_3 nanoparticles.[79] In a nano ribbon morphology, this material has shown a photoresponsitivity exceeding 4 A/W, resulting in a quantum efficiency of above 850%.[63] Bi_2S_3 based H_2 gas sensors have been demonstrated with a response time in the order of several hours at room temperature.[72] For electronics, the electron mobility has been reported to be in the range of 0.3 to 0.6 cm^2/Vs, with on/off ratios of 10^2-10^3.[65]

However, to date there is no report on any other stoichiometric or sub-stoichiometric bismuth sulphide showing p-type behavior.

2.5.2 One and two-dimensional structures

The most common crystal structure of stoichiometric Bi_2S_3 is orthorhombic, with a layered structure made of atomic scale ribbons projected in the direction of the b-axis, which are held together by van der Waals forces.[80] This favours formation of one-dimensional nanostructures, with many previous reports of synthesised nanowires,[65, 67, 81] nanorods[74, 82] and nanotubes.[80]

Only one previous report of a two-dimensional Bi_2S_3 structure has been presented by Chen *et al.*[63] In their work, Bi_2S_3 nanoribbons were synthesised using chemical approaches to form quasi two-dimensional structures. The existence of Bi_2S_3 in nanoribbon morphology is an indication that exfoliation of highly ordered bulk crystals into large, planar nanosheets may be possible. If a relatively gentle approach is taken, exfoliation of the crystals should be achievable without resulting in complete breakdown into individual ribbons.

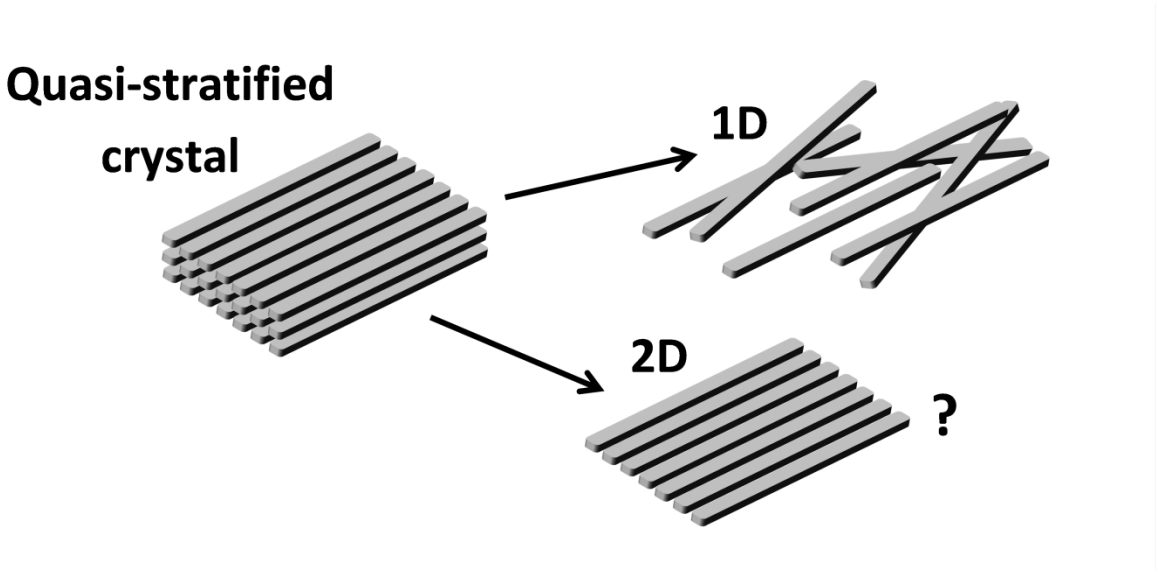

Figure 2.3 Quasi-stratified crystals such as Bi_2S_3 usually form 1D nanomaterials but it may also be possible to exfoliate the crystals into a 2D morphology.

It has been widely established that two-dimensional forms of materials such as graphene, phosphorene and transition metal dichalcogenides show vastly altered optical and electronic properties from their

bulk counterparts.[2, 83-86] We predict that such phenomena can also be observed in two-dimensional bismuth sulphides, if their efficient exfoliation is achieved. To the best of our knowledge, there is no report of top-down exfoliation processes or formation of micron-sized ultrathin Bi_2S_3 sheets. Isolation of ultrathin sheets from orthorhombic Bi_2S_3 could present a range of interesting, previously unexplored dimension-dependent properties.

2.5.3 Exfoliation techniques

The bulk crystal of orthorhombic Bi_2S_3 displays favored cleavage along the (010) plane, since the planar layers are held together by weak van der Waals forces.[87] Zhang *et al.* also report that the (040) plane has the lowest surface energy out of the major crystal facets.[77] As a result, we predict that it is likely that successful exfoliation of Bi_2S_3 would occur parallel to this plane. However, harsh exfoliation conditions could possibly result in the breakdown of the planar arrangement of the ribbon-like units, leading to the exfoliation of one-dimensional structures. Hence the exfoliation strategy has to be carefully designed in order to maintain the desired planar morphology.

A variety of liquid phase exfoliation approaches have been investigated for layered materials including graphene and transition metal dichalcogenides.[13, 21, 23, 88, 89] Many of such liquid exfoliation techniques are based on processes such as the intercalation of the layered entity using a highly reactive lithium reagent,[17, 20, 90] probe sonication in a surfactant solution[13, 88, 91] or a low energy solvent,[89] and delaminating the layered material by reaction with a reducing agent like hydrazine.[92, 93]

Out of such techniques, the hydrazine reduction process has distinct advantages. It is a very effective technique, requiring a short processing time and, more importantly, no mechanical agitation. Consequently, successful exfoliation can occur without resulting in the breakdown of the exfoliated sheets. As a result, ultrathin sheets of exfoliated material with very large lateral dimensions can be obtained. The hydrazine reduction process has recently been demonstrated for the exfoliation of MoS_2 by our group.[93] The author hypothesises that it can also be used for the exfoliation of large sheets from highly ordered bismuthinite, the naturally abundant crystals of Bi_2S_3.

2.6 Summary

Reviewing recent literature has highlighted the progress in the booming field of nanomaterial synthesis and applications. There has been immense research effort into morphological control during synthesis, with many examples of emerging nanostructured metal sulphides. However, several gaps in the knowledge regarding metal sulphide nanomaterial synthesis still exist. In brief, the gaps that the author of this thesis believes need attention include: (1) development of a biocompatible liquid exfoliation technique using an aqueous surfactant solution, (2) incorporation of MoS_2 into a hybrid QD through surface coating with another metal sulphide, (3) controlled thin film deposition of suspended 2D nanoflakes into a uniform film and (4) exfoliation of quasi-stratified crystals into ultrathin 2D nanosheets. In this thesis, the author will address the identified gaps through development of new metal sulphide synthesis routes.

In the following chapter, the PhD candidate will investigate biocompatible exfoliation of MoS_2. She will then describe a novel method to convert the MoS_2 into quantum dots with simultaneous ZnS synthesis to create hybrid quantum dots with improved photoluminescence emission.

Chapter 4 will focus on the controlled deposition of thin films from exfoliated TMDs. The suspended nanoflakes will be assembled via a liquid-liquid interface, without the addition of any chemical modifiers. The films will be collected onto hydrophobically-treated substrates for controlled patterned deposition.

The exfoliation of quasi-stratified Bi_2S_3 crystals will be presented in chapter 5. The author of this thesis will use a mechanically gentle exfoliation technique to produce micron-scale ultrathin nanosheets, then study the electronic and gas sensing properties of the new 2D material.

Chapter 6 presents the final conclusions and provides some suggestions for future research.

2.7 References

1. Bera, D.; Qian, L.; Tseng, T. K.; Holloway, P. H. Quantum Dots and Their Multimodal Applications: A Review. *Materials* **2010,** 3, 2260-2345.

2. Wang, Q. H.; Kalantar-Zadeh, K.; Kis, A.; Coleman, J. N.; Strano, M. S. Electronics and optoelectronics of two-dimensional transition metal dichalcogenides. *Nat. Nanotechnol.* **2012,** 7, 699-712.

3. Kim, J. Y.; Voznyy, O.; Zhitomirsky, D.; Sargent, E. H. 25th Anniversary Article: Colloidal Quantum Dot Materials and Devices: A Quarter-Century of Advances. *Adv. Mater.* **2013,** 25, 4986-5010.

4. Gao, M.-R.; Xu, Y.-F.; Jiang, J.; Yu, S.-H. Nanostructured metal chalcogenides: synthesis, modification, and applications in energy conversion and storage devices. *Chem. Soc. Rev.* **2013,** 42, 2986-3017.

5. Butler, S. Z.; Hollen, S. M.; Cao, L. Y.; Cui, Y.; Gupta, J. A.; Gutierrez, H. R.; Heinz, T. F.; Hong, S. S.; Huang, J. X.; Ismach, A. F.; Johnston-Halperin, E.; Kuno, M.; Plashnitsa, V. V.; Robinson, R. D.; Ruoff, R. S.; Salahuddin, S.; Shan, J.; Shi, L.; Spencer, M. G.; Terrones, M.; Windl, W.; Goldberger, J. E. Progress, Challenges, and Opportunities in Two-Dimensional Materials Beyond Graphene. *ACS Nano* **2013,** 7, 2898-2926.

6. Chhowalla, M.; Shin, H. S.; Eda, G.; Li, L. J.; Loh, K. P.; Zhang, H. The chemistry of two-dimensional layered transition metal dichalcogenide nanosheets. *Nat. Chem.* **2013,** 5, 263-275.

7. Dunne, P. W.; Starkey, C. L.; Gimeno-Fabra, M.; Lester, E. H. The rapid size- and shape-controlled continuous hydrothermal synthesis of metal sulphide nanomaterials. *Nanoscale* **2014,** 6, 2406-2418.

8. Lai, C.-H.; Lu, M.-Y.; Chen, L.-J. Metal sulfide nanostructures: synthesis, properties and applications in energy conversion and storage. *J. Mater. Chem.* **2012,** 22, 19-30.

9. Huang, X.; Tan, C. L.; Yin, Z. Y.; Zhang, H. 25th Anniversary Article: Hybrid Nanostructures Based on Two-Dimensional Nanomaterials. *Adv. Mater.* **2014,** 26, 2185-2204.

10. Reiss, P.; Protiere, M.; Li, L. Core/Shell Semiconductor Nanocrystals. *Small* **2009,** 5, 154-168.

11. Gunjakar, J. L.; Kim, I. Y.; Lee, J. M.; Jo, Y. K.; Hwang, S.-J. Exploration of Nanostructured Functional Materials Based on Hybridization of Inorganic 2D Nanosheets. *J. Phys. Chem. C* **2014,** 118, 3847-3863.

12. Novoselov, K. S.; Geim, A. K.; Morozov, S. V.; Jiang, D.; Zhang, Y.; Dubonos, S. V.; Grigorieva, I. V.; Firsov, A. A. Electric Field Effect in Atomically Thin Carbon Films. *Science* **2004,** 306, 666-669.

13. Coleman, J. N.; Lotya, M.; O'Neill, A.; Bergin, S. D.; King, P. J.; Khan, U.; Young, K.; Gaucher, A.; De, S.; Smith, R. J.; Shvets, I. V.; Arora, S. K.; Stanton, G.; Kim, H.-Y.; Lee, K.; Kim, G. T.; Duesberg, G. S.; Hallam, T.; Boland, J. J.; Wang, J. J.; Donegan, J. F.; Grunlan, J. C.; Moriarty, G.; Shmeliov, A.; Nicholls, R. J.; Perkins, J. M.; Grieveson, E. M.; Theuwissen, K.; McComb, D. W.; Nellist, P. D.; Nicolosi, V. Two-Dimensional Nanosheets Produced by Liquid Exfoliation of Layered Materials. *Science* **2011,** 331, 568-571.

14. Nicolosi, V.; Chhowalla, M.; Kanatzidis, M. G.; Strano, M. S.; Coleman, J. N. Liquid Exfoliation of Layered Materials. *Science* **2013,** 340, 1226419.

15. Zhuiykov, S.; Kats, E. Atomically thin two-dimensional materials for functional electrodes of electrochemical devices. *Ionics* **2013,** 19, 825-865.

16. Late, D. J.; Liu, B.; Matte, H.; Rao, C. N. R.; Dravid, V. P. Rapid Characterization of Ultrathin Layers of Chalcogenides on SiO_2/Si Substrates. *Adv. Funct. Mater.* **2012,** 22, 1894-1905.

17. Eda, G.; Yamaguchi, H.; Voiry, D.; Fujita, T.; Chen, M.; Chhowalla, M. Photoluminescence from Chemically Exfoliated MoS_2. *Nano Lett.* **2011,** 11, 5111-5116.

18. Lee, C.; Yan, H.; Brus, L. E.; Heinz, T. F.; Hone, J.; Ryu, S. Anomalous Lattice Vibrations of Single- and Few-Layer MoS_2. *ACS Nano* **2010,** 4, 2695-2700.

19. Ambrosi, A.; Sofer, Z.; Pumera, M. 2H → 1T phase transition and hydrogen evolution activity of MoS_2, $MoSe_2$, WS_2 and WSe_2 strongly depends on the MX_2 composition. *Chem. Commun.* **2015,** 51, 8450-8453.

20. Ambrosi, A.; Sofer, Z.; Pumera, M. Lithium Intercalation Compound Dramatically Influences the Electrochemical Properties of Exfoliated MoS_2. *Small* **2015,** 11, 605-612.

21. O'Neill, A.; Khan, U.; Coleman, J. N. Preparation of High Concentration Dispersions of Exfoliated MoS2 with Increased Flake Size. *Chem. Mater.* **2012,** 24, 2414-2421.

22. Smith, R. J.; King, P. J.; Lotya, M.; Wirtz, C.; Khan, U.; De, S.; O'Neill, A.; Duesberg, G. S.; Grunlan, J. C.; Moriarty, G.; Chen, J.; Wang, J.; Minett, A. I.; Nicolosi, V.; Coleman, J. N. Large-Scale Exfoliation of Inorganic Layered Compounds in Aqueous Surfactant Solutions. *Adv. Mater.* **2011,** 23, 3944-3948.

23. Carey, B. J.; Daeneke, T.; Nguyen, E. P.; Wang, Y.; Zhen Ou, J.; Zhuiykov, S.; Kalantar-zadeh, K. Two solvent grinding sonication method for the synthesis of two-dimensional tungsten disulphide flakes. *Chem. Commun.* **2015,** 51, 3770-3773.

24. Giovanelli, E.; Castellanos-Gomez, A.; Pérez, E. M. Surfactant-Free Polar-to-Nonpolar Phase Transfer of Exfoliated MoS_2 Two-Dimensional Colloids. *ChemPlusChem* **2017,** 82, 1-11.

25. Eng, A. Y. S.; Ambrosi, A.; Sofer, Z.; Šimek, P.; Pumera, M. Electrochemistry of Transition Metal Dichalcogenides: Strong Dependence on the Metal-to-Chalcogen Composition and Exfoliation Method. *ACS Nano* **2014,** 8, 12185-12198.

26. Daeneke, T.; Clark, R. M.; Carey, B. J.; Ou, J. Z.; Weber, B.; Fuhrer, M. S.; Bhaskaran, M.; Kalantar-zadeh, K. Reductive exfoliation of substoichiometric MoS2 bilayers using hydrazine salts. *Nanoscale* **2016,** 8, 15252-15261.

27. Mak, K. F.; Lee, C.; Hone, J.; Shan, J.; Heinz, T. F. Atomically Thin MoS_2: A New Direct-Gap Semiconductor. *Phys. Rev. Lett.* **2010,** 105, 136805.

28. Kuc, A.; Zibouche, N.; Heine, T. Influence of quantum confinement on the electronic structure of the transition metal sulfide TS_2. *Phys. Rev. B* **2011,** 83, 245213.

29. Frasco, M. F.; Chaniotakis, N. Semiconductor quantum dots in chemical sensors and biosensors. *Sensors* **2009,** 9, 7266-7286.

30. Gan, Z. X.; Liu, L. Z.; Wu, H. Y.; Hao, Y. L.; Shan, Y.; Wu, X. L.; Chu, P. K. Quantum confinement effects across two-dimensional planes in MoS_2 quantum dots. *Appl. Phys. Lett.* **2015,** 106, 233113.

31. Wilcoxon, J. P.; Newcomer, P. P.; Samara, G. A. Synthesis and optical properties of MoS_2 and isomorphous nanoclusters in the quantum confinement regime. *J. Appl. Phys.* **1997,** 81, 7934-7944.

32. Li, B. L.; Chen, L. X.; Zou, H. L.; Lei, J. L.; Luo, H. Q.; Li, N. B. Electrochemically induced Fenton reaction of few-layer MoS_2 nanosheets: preparation of luminescent quantum dots via a transition of nanoporous morphology. *Nanoscale* **2014,** 6, 9831-9838.

33. Gopalakrishnan, D.; Damien, D.; Li, B.; Gullappalli, H.; Pillai, V. K.; Ajayan, P. M.; Shaijumon, M. M. Electrochemical synthesis of luminescent MoS_2 quantum dots. *Chem. Commun.* **2015,** 51, 6293-6296.

34. Ha, H. D.; Han, D. J.; Choi, J. S.; Park, M.; Seo, T. S. Dual Role of Blue Luminescent MoS_2 Quantum Dots in Fluorescence Resonance Energy Transfer Phenomenon. *Small* **2014,** 10, 3858-3862.

35. Xu, S. J.; Li, D.; Wu, P. Y. One-Pot, Facile, and Versatile Synthesis of Monolayer MoS_2/WS_2 Quantum Dots as Bioimaging Probes and Efficient Electrocatalysts for Hydrogen Evolution Reaction. *Adv. Funct. Mater.* **2015,** 25, 1127-1136.

36. Cheng, Z. H.; He, B. Z.; Zhou, L. A general one-step approach for in situ decoration of MoS_2 nanosheets with inorganic nanoparticles. *J. Mater. Chem. A* **2015,** 3, 1042-1048.

37. Huang, X.; Zeng, Z. Y.; Bao, S. Y.; Wang, M. F.; Qi, X. Y.; Fan, Z. X.; Zhang, H. Solution-phase epitaxial growth of noble metal nanostructures on dispersible single-layer molybdenum disulfide nanosheets. *Nat. Commun.* **2013,** 4, 1444.

38. Schornbaum, J.; Winter, B.; Schießl, S. P.; Gannott, F.; Katsukis, G.; Guldi, D. M.; Spiecker, E.; Zaumseil, J. Epitaxial Growth of PbSe Quantum Dots on MoS_2 Nanosheets and their Near-Infrared Photoresponse. *Adv. Funct. Mater.* **2014,** 24, 5798-5806.

39. Sreeprasad, T. S.; Nguyen, P.; Kim, N.; Berry, V. Controlled, Defect-Guided, Metal-Nanoparticle Incorporation onto MoS_2 via Chemical and Microwave Routes: Electrical, Thermal, and Structural Properties. *Nano Lett.* **2013,** 13, 4434-4441.

40. Finn, D. J.; Lotya, M.; Cunningham, G.; Smith, R. J.; McCloskey, D.; Donegan, J. F.; Coleman, J. N. Inkjet deposition of liquid-exfoliated graphene and MoS2 nanosheets for printed device applications. *J. Mater. Chem. C* **2014,** 2, 925-932.

41. Alsaif, M. M. Y. A.; Chrimes, A. F.; Daeneke, T.; Balendhran, S.; Bellisario, D. O.; Son, Y.; Field, M. R.; Zhang, W.; Nili, H.; Nguyen, E. P.; Latham, K.; van Embden, J.; Strano, M. S.; Ou, J. Z.; Kalantar-zadeh, K. High-Performance Field Effect Transistors Using Electronic Inks of 2D Molybdenum Oxide Nanoflakes. *Adv. Funct. Mater.* **2016,** 26, 91-100.

42. Cao, X.; Tan, C.; Zhang, X.; Zhao, W.; Zhang, H. Solution-Processed Two-Dimensional Metal Dichalcogenide-Based Nanomaterials for Energy Storage and Conversion. *Adv. Mater.* **2016,** 28, 6167-6196.

43. Yu, X.; Prevot, M. S.; Guijarro, N.; Sivula, K. Self-assembled 2D WSe_2 thin films for photoelectrochemical hydrogen production. *Nat. Commun.* **2015,** 6, 8596.

44. Chan, Y. Y.; Eng, A. Y. S.; Pumera, M.; Webster, R. D. Assessments of Surface Coverage after Nanomaterials are Drop Cast onto Electrodes for Electroanalytical Applications. *ChemElectroChem* **2015,** 2, 1003-1009.

45. Yu, X.; Prévot, M. S.; Sivula, K. Multiflake Thin Film Electronic Devices of Solution Processed 2D MoS_2 Enabled by Sonopolymer Assisted Exfoliation and Surface Modification. *Chem. Mater.* **2014,** 26, 5892-5899.

46. Niu, Z.; He, J.; Russell, T. P.; Wang, Q. Synthesis of Nano/Microstructures at Fluid Interfaces. *Angew. Chem., Int. Ed.* **2010,** 49, 10052-10066.

47. Hu, L.; Chen, M.; Fang, X.; Wu, L. Oil-water interfacial self-assembly: a novel strategy for nanofilm and nanodevice fabrication. *Chem. Soc. Rev.* **2012,** 41, 1350-1362.

48. Bresme, F.; Oettel, M. Nanoparticles at fluid interfaces. *J. Phys.: Condens. Matter* **2007,** 19, 413101.

49. Booth, S. G.; Dryfe, R. A. W. Assembly of Nanoscale Objects at the Liquid/Liquid Interface. *J. Phys. Chem. C* **2015,** 119, 23295-23309.

50. Biswas, S.; Drzal, L. T. A Novel Approach to Create a Highly Ordered Monolayer Film of Graphene Nanosheets at the Liquid−Liquid Interface. *Nano Lett.* **2009,** 9, 167-172.

51. Gudarzi, M. M.; Sharif, F. Self assembly of graphene oxide at the liquid-liquid interface: A new route to the fabrication of graphene based composites. *Soft Matter* **2011,** 7, 3432-3440.

52. Kim, J.; Cote, L. J.; Kim, F.; Yuan, W.; Shull, K. R.; Huang, J. Graphene Oxide Sheets at Interfaces. *J. Am. Chem. Soc.* **2010,** 132, 8180-8186.

53. Cote, L. J.; Kim, F.; Huang, J. Langmuir−Blodgett Assembly of Graphite Oxide Single Layers. *J. Am. Chem. Soc.* **2009,** 131, 1043-1049.

54. Woltornist, S. J.; Oyer, A. J.; Carrillo, J. M. Y.; Dobrynin, A. V.; Adamson, D. H. Conductive Thin Films of Pristine Graphene by Solvent Interface Trapping. *Acs Nano* **2013,** 7, 7062-7066.

55. Tsokkou, D.; Yu, X.; Sivula, K.; Banerji, N. The Role of Excitons and Free Charges in the Excited-State Dynamics of Solution-Processed Few-Layer MoS2 Nanoflakes. *J. Phys. Chem. C* **2016,** 120, 23286-23292.

56. Zhang, X.; Lai, Z.; Tan, C.; Zhang, H. Solution-Processed Two-Dimensional MoS_2 Nanosheets: Preparation, Hybridization, and Applications. *Angew. Chem., Int. Ed.* **2016,** 55, 8816-8838.

57. Mohamad Latiff, N.; Wang, L.; Mayorga-Martinez, C. C.; Sofer, Z.; Fisher, A. C.; Pumera, M. Valence and oxide impurities in MoS_2 and WS_2 dramatically change their electrocatalytic activity towards proton reduction. *Nanoscale* **2016,** 8, 16752-16760.

58. Molina-Mendoza, A. J.; Vaquero-Garzon, L.; Leret, S.; de Juan-Fernandez, L.; Perez, E. M.; Castellanos-Gomez, A. Engineering the optoelectronic properties of MoS_2 photodetectors through reversible noncovalent functionalization. *Chem. Commun.* **2016,** 52, 14365-14368.

59. Wang, Z.; Yang, X. S.; Chen, M. Y. Assembly of Patterned Graphene Film Aided by Wetting/Nonwetting Surface on Liquid Interface. *IEEE Trans. Nanotechnol.* **2014,** 13, 589-593.

60. Carey, B. J.; Ou, J. Z.; Clark, R. M.; Berean, K. J.; Zavabeti, A.; Chesman, A. S. R.; Russo, S. P.; Lau, D. W. M.; Xu, Z.-Q.; Bao, Q.; Kevehei, O.; Gibson, B. C.; Dickey, M. D.; Kaner, R. B.; Daeneke, T.; Kalantar-Zadeh, K. Wafer-scale two-dimensional semiconductors from printed oxide skin of liquid metals. *Nat. Commun.* **2017,** 8, 14482.

61. Malakooti, R.; Cademartiri, L.; Akçakir, Y.; Petrov, S.; Migliori, A.; Ozin, G. A. Shape-Controlled Bi_2S_3 Nanocrystals and Their Plasma Polymerization into Flexible Films. *Adv. Mater.* **2006,** 18, 2189-2194.

62. Biswas, K.; Zhao, L.-D.; Kanatzidis, M. G. Tellurium-Free Thermoelectric: The Anisotropic n-Type Semiconductor Bi_2S_3. *Adv. Energy Mater.* **2012,** 2, 634-638.

63. Chen, G.; Yu, Y.; Zheng, K.; Ding, T.; Wang, W.; Jiang, Y.; Yang, Q. Fabrication of Ultrathin Bi_2S_3 Nanosheets for High-Performance, Flexible, Visible–NIR Photodetectors. *Small* **2015,** 11, 2848-2855.

64. Li, R.; Yang, J.; Huo, N.; Fan, C.; Lu, F.; Yan, T.; Wei, Z.; Li, J. Effect of Electrical Contact on the Performance of Bi2S3 Single Nanowire Photodetectors. *ChemPhysChem* **2014,** 15, 2510-2516.

65. Lu, F.; Li, R.; Li, Y.; Huo, N.; Yang, J.; Li, Y.; Li, B.; Yang, S.; Wei, Z.; Li, J. Improving the Field-Effect Performance of Bi_2S_3 Single Nanowires by an Asymmetric Device Fabrication. *ChemPhysChem* **2015,** 16, 99-103.

66. Li, R.; Yue, Q.; Wei, Z. Abnormal low-temperature behavior of a continuous photocurrent in Bi2S3 nanowires. *J. Mater. Chem. C* **2013,** 1, 5866-5871.

67. Bao, H.; Cui, X.; Li, C. M.; Gan, Y.; Zhang, J.; Guo, J. Photoswitchable Semiconductor Bismuth Sulfide (Bi2S3) Nanowires and Their Self-Supported Nanowire Arrays. *J. Phys. Chem. C* **2007,** 111, 12279-12283.

68. Gao, X.; Huang, G.; Gao, H.; Pan, C.; Wang, H.; Yan, J.; Liu, Y.; Qiu, H.; Ma, N.; Gao, J. Facile fabrication of Bi_2S_3/SnS_2 heterojunction photocatalysts with efficient photocatalytic activity under visible light. *J. Alloys Compd.* **2016,** 674, 98-108.

69. Zhang, Z.; Wang, W.; Wang, L.; Sun, S. Enhancement of Visible-Light Photocatalysis by Coupling with Narrow-Band-Gap Semiconductor: A Case Study on Bi_2S_3/Bi_2WO_6. *ACS Appl. Mater. Interfaces* **2012,** 4, 593-597.

70. Wu, T.; Zhou, X.; Zhang, H.; Zhong, X. Bi_2S_3 nanostructures: A new photocatalyst. *Nano Res.* **2010,** 3, 379-386.

71. Tamašauskaitė-Tamašiūnaitė, L.; Valiulienė, G.; Žielienė, A.; Šimkūnaitė-Stanynienė, B.; Naruškevičius, L.; Sudavičius, A. EQCM study on the oxidation/reduction of bismuth sulfide thin films. *J. Electroanal. Chem.* **2010,** 642, 22-29.

72. Yao, K.; Gong, W. W.; Hu, Y. F.; Liang, X. L.; Chen, Q.; Peng, L. M. Individual Bi_2S_3 Nanowire-Based Room-Temperature H_2 Sensor. *J. Phys. Chem. C* **2008,** 112, 8721-8724.

73. Li, H.; Yang, J.; Zhang, J.; Zhou, M. Facile synthesis of hierarchical Bi_2S_3 nanostructures for photodetector and gas sensor. *RSC Adv.* **2012,** 2, 6258-6261.

74. Liufu, S.-C.; Chen, L.-D.; Yao, Q.; Wang, C.-F. Assembly of one-dimensional nanorods into Bi_2S_3 films with enhanced thermoelectric transport properties. *Appl. Phys. Lett.* **2007,** 90, 112106.

75. Chmielowski, R.; Péré, D.; Bera, C.; Opahle, I.; Xie, W.; Jacob, S.; Capet, F.; Roussel, P.; Weidenkaff, A.; Madsen, G. K. H.; Dennler, G. Theoretical and experimental investigations of the thermoelectric properties of Bi_2S_3. *J. Appl. Phys.* **2015,** 117, 125103.

76. Zhang, Z.; Zhou, C.; Huang, L.; Wang, X.; Qu, Y.; Lai, Y.; Li, J. Synthesis of bismuth sulfide/reduced graphene oxide composites and their electrochemical properties for lithium ion batteries. *Electrochim. Acta* **2013,** 114, 88-94.

77. Zhang, H.; Yang, L.; Liu, Z.; Ge, M.; Zhou, Z.; Chen, W.; Li, Q.; Liu, L. Facet-dependent activity of bismuth sulfide as low-cost counter-electrode materials for dye-sensitized solar cells. *J. Mater. Chem.* **2012,** 22, 18572-18577.

78. Becerra, D.; Nair, M. T. S.; Nair, P. K. Analysis of a Bismuth Sulfide/Silicon Junction for Building Thin Film Solar Cells. *J. Electrochem. Soc.* **2011,** 158, H741-H749.

79. Han, P.; Mihi, A.; Ferre-borrull, J.; Pallarés, J.; Marsal, L. F. Interplay Between Morphology, Optical Properties, and Electronic Structure of Solution-Processed Bi_2S_3 Colloidal Nanocrystals. *J. Phys. Chem. C* **2015,** 119, 10693-10699.

80. Wang, D.; Hao, C.; Zheng, W.; Ma, X.; Chu, D.; Peng, Q.; Li, Y. Bi_2S_3 nanotubes: Facile synthesis and growth mechanism. *Nano Res.* **2009,** 2, 130-134.

81. Yu, X.; Cao, C.; Zhu, H. Synthesis and photoluminescence properties of Bi_2S_3 nanowires via surfactant micelle-template inducing reaction. *Solid State Commun.* **2005,** 134, 239-243.

82. Liao, H.-C.; Wu, M.-C.; Jao, M.-H.; Chuang, C.-M.; Chen, Y.-F.; Su, W.-F. Synthesis, optical and photovoltaic properties of bismuth sulfide nanorods. *CrystEngComm* **2012,** 14, 3645-3652.

83. Zhu, Y.; Murali, S.; Cai, W.; Li, X.; Suk, J. W.; Potts, J. R.; Ruoff, R. S. Graphene and Graphene Oxide: Synthesis, Properties, and Applications. *Adv. Mater.* **2010,** 22, 3906-3924.

84. Zhang, X.; Liu, Y.; Zhang, G.; Wang, Y.; Zhang, H.; Huang, F. Thermal Decomposition of Bismuth Oxysulfide from Photoelectric Bi_2O_2S to Superconducting $Bi_4O_4S_3$. *ACS Appl. Mater. Interfaces* **2015,** 7, 4442-4448.

85. Lu, Q.; Yu, Y.; Ma, Q.; Chen, B.; Zhang, H. 2D Transition-Metal-Dichalcogenide-Nanosheet-Based Composites for Photocatalytic and Electrocatalytic Hydrogen Evolution Reactions. *Adv. Mater.* **2016,** 28, 1917-1933.

86. Mayorga-Martinez, C. C.; Sofer, Z.; Pumera, M. Layered Black Phosphorus as a Selective Vapor Sensor. *Angew. Chem. Int. Ed.* **2015,** 127, 14525-14528.

87. Grigas, J.; Talik, E.; Lazauskas, V. X-ray Photoelectron Spectra and Electronic Structure of Bi_2S_3 Crystals. *Phys. Status Solidi B* **2002,** 232, 220-230.

88. Lotya, M.; Hernandez, Y.; King, P. J.; Smith, R. J.; Nicolosi, V.; Karlsson, L. S.; Blighe, F. M.; De, S.; Wang, Z.; McGovern, I. T.; Duesberg, G. S.; Coleman, J. N. Liquid Phase Production of Graphene by Exfoliation of Graphite in Surfactant/Water Solutions. *J. Am. Chem. Soc.* **2009,** 131, 3611-3620.

89. Nguyen, E. P.; Carey, B. J.; Daeneke, T.; Ou, J. Z.; Latham, K.; Zhuiykov, S.; Kalantar-zadeh, K. Investigation of Two-Solvent Grinding-Assisted Liquid Phase Exfoliation of Layered MoS_2. *Chem. Mater.* **2015,** 27, 53-59.

90. Ren, L.; Qi, X.; Liu, Y.; Hao, G.; Huang, Z.; Zou, X.; Yang, L.; Li, J.; Zhong, J. Large-scale production of ultrathin topological insulator bismuth telluride nanosheets by a hydrothermal intercalation and exfoliation route. *J. Mater. Chem.* **2012,** 22, 4921-4926.

91. Clark, R. M.; Carey, B. J.; Daeneke, T.; Atkin, P.; Bhaskaran, M.; Latham, K.; Cole, I. S.; Kalantar-zadeh, K. Two-step synthesis of luminescent MoS_2-ZnS hybrid quantum dots. *Nanoscale* **2015,** 7, 16763-16772.

92. Zheng, J.; Zhang, H.; Dong, S.; Liu, Y.; Tai Nai, C.; Suk Shin, H.; Young Jeong, H.; Liu, B.; Ping Loh, K. High yield exfoliation of two-dimensional chalcogenides using sodium naphthalenide. *Nat. Commun.* **2014,** 5.

93. Daeneke, T.; Clark, R. M.; Carey, B.; Ou, J. Z.; Weber, B.; Fuhrer, M. S.; Bhaskaran, M.; Kalantar-zadeh, K. Reductive exfoliation of substoichiometric MoS2 bilayers using hydrazine salts. *Nanoscale* **2016**.

Chapter 3

Two-step synthesis of luminescent MoS_2-ZnS hybrid quantum dots

3.1 Introduction

MoS_2 has been recently identified as a potential quantum dot (QD) material candidate, due to its high stability, low toxicity, abundance and suitable optical properties.[1, 2] The inherently low photoluminescence (PL) from ultrathin MoS_2 limits its usefulness as a luminescent material for optical sensing. As such, the enhancement of the PL emission from MoS_2 is of immediate interest in order to develop new optical applications. The demonstration of quantum yield enhancement, through passivation, in core-shell QDs is an ideal model for potential PL enhancement of other core materials.

In this chapter, a novel and scalable synthetic method for thin MoS_2-ZnS hybrid QDs is established. A modified surfactant assisted exfoliation technique has been developed, using the naturally occurring bile acid chenodeoxycholic acid (CDCA). This leads to high exfoliation yields in ethanol water mixtures, while maintaining a green synthesis profile and biocompatibility. I propose a novel

hydrothermal method, in which aqueous suspensions of exfoliated laterally large MoS_2 sheets are broken down into QDs. This approach limits one dimension of the QDs through the pre-defined thickness of the precursor flakes. Advantageously, ZnS growth can be achieved simultaneously in the hydrothermal step. The synthesised hybrid MoS_2-ZnS QDs are found to feature superior PL yields with emissions independent from the excitation wavelength, which is a sign of a relatively narrow size distribution. The hybrid QDs with stable emission properties are likely to be useful as imaging agents and could be tuned as nanosensors with measurable optical emission.

The contents of this chapter have been published as an article in Nanoscale journal, 2015.[3]

3.2 Experimental details

3.2.1 Exfoliation

A modified surfactant assisted method was used for the exfoliation of MoS_2. 1 g of MoS_2 powder (<1 μm size, 99.9% US Nano) was ground in a mortar and pestle with 1.5 mL of acetonitrile for 15 minutes, before adding an additional 1.5 mL and grinding for a further 15 minutes. The ground powder was left to dry for approximately 10 minutes. Meanwhile, 7 mg of CDCA was dissolved in 40 mL of a 50:50 v/v mixture of ethanol and water, the pH was adjusted to 10 using 30% ammonia. The ground MoS_2 powder was then suspended in 30 mL of the CDCA solution and probe sonicated (QSonica, 500 W, amplitude 20%) for 90 minutes with a pulse ratio of 50:10 seconds. The resulting mixture was centrifuged at 4000 RPM for 90 minutes, to remove sediment powder and obtain the yellow-green MoS_2 suspension (Figure 3.1 step 1).

3.2.2 Hydrothermal processing

For the 0 mM sample, 2 mL of MoS_2 suspension and 8 mL of MilliQ water were mixed and the pH was adjusted to 10 using 30% ammonia. The mixture was stirred for 30 minutes before transferring to a 50 mL Teflon-lined stainless steel autoclave and kept at 140˚C for 3 hours. The autoclave was cooled to room temperature before transferring the products into a 15 mL tube and centrifuging at 4000 RPM for 60 minutes.

For the time length study, 0 mM solutions (as described above) were heated and removed from the oven at varying times over the course of 24 hours. For the surfactant control study, samples were prepared using 2 mL of surfactant solution in place of the suspension of MoS_2.

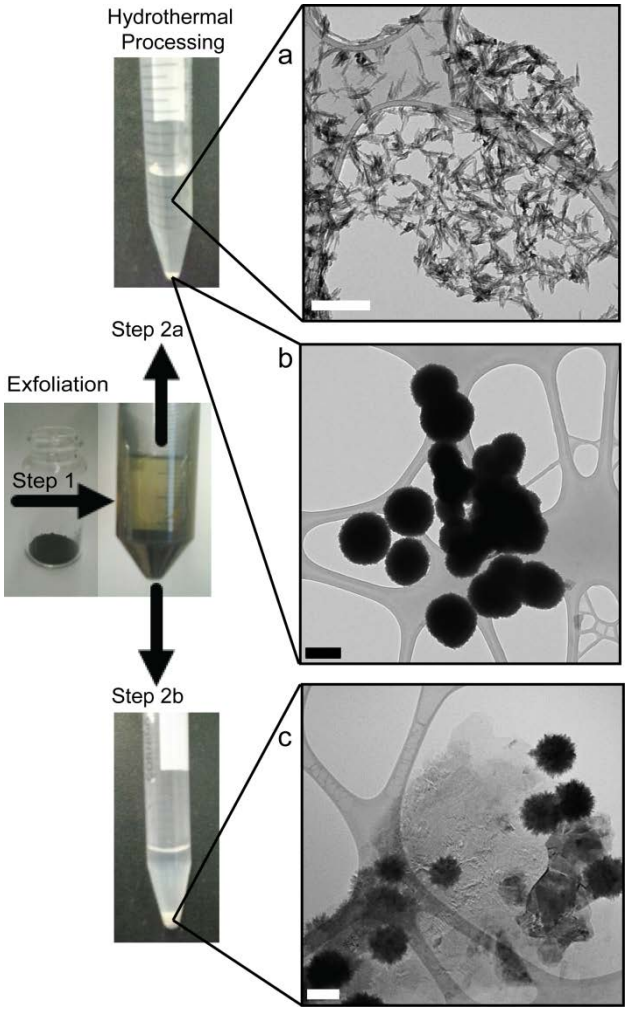

Figure 3.1 Flow chart of synthetic procedure, with photos at each step, and TEM images of products: (a) Hydrothermal reaction supernatant. (b) Hydrothermal reaction precipitates. (c) Hydrothermal reaction precipitates using sediment MoS_2, scale bars 200 nm.

3.2.3 Hydrothermal processing with simultaneous ZnS growth

A 10 mL sample was prepared using 2 mL of the exfoliated MoS_2 suspension, 1 mM zinc nitrate hexahydrate and 2 mM L-cysteine in MilliQ water, the pH was adjusted to 10 using 30% ammonia. The rest of the procedure was similar to the preparation of the 0 mM sample (Figure 3.1 step 2a). The colourless supernatant was decanted and the white precipitate was re-suspended in MilliQ water. This procedure was repeated over a concentration range of 0.01 to 10 mM zinc nitrate hexahydrate with

L-cysteine in a molar ratio of 1:2. The samples are referred to by their zinc content, for instance the sample with 0.4 mM zinc nitrate hexahydrate is called “0.4 mM sample”. PL emission zinc sensitivity testing was performed by preparing samples from suspended MoS_2 processed with neither zinc nor cysteine, with only 2 mM cysteine, and with only 1 mM zinc nitrate hexahydrate. PL spectra were collected, then 1 mM zinc nitrate hexahydrate was added to the samples that contained no zinc and PL was again collected. The hydrothermal processing was also repeated using sediment MoS_2 in place of suspended MoS_2 flakes (Figure 3.1 step 2b).

3.2.4 Characterisation

Optical characterisation of the products was performed on the suspensions, without further treatment, using 1 cm path length cuvettes. Ultra violet- visible spectroscopy (UV-vis) was collected with a Cary 500 spectrometer and PL was collected using a Cary Eclipse fluorescence spectrophotometer. Particle size and quality were assessed by transmission electron microscopy (TEM) using a JEOL1010 instrument (100 keV), and high resolution TEM (HRTEM) was performed using a JEOL2100F (80 keV). Samples were dropped onto holey carbon covered copper mesh TEM grids. Raman spectra (Reinshaw inVia) were collected, from samples drop-cast onto silicon substrates, using a 785 nm laser. The elemental composition was studied by x-ray photoelectron spectroscopy (XPS) of samples drop-cast on silicon substrates and also by energy dispersive x-ray spectroscopy (EDX) within the JEOL2100F TEM. XPS (Thermo Scientific K-alpha) was performed using an Al Kα source (λ= 8.3386Å), with an etch step depth calculated to be approximately 2 nm. EDX was collected with an X-max^N 80T detector (Oxford instruments) attached to the JEOL2100F instrument. Crystal structure information was collected on a Bruker D4 Endeavour x-ray diffractometer (XRD) using Cu Kα radiation (λ= 1.5406 Å). Samples were prepared by repeated application and subsequent drying of each suspension onto a glass substrate, until sufficient sample coverage was achieved. Flake thickness was determined by atomic force microscopy (AFM) of a diluted sample dried on a silicon substrate, using a Bruker Dimension Icon in ScanAsyst mode. Scanning electron microscopy (SEM) was performed using an FEI Nova NanoSEM operating at 5 keV, to study the morphology of ZnS growth on MoS_2 that had been drop-casted on a silicon substrate.

3.3 Results and discussion

3.3.1 Exfoliation

Suspensions prepared by surfactant assisted exfoliation show characteristic optical properties of typical MoS_2 suspensions. The presence of CDCA does not alter the properties of the exfoliated MoS_2, in agreement with previous reports using surfactant and biomolecule assisted exfoliation.[4-6] The UV-vis spectrum (Figure 3.2a) shows absorbance peaks at 665 and 605 nm corresponding respectively to the A and B transitions to the split valence band,[7-9] as well as a broad absorbance with peaks at approximately 445 and 400 nm corresponding to the C and D transitions.[5, 10]

Commonly reported PL emission for monolayer MoS_2 of large lateral dimension is between 620-670 nm.[7, 8, 11, 12] However, for these flakes PL spectroscopy (Figure 3.2b) gives a broad, weak emission between 350-450 nm, indicating that the exfoliated material is not made of large monolayer sheets. Such high energy peaks have been reported previously[13-15] for small sized MoS_2 flakes, indicating that the lateral dimensions should be less than 150 nm. However, broad emission indicates polydispersity of sheets' lateral dimensions. The blue shifted peak is ascribed to the hot PL from the K point of the Brillouin zone.[15] The presence of PL indicates the existence of many MoS_2 sheets being less than five monolayers thick.

The thickness of the exfoliated flakes was determined by AFM imaging (Figure 3.3). Measurement of 80 separate flakes resulted in thicknesses of 0.7-2.8 nm, with the majority corresponding to thickness of two layers of MoS_2. To assess the dimensions, a series of TEM images (including Figure 3.2c) were studied, measurements indicate that the sheets span a broad range of sizes from 30 to 500 nm.

Raman spectroscopy (Figure 3.2d) of the suspension drop-cast onto a silicon substrate shows characteristic peaks at 409.5 and 384.7 cm^{-1}.[16, 17] These correspond to the A_{1g} out-of-plane and E^1_{2g} in-plane vibrations respectively. The shift of the E^1_{2g} peak in the suspension sample, compared to the sediment, indicates that the exfoliated flakes are made up of very few layers of MoS_2.[18] The peak that appears with the center at 391 cm^{-1} is associated with partial oxidation of the flakes that occurs during the surfactant assisted exfoliation process.[19]

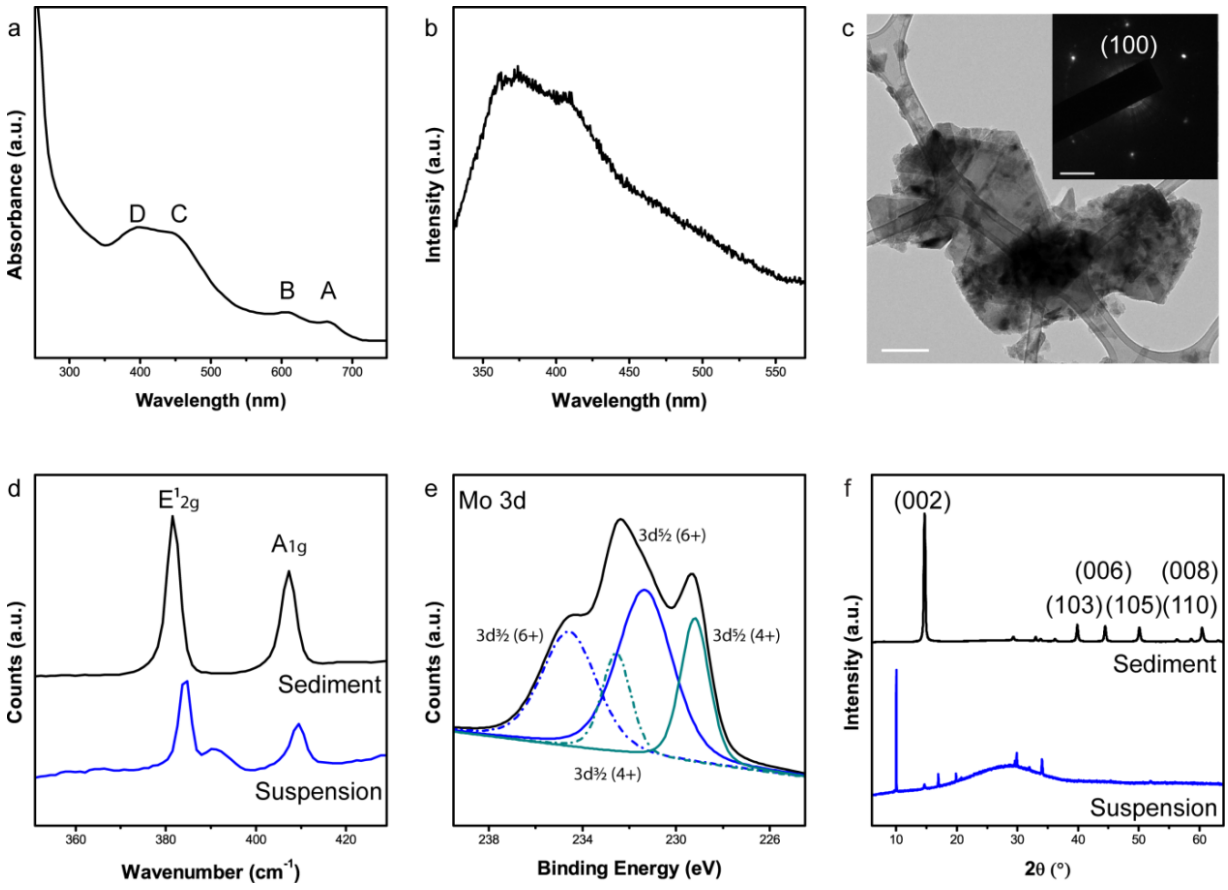

Figure 3.2 Characterisation of the exfoliated MoS_2 suspension: (a) UV-vis spectrum. (b) PL emission spectrum using 300 nm excitation. (c) TEM image of MoS_2 suspension on holey carbon grid, scale bar 200 nm. Inset SAED pattern of the flake in (c) showing (100) diffraction spots, scale bar 2 nm^{-1}. (d) Raman spectrum, of sediment (black) and suspension (blue) from exfoliation, peaks have been normalised by maximum intensity and offset for ease of comparison. (e) XPS trace of Mo 3d energy range with peaks fitted to the Mo^{6+} and Mo^{4+} oxidation states. (f) XRD patterns of sediment (black) and suspension (blue) from exfoliation, peaks have been normalised and offset for comparison.

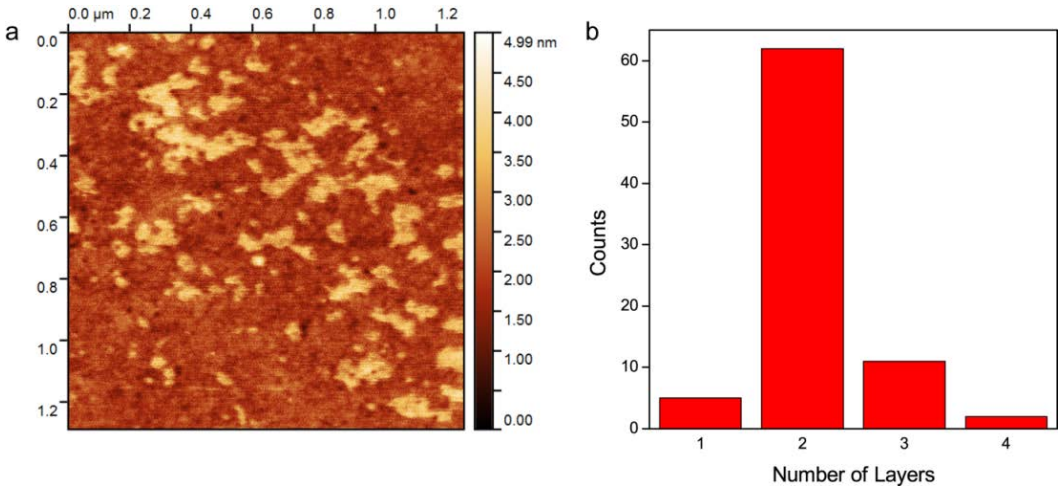

Figure 3.3 AFM characterisation of exfoliated MoS_2. (a) AFM image. (b) Flake height histogram of 80 flakes in (a).

XPS characterisation (Figures 3.2e and 3.4) of the drop-cast flakes on silicon shows two overlapping doublets in the Mo 3d energy range. These are assigned to Mo^{6+} with $3d_{5/2}$ at 231.4 eV and $3d_{3/2}$ at 234.6 eV and the expected Mo^{4+} peaks with $3d_{5/2}$ at 229.2 eV and $3d_{3/2}$ at 232.6 eV for Mo in MoS_2.[8, 20] The presence of Mo 3d peaks for both oxidation states suggests that the sample is partially oxidised, in agreement with the Raman spectrum.

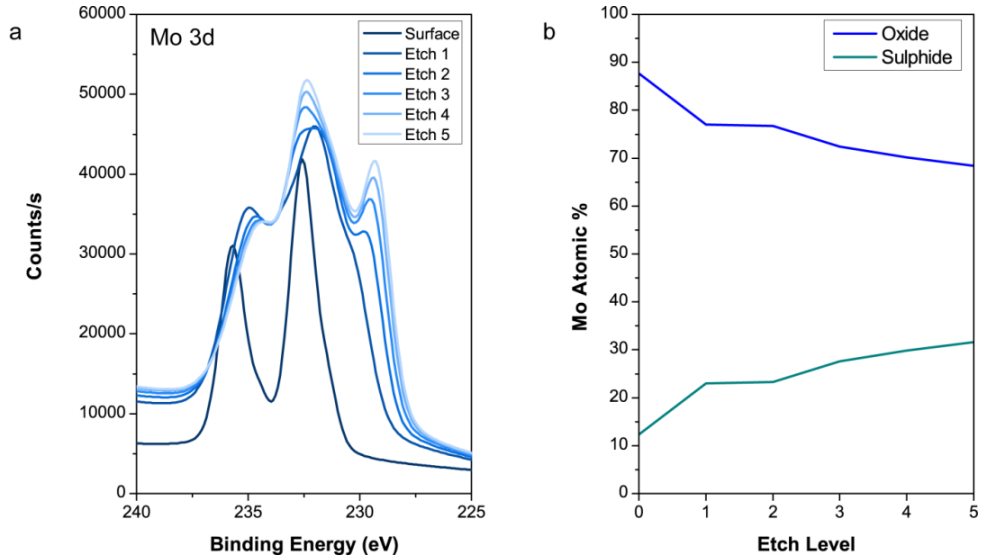

Figure 3.4 XPS etch level analysis of exfoliated MoS_2: (a) Mo 3d energy range at different etch levels showing Mo^{6+} at the surface and the evolution of the peaks for Mo^{4+}. (b) Atomic percentage profile of Mo^{6+} (oxide) and Mo^{4+} (sulphide).

The crystal structure of the material was studied by Wide-Angle XRD (Figure 3.2f). Patterns collected from the sediment MoS_2 (settled by centrifugation of the exfoliation mixture), and the drop-cast suspension of exfoliated MoS_2, differ from each other. The sediment powder closely matches the expected pattern for 2H-MoS_2 (ICCD No. [00-037-1492]). Peaks occur at 14.7˚ (002), 39.9˚ (103), 44.5˚ (006), 50.1˚ (105), 58.6˚ (110) and 60.4˚ (008) in good agreement with the reference pattern. This indicates that there has been no change to the crystal structure of the bulk material during the CDCA assisted exfoliation. However, the film made from suspension of exfoliated flakes gives a diffraction profile that does not match the expected MoS_2 pattern. A relatively large shift of the (002) peak was seen to occur from 14.7° to 9.9°. This change is expected to occur during the exfoliation process as a result of possible insertion of CDCA molecules between the layers, effectively increasing the interlayer spacing of the (002) plane from 0.6 nm to approximately 0.9 nm, which has been

similarly reported by others.[21] Sharp peaks indicate that the flakes are highly crystalline. The broad feature centered at approximately 28° appears due to the glass substrate, it is not an indication of poor crystallinity of the sample itself.

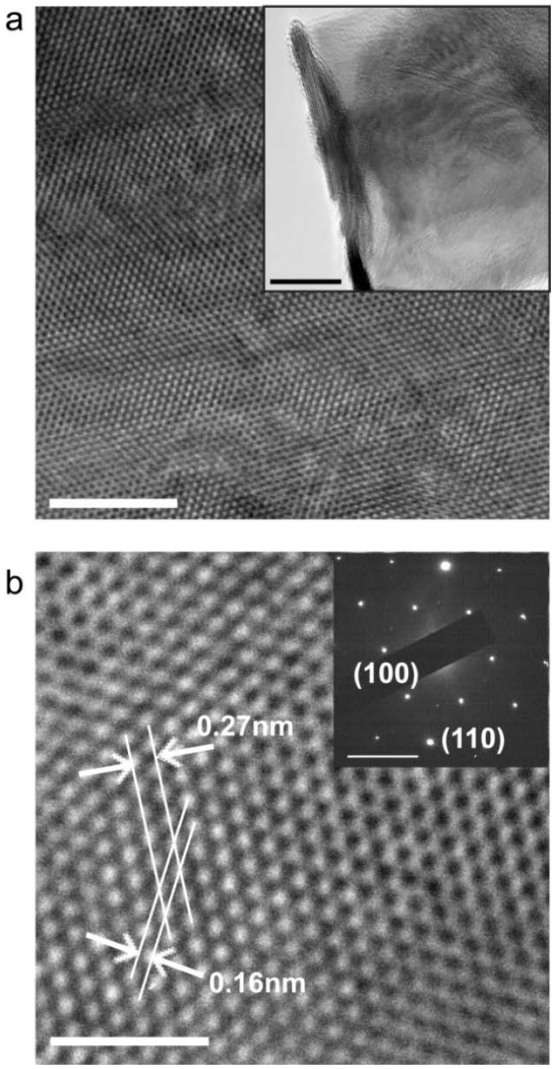

Figure 3.5 HRTEM of exfoliated MoS_2: (a) MoS_2 flake, scale bar 5 nm. Inset lower magnification, scale bar 20 nm. (b) HRTEM showing MoS_2 lattice with characteristic (100) d spacing of 0.27 nm and (110) d spacing of 0.16 nm, scale bar 2 nm. Inset SAED pattern of exfoliated MoS_2 showing diffraction spots for (100) and (110) planes, scale bar 5 nm^{-1}.

Figure 3.5a presents a TEM image of a large exfoliated flake. HRTEM (Figure 3.5b) shows defect free crystal lattice with (100) d spacing of 0.27 nm and (110) d spacing of 0.16 nm,[12] in agreement with the diffraction spots in the selected area electron diffraction (SAED) pattern (Figure 3.5b inset). This confirms that the crystal structure of the suspended flakes was not significantly altered during the surfactant assisted exfoliation.

3.3.2 Hydrothermal processing

The suspension of exfoliated MoS_2 was processed in a hydrothermal reaction, as described in the Experimental section 3.2.2. The resulting MoS_2 QDs were characterised by HRTEM imaging. It was observed that most of the particles have close to 5 nm diameter, however large particles are also observed when the well-defined QDs accumulate together (as shown in section 3.3.3).

The MoS_2 QDs have PL emission at 380 nm, with increased intensity relative to the PL from the suspension of exfoliated flakes (before hydrothermal processing). This break-down to small particles with blue-shifted PL is consistent with previous reports on hydrothermal processing of graphene[22] and solvothermal processing of MoS_2.[23] Interestingly, in this case, the emission wavelength is independent from the excitation wavelength (as discussed in section 3.3.3), in contrast to several previous reports of excitation dependent emission.[24-26]This dependence on excitation wavelength is assigned to polydispersity of the sample, with different sized particles causing different emissions. A recent report of highly monodisperse QDs synthesised from MoS_2 nanoparticles[27] also shows excitation wavelength independent emission.

The relationship between the hydrothermal reaction length and PL intensity was studied. It is observed that initially hydrothermal treatment of the MoS_2 flakes slightly reduces the emission intensity, however longer reaction times (>1.5 hours) increase the emission intensity (Figure 3.6). The intensity is believed to be associated with the number of QD sized particles produced, with longer reaction time causing more complete break-down of the flakes.

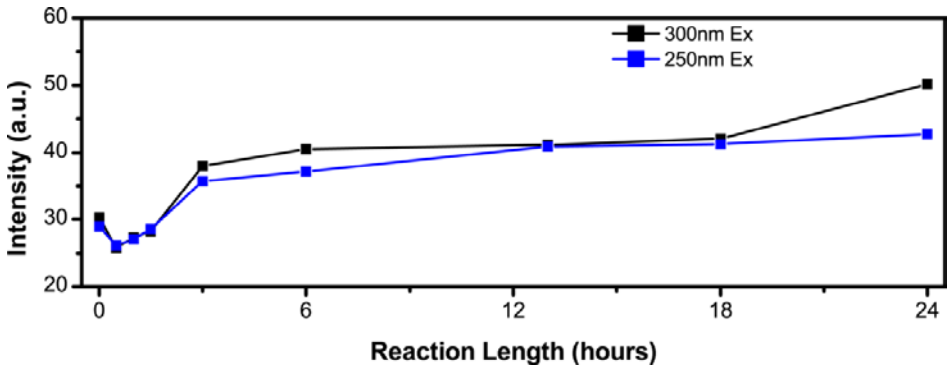

Figure 3.6 PL emission from MoS_2 QDs hydrothermally processed for different lengths of time.

3.3.3 Hydrothermal processing with simultaneous ZnS growth

ZnS was grown separately in the presence of sediment or exfoliated MoS_2 *via* a hydrothermal reaction, using zinc nitrate hexahydrate and L-cysteine as described in the Experimental section 3.2.3.

Sediment MoS_2 was first used for studying the nucleation of ZnS onto larger MoS_2 particles. SEM and TEM characterisations (Figures 3.1c and 3.7) show large (250 nm diameter) ZnS structures forming from small crystallites (5 nm diameter), some of which nucleated on the MoS_2 surface. The SAED (Figure 3.7e) shows hexagonally arranged spots diffracted from the MoS_2 crystal and a ring diffracted from polycrystalline ZnS. Dark field images collect from selecting a single spot and part of the ring (Figures 3.7f and g, respectively) give information about the location of each material in the products. It can be seen that ZnS balls have been formed on the surface of the sediment MoS_2, and that each ball is made up of small randomly oriented crystalline ZnS regions.

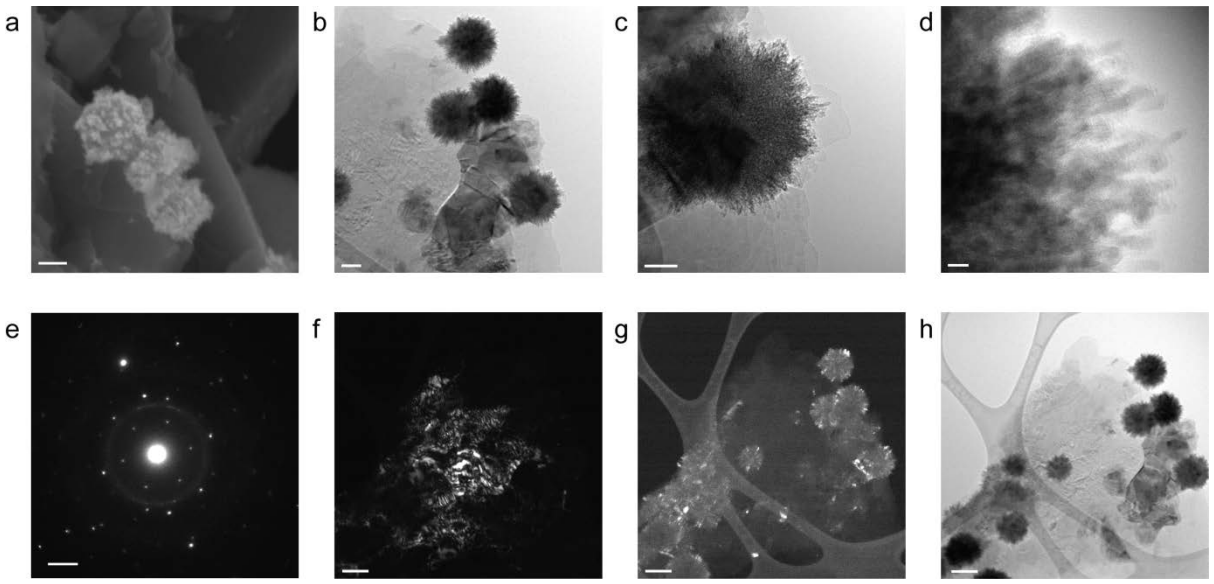

Figure 3.7 Characterisation of hydrothermal reaction precipitates using sediment MoS_2: (a) SEM, scale bar 100 nm. (b) TEM, scale bar 100 nm. (c) TEM, scale bar 50 nm. (d) TEM, scale bar 5 nm. (e) SAED of area shown in (h), scale bar 2 nm^{-1}. (f) Dark field image from spot in (e) showing distribution of MoS_2, scale bar 200 nm. (g) Dark field image from ring in (e) showing distribution of ZnS, scale bar 200 nm. (h) TEM, scale bar 200 nm.

Hydrothermal synthesis of ZnS in the presence of the exfoliated MoS_2 flakes was performed over a broad zinc concentration range as discussed in the Experimental section. The products were centrifuged at 4000 RPM to separate large precipitates (Figures 3.1b) from smaller particles that

remain in suspension (Figure 3.1a). The precipitates were characterised by TEM and XPS (Figures 3.1b and 3.8) and were determined to be ZnS spheres of 200-300 nm diameter. PL spectroscopy (not shown) did not give any significant emission from the precipitates. XPS analysis confirms that these particles don't contain significant amounts of Mo (Figure 3.8c) which indicates that most of the Mo should still be present in the supernatant. As such, the supernatants became the focus of further characterisation to determine if MoS_2-ZnS composites had been successfully produced.

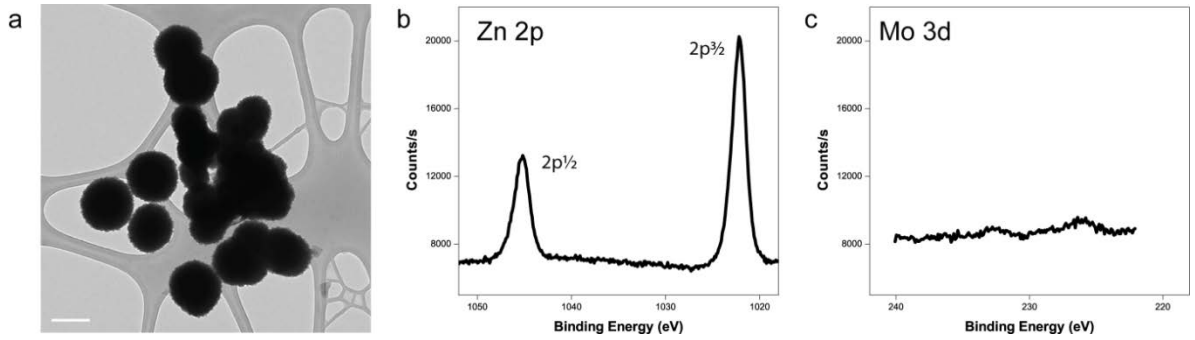

Figure 3.8 Characterisation of hydrothermal reaction precipitates: (a) TEM image showing spheres of 200-300 nm diameter, scale bar 200 nm. (b) XPS trace of Zn 2p energy range. (c) XPS trace of Mo 3d energy range showing absence of Mo.

TEM images of the hydrothermal reaction supernatants (Figures 3.1a and 3.9) show that the ZnS seems to anchor the MoS_2 QDs together to form larger, sub-micron, agglomerates with width 20-30 nm and length <100 nm. The varying zinc concentration doesn't have any major effect on the structure of the particles, however increased amounts of dark regions in the TEM images (Figure 3.9) indicates thicker particles when the ZnS content is increased. Higher magnification of the 1.0 mM sample, using HRTEM (Figure 3.10), shows very small, randomly oriented crystalline regions within the larger structures. Dynamic light scattering (DLS) (Figure 3.10 inset) reveal individual particles with an average diameter of approximately 6 nm.

In Figure 3.11c the interference of two overlapping materials can be clearly seen. When fast Fourier transform (FFT) processing is conducted, two separate hexagons are evident (Figure 3.11d). The diameters of the two rings, 6.1 and 12.5 nm^{-1}, correspond to ZnS (100) and MoS_2 (110), respectively. Applying a mask to each, and performing inverse FFT shows the distribution of each material in the hybrid QD (Figure 3.11e and f). It is believed that the MoS_2 flakes have been broken to monodisperse

QDs as can be seen in Figure 3.11a and, when the precursors are present, ZnS has simultaneously grown on their surface (Figure 3.11b). This morphology is consistent with similar small crystallites which grew on the surface of MoS_2 sediment, joining to form large ZnS balls (Figure 3.7d).

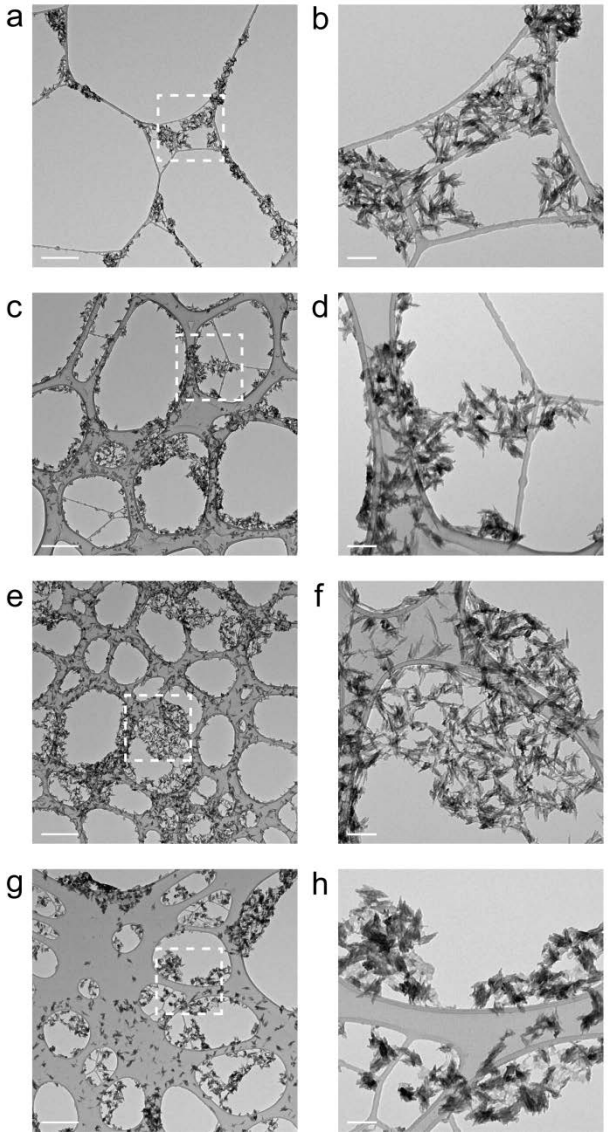

Figure 3.9 TEM characterisation of hydrothermal reaction supernatants: (a, c, e and g) 0.4, 0.6, 0.8 and 1.0 mM samples, scale bars 500 nm. (b, d, f and h) Higher magnification of the outlined square regions in (a, c, e and g), scale bars 100 nm.

It is believed that surface defects on the layered MoS_2 provide sites for nucleation of ZnS. L-cysteine molecules assemble on the MoS_2 surface, and then act as a sulphur source for the growth of ZnS. The synergy of the two hexagonal crystal structures means that ZnS may likely form a layer on top of the MoS_2 basal plane.

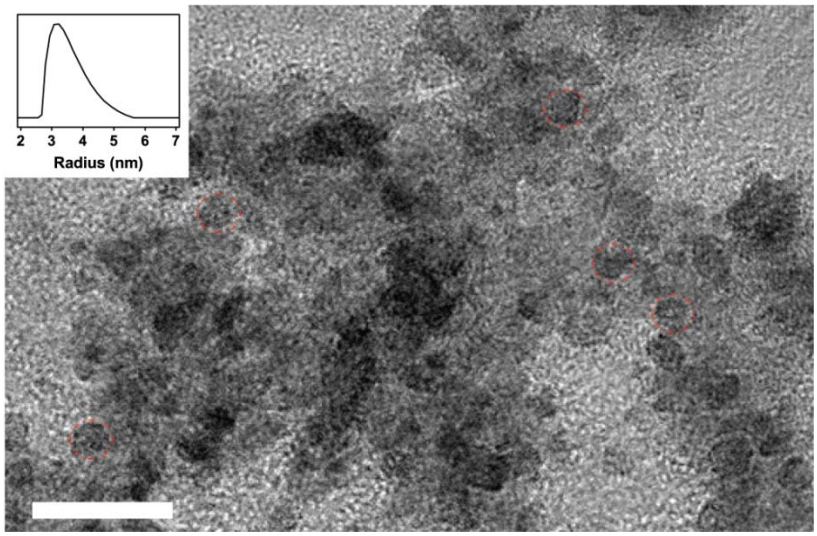

Figure 3.10 HRTEM of 1 mM sample with outlines of some single particles, scale bar 20nm. Inset number weighted radius statistics from DLS of 1 mM sample.

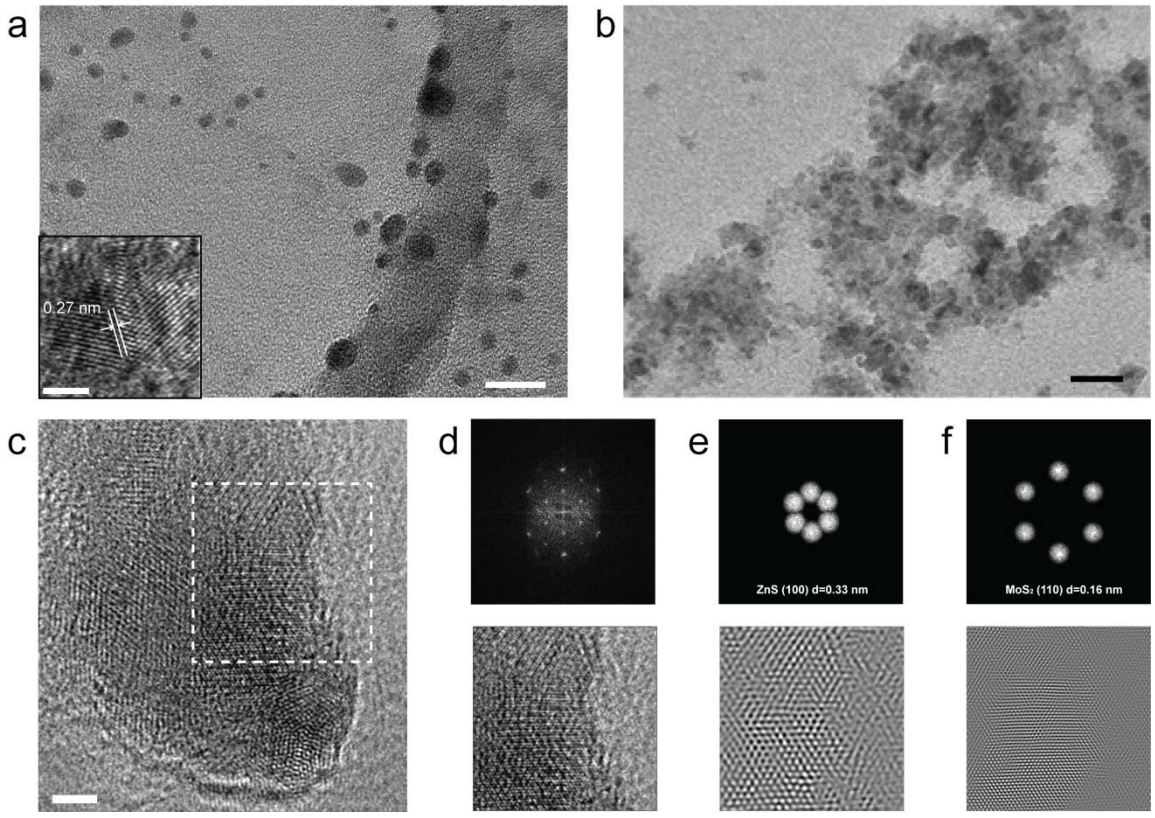

Figure 3.11 HRTEM of hydrothermal reaction supernatants: (a) 0 mM sample, scale bar 20 nm. Inset higher magnification of two particles, scale bar 2 nm. (b) 1.0 mM sample, scale bar 20 nm. (c) Higher magnification of a hybrid MoS_2-ZnS QD in the 1.0 mM sample, scale bar 2 nm. (d) FFT pattern of selected region from (c). (e) Masked region with diameter of 6.1 nm^{-1} and inverse FFT for ZnS (100). (f) Masked region with diameter of 12.5 nm^{-1} and inverse FFT for MoS_2 (110).

The EDX analysis (Figure 3.12a) gives large peaks for copper from the TEM grid. Closer inspection of the baseline (Figure 3.12b-d) shows the presence of molybdenum, sulphur and zinc. The presence of ZnS is confirmed by the XRD pattern which is presented in Figure 3.13.

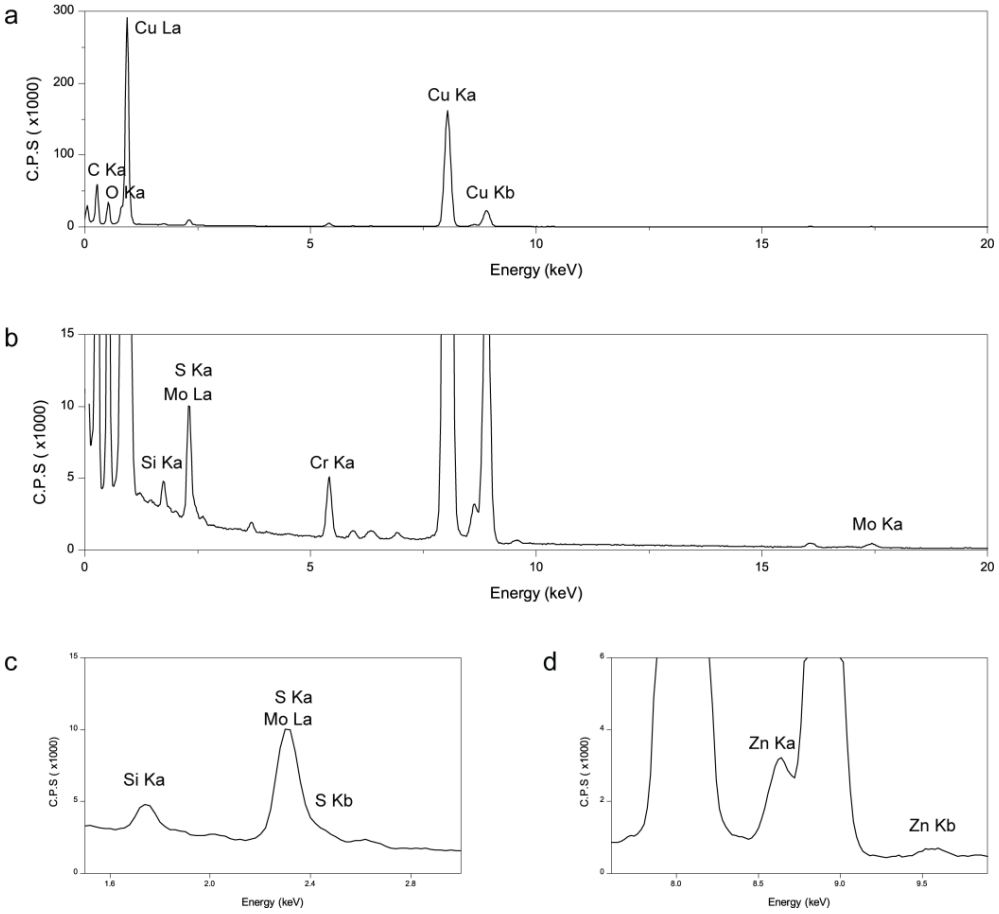

Figure 3.12 EDX analysis of 0.4 mM hydrothermal reaction supernatant: (a) Full analysis energy range. (b) Magnified baseline showing elemental composition. (c) Region showing overlap of the Mo La and S Ka peaks. (d) Region showing Zn peaks close to the intense Cu peaks from the grid.

XPS analysis of the supernatants shows molybdenum to be present in two different oxidation states in all of the samples (Figure 3.14a, d and g). This is due to partial oxidation as previously mentioned. The peak area ratio between the Mo^{6+} (blue) and Mo^{4+} (green) states indicates the extent of oxidation of each sample. Sulphur appears in two different states in all samples (Figure 3.14b, e and h), the peak at 169 eV is due to oxidised material and the peak at 162 eV is due to S^{2-} present in MoS_2 and ZnS. The increased relative intensity of the S^{2-} 2p peak (green) indicates that the sample is more reduced when zinc is present.[8, 28] Zinc is absent in the 0 mM sample, and is present as Zn^{2+} in the other samples (Figure 3.14c, f and i), as expected.

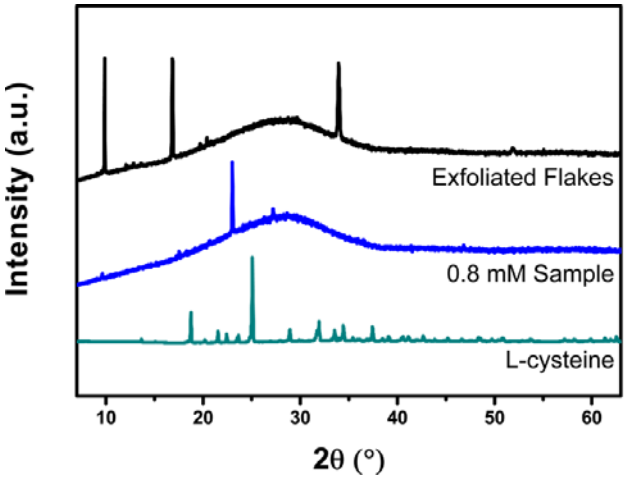

Figure 3.13 XRD patterns of exfoliated MoS_2 flakes (black), 0.8 mM sample (blue) and L-cysteine (green), peaks have been normalized by intensity and offset for ease of comparison. The broad feature centred at approximately 28° is due to the glass substrates. The 0.8 mM sample has peaks at 9.6 and 17.5° from exfoliated MoS_2, and additional peaks at 27.2 and 46.8° from ZnS.[29] Consideration of possible sources found that the prominent peak at 23.0° may be due to unreacted L-cysteine.

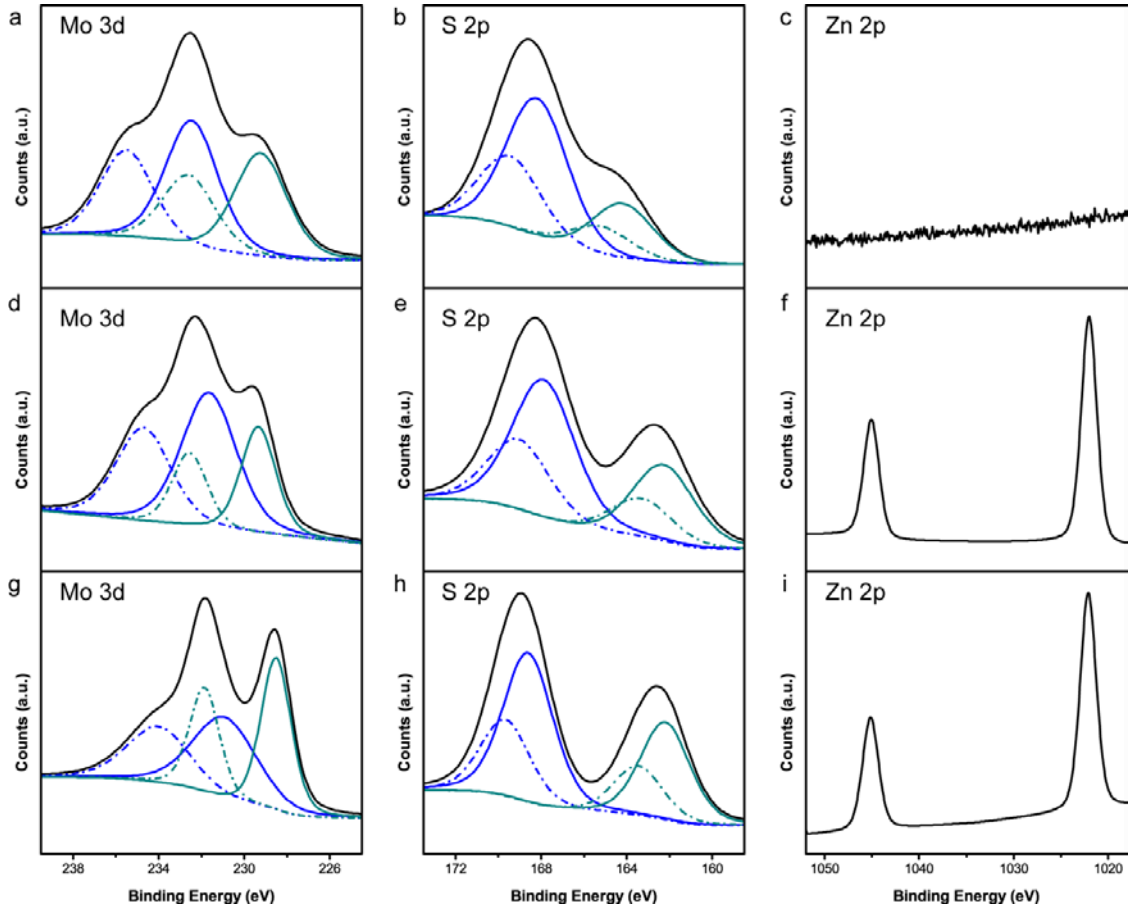

Figure 3.14 XPS characterisation of hydrothermal reaction supernatants: (a, b and c) 0.0 mM, (d, e and f) 0.4 mM, (g, h and i) 1.0 mM samples. Mo^{6+} peaks shown in blue and Mo^{4+} peaks shown in green, $3d_{5/2}$ solid and $3d_{3/2}$ dashed. S^{6+} peaks shown in blue and S^{2-} peaks shown in green, $2p_{3/2}$ solid and $2p_{1/2}$ dashed.

The PL emission from the product supernatants was collected at several excitation wavelengths (Figure 3.15). The emission from each sample was found to be uniform and independent from the excitation wavelength (Figures 3.15 and 3.16a).

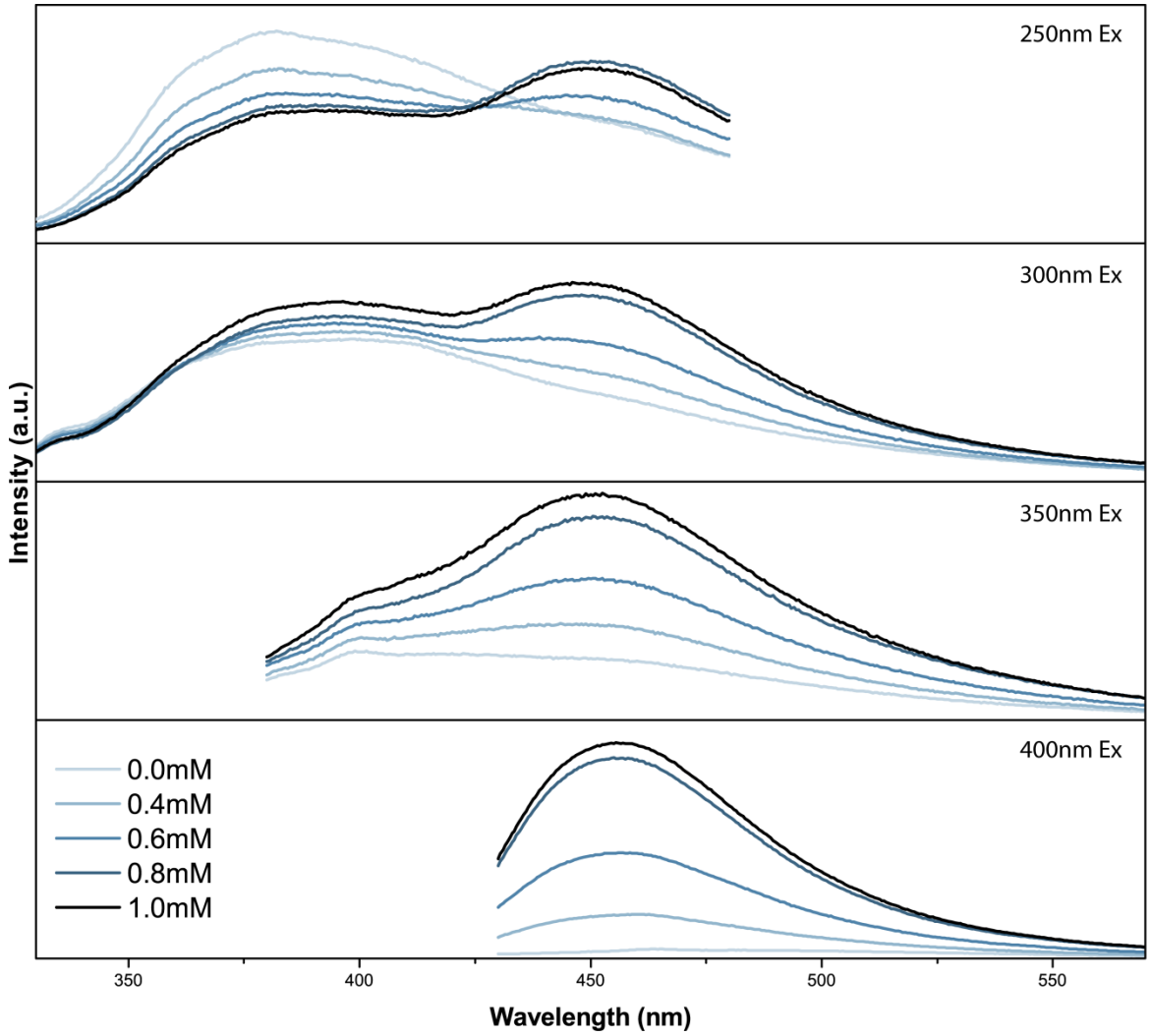

Figure 3.15 PL emission from hydrothermal reaction supernatants at excitation wavelengths of 250, 300, 350 and 400 nm from 0.0, 0.4, 0.6, 0.8 and 1.0 mM samples.

In contrast to a report by Gan *et al.*,[24] PL collected four weeks after my sample preparation gave the same emission wavelength and intensity as the original measurements (Figure 3.16a inset), indicating that the samples are very stable.

Except for the 0 mM sample, that only has one peak centered at 380 nm, all hybrid samples are found to have two peaks around 380 and 450 nm, with the peak intensity varying in samples with different zinc concentration (Figure 3.16b). As the peak at 380 nm (Peak A) is present when there is 0 mM

zinc, it is assigned to the MoS_2 emission. As shown in Figure 3.16c, the intensity of peak A is reasonably unaffected by the zinc concentration from 0.01 to 1 mM with only slight fluctuations, the emission is severely reduced when 5 mM is exceeded. This indicates that the emission from MoS_2 is reduced by the ZnS when in excess, perhaps due to the fact that the majority of photons are absorbed by the ZnS.

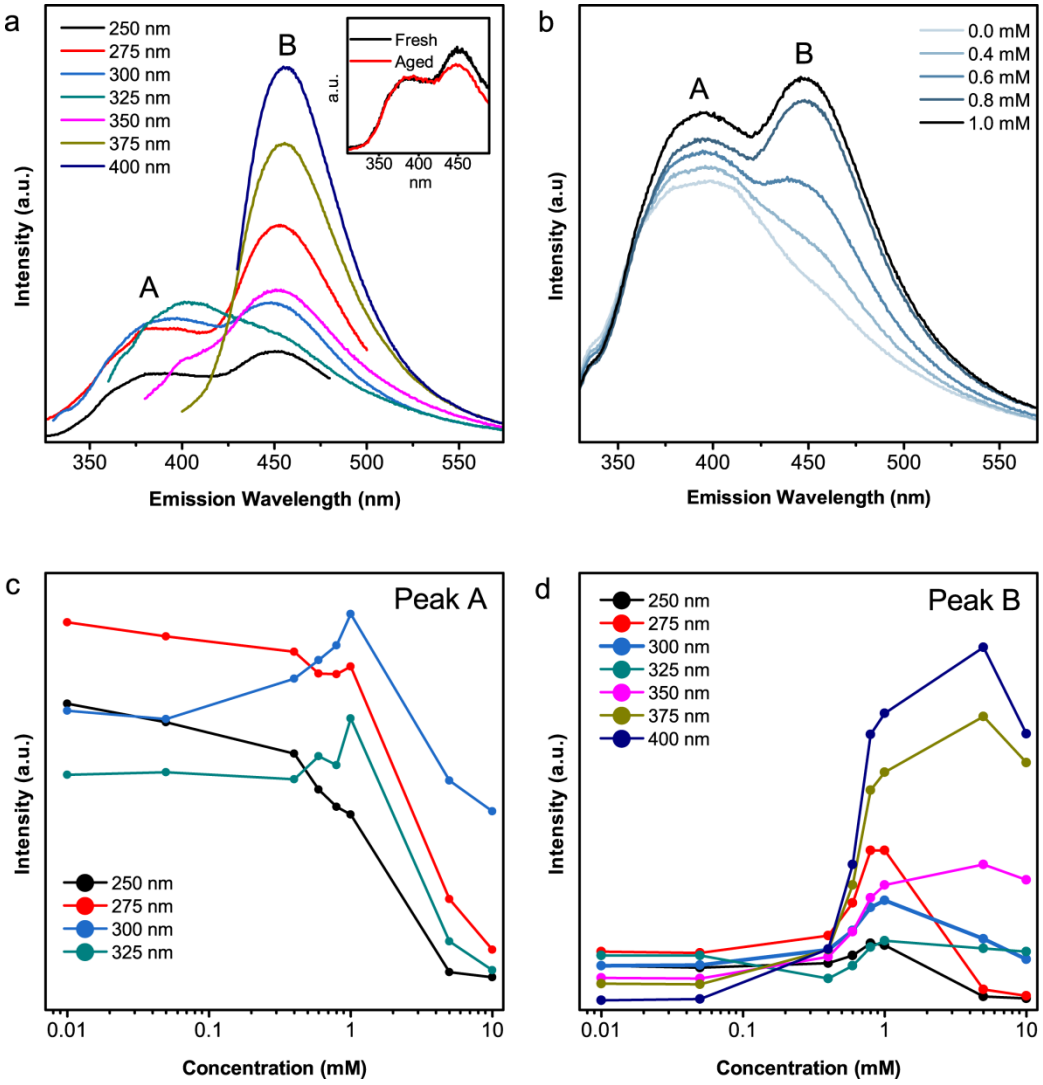

Figure 3.16 PL emission from hydrothermal reaction supernatants: (a) PL emission from 0.8 mM sample with excitation wavelengths of 250, 275, 300, 325, 350, 375 and 400 nm. Inset PL emission from fresh and aged (4 weeks) 0.8 mM sample using 250 nm excitation. (b) PL emission from 0, 0.4, 0.6, 0.8 and 1.0 mM samples, using 300 nm excitation. PL emission from all samples at other excitation wavelengths is presented in Figure S10. (c) Peak A (380 nm emission) intensity as a function of zinc concentration at excitation wavelengths of 250, 275, 300 and 325 nm. (d) Peak B (450 nm emission) intensity as a function of zinc concentration at excitation wavelengths of 250, 275, 300, 325, 350, 375 and 400 nm.

The peak at 450 nm (Peak B) is not present for 0 mM zinc, and increases in intensity as the concentration of zinc is increased (Figure 3.16b). As such, it is expected that peak B is caused by the formation of ZnS onto the MoS_2. PL from ZnS, at wavelengths close to 450 nm, has been recently reported.[29] As shown in Figure 3.16d, the intensity of peak B changes with zinc concentration and the optimum emission intensity is reliant on the excitation wavelength used. For shorter wavelengths, the most intense emission is seen with 1.0 mM zinc. With longer excitation wavelengths, the maximum emission is achieved with 5.0 mM zinc. These results indicate that MoS_2 excitation is competing at shorter wavelengths, but at longer wavelengths the bandgap energy of MoS_2 is not overcome, only ZnS is excited and hence, more emission is produced.

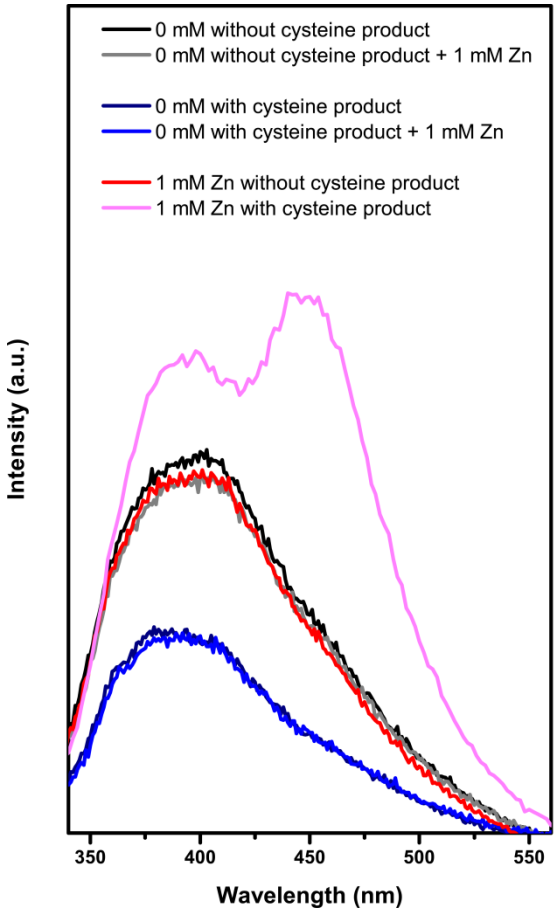

Figure 3.17 PL emission from products, before and after mixing with zinc nitrate hexahydrate.

To confirm that peak B is from the reaction products, and not produced by mixing zinc nitrate hexahydrate with the products, a PL sensitivity test was conducted (as described in the Experimental section 3.2.3). The results (Figure 3.17) indicate that peak B is only present when MoS_2 is processed

with both L-cysteine and zinc nitrate hexahydrate. The peak does not appear when zinc is added to the zinc-free products after the reaction, indicating that the emission at 450 nm is from the product ZnS formed during the hydrothermal reaction.

PL emission from possible by-products of the reaction were ruled out by investigating hydrothermal processing of the surfactant solution without the addition of MoS_2, resulting in no emission (Figure 3.18). ZnS was also grown in the presence of CDCA surfactant solution containing no MoS_2 and this produced luminescent ZnS with lower quantum yield than from either the bare or hybrid QDs (Figure 3.18).

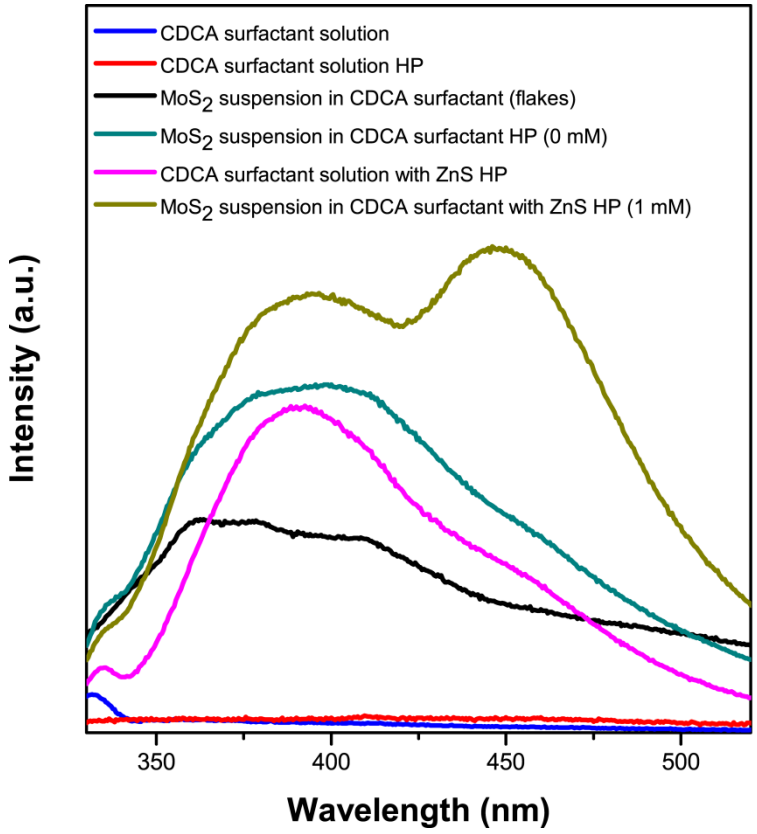

Figure 3.18 PL emission from surfactant solution and product suspensions, where HP stands for hydrothermal processing.

The quantum yield of the 0.8 mM sample was calculated (Table 3.1) to be 1.96%, using quinine sulphate in 0.1 M H_2SO_4 as a reference. This is higher than previously reported (~0.4%) for MoS_2 monolayers[7] and for QDs of MoS_2 synthesised from bulk powder (0.3%)[24] or synthesised from monodisperse nanoparticles (1.3%).[27] The PL quantum yield from the hybrid QDs is much higher than

for the bare MoS_2 QDs or the exfoliated flakes, as can be seen in Figure 3.18. It seems that the presence of ZnS is enhancing the quantum yield by providing an alternative recombination pathway. Such recombination pathways have also been proposed in a core-shell QD study.[30]

Table 3.1 Quantum yield estimations.

Sample	Solvent	Refractive Index	Absorbance at 320 nm	Integrated emission	Quantum Yield
Quinine sulphate	0.1 M H_2SO_4	1.33	0.0937	51806.6	54%[31]
0.8 mM sample	MilliQ	1.33	0.0905	1815.6	1.96%

This simple process for synthesising hybrid QDs with strong PL emission provides a pathway to realising a multitude of optical sensors. Through further functionalisation, it is believed that these materials could become sensitive to a large variety of analytes. The introduction of a double peak in the emission spectrum could provide a means for isolation of the two emission wavelengths, with the possibility of introducing sensitivity at one wavelength and using the other wavelength as a reference standard.

3.4 Conclusions

MoS_2 was exfoliated with a high yield of flakes, in a water and ethanol solution using CDCA surfactant. The hydrothermal processing was shown to break-down the flakes into QDs and result in enhanced optical properties due to quantum confinement. For producing the hybrids, ZnS was formed simultaneously during the hydrothermal process, and has been shown to grow onto large MoS_2 sediment as well as onto MoS_2 QDs. ZnS grew in the form of balls made of small crystallites onto the MoS_2 sediment, but on MoS_2 QDs, ZnS formed thin layers, that sometimes fused the QDs into sub-micron hybrids. The PL from the hybrid QD products is enhanced (maximum quantum yield of

1.96%) compared to the bare MoS_2 flakes or QDs, indicating that this composite material could be potentially useful for effective optical imaging or sensing applications. I have presented the first report on a hydrothermal process for forming MoS_2-ZnS hybrid QDs. Processes may be similarly adopted for forming other metal chalcogenide or oxide compounds onto MoS_2 for obtaining interesting composites with a plethora of functionalities.

In the following chapter, I will investigate methods to deposit colloidal particles into uniform thin films. An alternative to the inconsistent method of drop casting, which provides films of densely-packed particles over large areas, is presented.

3.5 References

1. Wang, Q. H.; Kalantar-Zadeh, K.; Kis, A.; Coleman, J. N.; Strano, M. S. Electronics and optoelectronics of two-dimensional transition metal dichalcogenides. *Nat. Nanotechnol.* **2012,** 7, 699-712.

2. Teo, W. Z.; Chng, E. L. K.; Sofer, Z.; Pumera, M. Cytotoxicity of Exfoliated Transition-Metal Dichalcogenides (MoS_2, WS_2, and WSe_2) is Lower Than That of Graphene and its Analogues. *Chem. -Eur. J.* **2014,** 20, 9627-9632.

3. Clark, R. M.; Carey, B. J.; Daeneke, T.; Atkin, P.; Bhaskaran, M.; Latham, K.; Cole, I. S.; Kalantar-zadeh, K. Two-step synthesis of luminescent MoS_2-ZnS hybrid quantum dots. *Nanoscale* **2015,** 7, 16763-16772.

4. Smith, R. J.; King, P. J.; Lotya, M.; Wirtz, C.; Khan, U.; De, S.; O'Neill, A.; Duesberg, G. S.; Grunlan, J. C.; Moriarty, G.; Chen, J.; Wang, J. Z.; Minett, A. I.; Nicolosi, V.; Coleman, J. N. Large-Scale Exfoliation of Inorganic Layered Compounds in Aqueous Surfactant Solutions. *Adv. Mater.* **2011,** 23, 3944-3948.

5. Li, B. L.; Zou, H. L.; Lu, L.; Yang, Y.; Lei, J. L.; Luo, H. Q.; Li, N. B. Size-Dependent Optical Absorption of Layered MoS_2 and DNA Oligonucleotides Induced Dispersion Behavior for Label-Free Detection of Single-Nucleotide Polymorphism. *Adv. Funct. Mater.* **2015,** 25, 3541-3550.

6. Zhang, W.; Wang, Y.; Zhang, D.; Yu, S.; Zhu, W.; Wang, J.; Zheng, F.; Wang, S.; Wang, J. A one-step approach to the large-scale synthesis of functionalized MoS_2 nanosheets by ionic liquid assisted grinding. *Nanoscale* **2015,** 7, 10210-10217.

7. Mak, K. F.; Lee, C.; Hone, J.; Shan, J.; Heinz, T. F. Atomically Thin MoS_2: A New Direct-Gap Semiconductor. *Phys. Rev. Lett.* **2010,** 105, 136805.

8. Eda, G.; Yamaguchi, H.; Voiry, D.; Fujita, T.; Chen, M.; Chhowalla, M. Photoluminescence from Chemically Exfoliated MoS_2. *Nano Lett.* **2011,** 11, 5111-5116.

9. Butler, S. Z.; Hollen, S. M.; Cao, L. Y.; Cui, Y.; Gupta, J. A.; Gutierrez, H. R.; Heinz, T. F.; Hong, S. S.; Huang, J. X.; Ismach, A. F.; Johnston-Halperin, E.; Kuno, M.; Plashnitsa, V. V.; Robinson, R. D.; Ruoff, R. S.; Salahuddin, S.; Shan, J.; Shi, L.; Spencer, M. G.; Terrones, M.; Windl, W.;

Goldberger, J. E. Progress, Challenges, and Opportunities in Two-Dimensional Materials Beyond Graphene. *ACS Nano* **2013,** 7, 2898-2926.

10. Wilcoxon, J. P.; Newcomer, P. P.; Samara, G. A. Synthesis and optical properties of MoS_2 and isomorphous nanoclusters in the quantum confinement regime. *J. Appl. Phys.* **1997,** 81, 7934-7944.

11. Ji, Q. Q.; Zhang, Y. F.; Gao, T.; Zhang, Y.; Ma, D. L.; Liu, M. X.; Chen, Y. B.; Qiao, X. F.; Tan, P. H.; Kan, M.; Feng, J.; Sun, Q.; Liu, Z. F. Epitaxial Monolayer MoS_2 on Mica with Novel Photoluminescence. *Nano Lett.* **2013,** 13, 3870-3877.

12. Liu, Y. L.; Nan, H. Y.; Wu, X.; Pan, W.; Wang, W. H.; Bai, J.; Zhao, W. W.; Sun, L. T.; Wang, X. R.; Ni, Z. H. Layer-by-Layer Thinning of MoS_2 by Plasma. *ACS Nano* **2013,** 7, 4202-4209.

13. Wang, Y. C.; Ou, J. Z.; Balendhran, S.; Chrimes, A. F.; Mortazavi, M.; Yao, D. D.; Field, M. R.; Latham, K.; Bansal, V.; Friend, J. R.; Zhuiykov, S.; Medhekar, N. V.; Strano, M. S.; Kalantar-zadeh, K. Electrochemical Control of Photoluminescence in Two-Dimensional MoS_2 Nanoflakes. *ACS Nano* **2013,** 7, 10083-10093.

14. Nguyen, E. P.; Carey, B. J.; Daeneke, T.; Ou, J. Z.; Latham, K.; Zhuiykov, S.; Kalantar-zadeh, K. Investigation of Two-Solvent Grinding-Assisted Liquid Phase Exfoliation of Layered MoS_2. *Chem. Mater.* **2015,** 27, 53-59.

15. Ou, J. Z.; Chrimes, A. F.; Wang, Y. C.; Tang, S. Y.; Strano, M. S.; Kalantar-zadeh, K. Ion-Driven Photoluminescence Modulation of Quasi-Two-Dimensional MoS_2 Nanoflakes for Applications in Biological Systems. *Nano Lett.* **2014,** 14, 857-863.

16. Ganatra, R.; Zhang, Q. Few-Layer MoS_2: A Promising Layered Semiconductor. *ACS Nano* **2014,** 8, 4074-4099.

17. Li, H.; Zhang, Q.; Yap, C. C. R.; Tay, B. K.; Edwin, T. H. T.; Olivier, A.; Baillargeat, D. From Bulk to Monolayer MoS_2: Evolution of Raman Scattering. *Adv. Funct. Mater.* **2012,** 22, 1385-1390.

18. Lee, C.; Yan, H.; Brus, L. E.; Heinz, T. F.; Hone, J.; Ryu, S. Anomalous Lattice Vibrations of Single- and Few-Layer MoS_2. *ACS Nano* **2010,** 4, 2695-2700.

19. Murugan, R.; Ghule, A.; Bhongale, C.; Chang, H. Thermo-Raman investigations on structural transformations in hydrated MoO_3. *J. Mater. Chem.* **2000,** 10, 2157-2162.

20. Kim, I. S.; Sangwan, V. K.; Jariwala, D.; Wood, J. D.; Park, S.; Chen, K. S.; Shi, F. Y.; Ruiz-Zepeda, F.; Ponce, A.; Jose-Yacaman, M.; Dravid, V. P.; Marks, T. J.; Hersam, M. C.; Lauhon, L. J. Influence of Stoichiometry on the Optical and Electrical Properties of Chemical Vapor Deposition Derived MoS_2. *ACS Nano* **2014,** 8, 10551-10558.

21. Jeong, S.; Yoo, D.; Ahn, M.; Miro, P.; Heine, T.; Cheon, J. Tandem intercalation strategy for single-layer nanosheets as an effective alternative to conventional exfoliation processes. *Nat. Commun.* **2015,** 6, 5763.

22. Pan, D. Y.; Zhang, J. C.; Li, Z.; Wu, M. H. Hydrothermal Route for Cutting Graphene Sheets into Blue-Luminescent Graphene Quantum Dots. *Adv. Mater.* **2010,** 22, 734-738.

23. Xu, S. J.; Li, D.; Wu, P. Y. One-Pot, Facile, and Versatile Synthesis of Monolayer MoS_2/WS_2 Quantum Dots as Bioimaging Probes and Efficient Electrocatalysts for Hydrogen Evolution Reaction. *Adv. Funct. Mater.* **2015,** 25, 1127-1136.

24. Gan, Z. X.; Liu, L. Z.; Wu, H. Y.; Hao, Y. L.; Shan, Y.; Wu, X. L.; Chu, P. K. Quantum confinement effects across two-dimensional planes in MoS_2 quantum dots. *Appl. Phys. Lett.* **2015,** 106, 233113.

25. Li, B. L.; Chen, L. X.; Zou, H. L.; Lei, J. L.; Luo, H. Q.; Li, N. B. Electrochemically induced Fenton reaction of few-layer MoS_2 nanosheets: preparation of luminescent quantum dots via a transition of nanoporous morphology. *Nanoscale* **2014,** 6, 9831-9838.

26. Gopalakrishnan, D.; Damien, D.; Li, B.; Gullappalli, H.; Pillai, V. K.; Ajayan, P. M.; Shaijumon, M. M. Electrochemical synthesis of luminescent MoS_2 quantum dots. *Chem. Commun.* **2015,** 51, 6293-6296.

27. Ha, H. D.; Han, D. J.; Choi, J. S.; Park, M.; Seo, T. S. Dual Role of Blue Luminescent MoS_2 Quantum Dots in Fluorescence Resonance Energy Transfer Phenomenon. *Small* **2014,** 10, 3858-3862.

28. Chou, S. S.; Kaehr, B.; Kim, J.; Foley, B. M.; De, M.; Hopkins, P. E.; Huang, J.; Brinker, C. J.; Dravid, V. P. Chemically Exfoliated MoS_2 as Near-Infrared Photothermal Agents. *Angew. Chem. , Int. Ed.* **2013,** 52, 4160-4164.

29. Wang, G.; Huang, B.; Li, Z.; Lou, Z.; Wang, Z.; Dai, Y.; Whangbo, M.-H. Synthesis and characterization of ZnS with controlled amount of S vacancies for photocatalytic H_2 production under visible light. *Sci. Rep.* **2015,** 5, 8544.

30. Nam, D. E.; Song, W. S.; Yang, H. Noninjection, one-pot synthesis of Cu-deficient $CuInS_2$/ZnS core/shell quantum dots and their fluorescent properties. *J. Colloid Interface Sci.* **2011,** 361, 491-496.

31. Melhuish, W. H. Quantum efficiencies of fluorescence of organic substances: Effect of solvent and concentration of the fluorescent solute. *J. Phys. Chem.* **1961,** 65, 229-235.

Chapter 4

Patterned films from exfoliated two-dimensional transition metal dichalcogenides assembled at a liquid-liquid interface

4.1 Introduction

The translation of exfoliated nanoflake suspensions into useable films is currently a matter of intense investigation, to develop reliable and scalable printing and patterning methods.[1] A more reliable deposition technique is explored, in order to provide an alternative to traditional methods such as drop casting and spin coating.[2-5] The controlled deposition and patterning of macroscopic thin films from exfoliated transition metal dichalcogenides (TMDs) is investigated, using a liquid-liquid interface method.

In this chapter, I report a facile method where an interface is formed directly using the suspension of exfoliated TMDs. I show that this method works successfully for the two most common TMDs, molybdenum disulphide (MoS_2) and tungsten disulphide (WS_2). I also investigate controlled deposition by implementing a range of patterned substrates. Finally, composite films were also achieved by the incorporation of different TMDs into mixed films. Mixing two suspensions prior to film assembly provides a simple pathway to forming a heterofilm.

The new method produces concentrated, close-packed films with good uniformities which can be deposited in a controlled pattern over relatively large surface areas.

The contents of this chapter have been published as an article in Journal of Materials Chemistry C.[6]

4.2 Experimental details

4.2.1 Materials

Molybdenum disulphide (99.9%) was purchased from US Nano and rhenium disulphide (99%) was purchased from Alfa Aesar. Tungsten disulphide (99%), dimethyl formamide (DMF) (99.8%), octadecene (ODE) (90%) and 1H, 1H, 2H, 2H-Perfluorodecyl triethoxysilane (PFDTES) (97%) were purchased from Sigma Aldrich.

4.2.2 Exfoliation

Suspensions of TMDs were prepared in DMF. In brief, the bulk TMD powders were ground in a mortar and pestle with 2 mL DMF for 15 minutes before suspending in further 10 mL of DMF. The mixtures were then probe sonicated for 90 minutes with an on-off pulse ratio of 25:5 seconds. The mixture is then centrifuged at 2500 RCF for 60 minutes to remove remaining the bulk powders, and the suspensions of nanosheets were extracted.

4.2.3 Liquid-liquid interface

Octadecene was added to the nanoflake suspensions and the mixtures were shaken (Figure 4.1). When allowed to settle, these nanoflakes assembled at the liquid-liquid interface (Figure 4.1). These samples

were stored in plastic tubes because, when stored in glass, the particles were attracted to the walls of the vial. The assembled films were directly extracted from the liquid-liquid interface by dipping substrates into the interfaces (Figure 4.1), the substrates were dried on a hotplate at 90°C to evaporate solvent and increase the adherence of the films to the substrates.

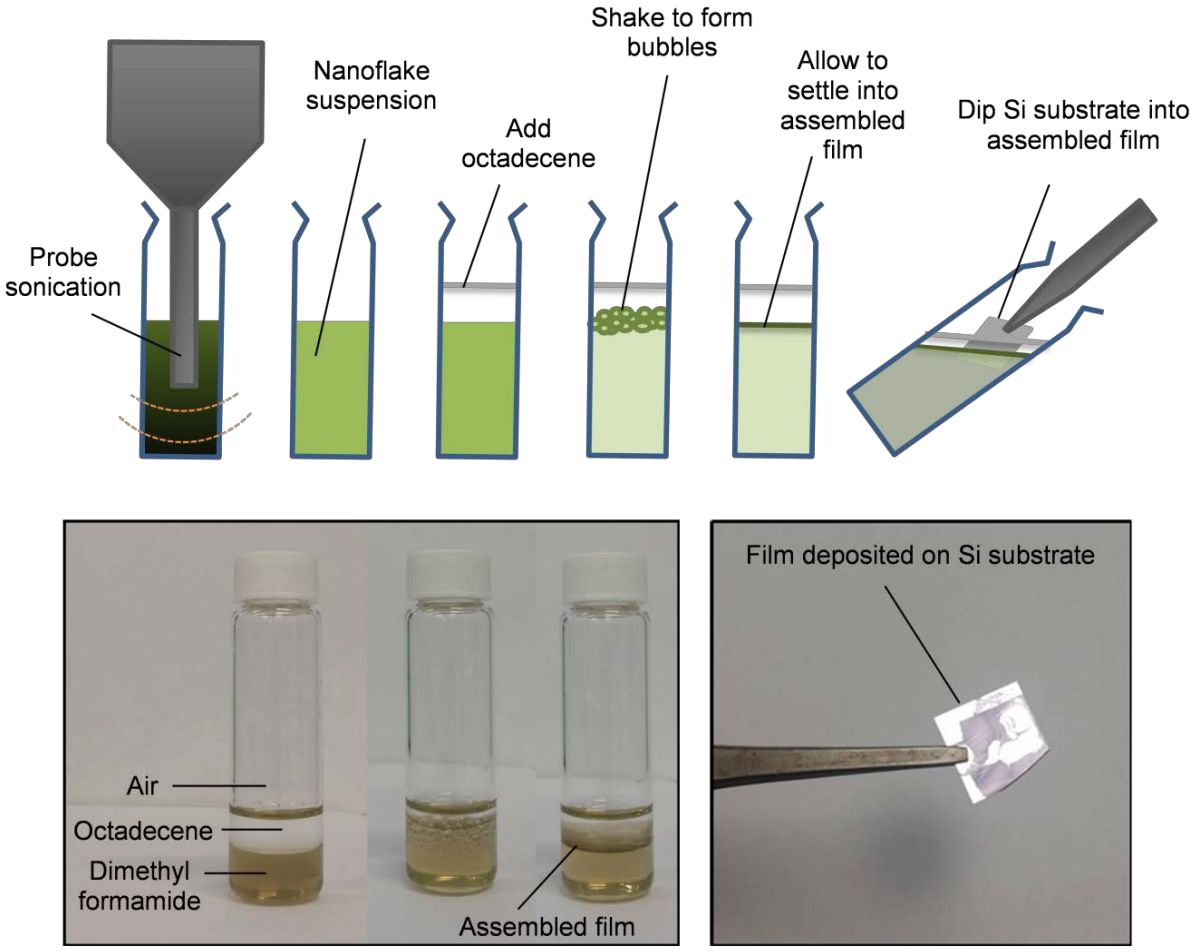

Figure 4.1 Method schematic showing exfoliation, liquid-liquid interface formation, film assembly and film deposition by dip technique.

4.2.4 Substrate patterning

Controlled patterned films are produced by first forming hydrophobic-hydrophilic patterned substrates (Figure 4.2), as reported previously by our group.[7] Photolithography is used to create a patterned photoresist, followed by exposure to PFDTES for hydrophobic treatment. The photoresist is then removed, to uncover the non-treated areas. (Figure 4.2)

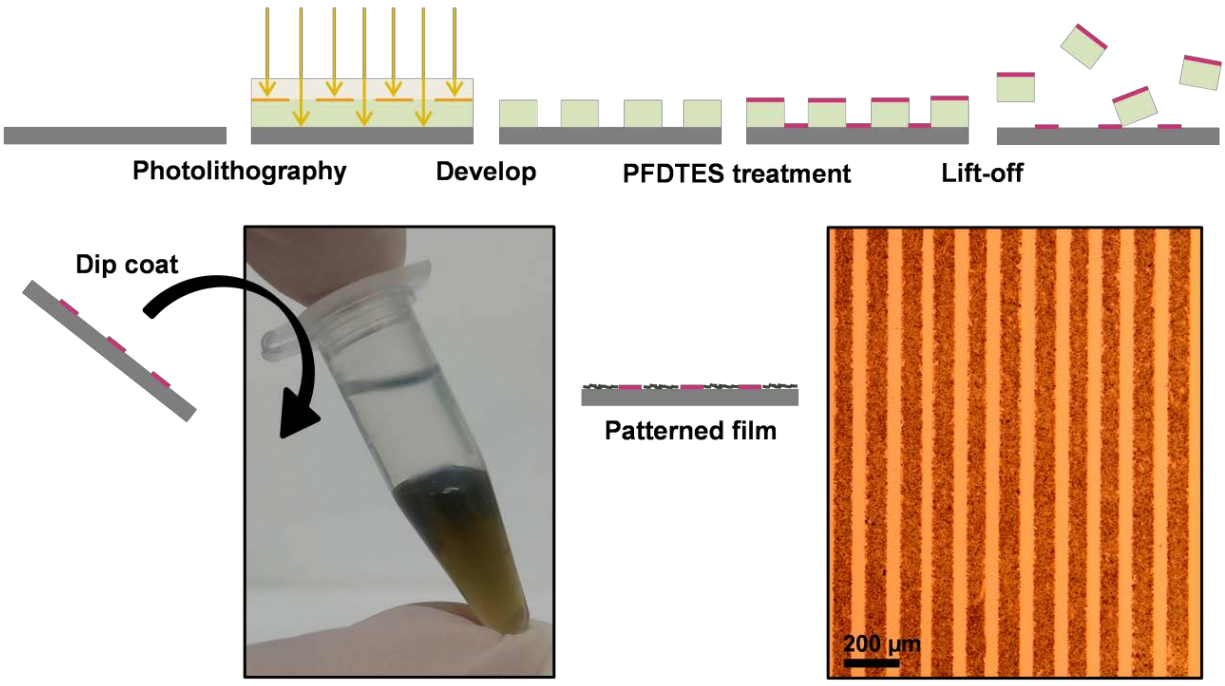

Figure 4.2 Substrate patterning technique schematic showing photolithography, hydrophobic treatment and patterned film deposition. Optical image of the resulting striped MoS_2 patterned film.

4.2.5 Characterisation

The prepared films were studied by optical and electron microscopy, Raman spectroscopy and x-ray diffraction (XRD). Films were deposited on various substrates for characterisation. The transition electron microscopy (TEM) sample was prepared by collecting a section of the suspended film using a small wire loop. The particles were allowed to reassemble and the film was transferred by lowering the wire loop onto a carbon coated TEM grid. TEM was conducted using a JEOL 1010 instrument (100 kV). Zeta potential measurements were performed using a Malvern Nano ZS zetasizer. Raman and photoluminescence (PL) spectroscopy were conducted with a Horiba Scientific LabRAM HR evolution system using a 532 nm laser. XRD patterns were collected from films dried on glass, using a Bruker D4 Endeavour with Cu Kα radiation of 1.5406 Å. Optical images were collected using a Leica DM2500 M microscope with CCD camera. An FEI Quanta scanning electron microscope (SEM) was used for SEM imaging. Atomic force microscopy (AFM) was performed using a Bruker Dimension Icon in tapping mode.

4.3 Results and discussion

4.3.1 Nanoflake assembly

Suspensions of exfoliated two-dimensional (2D) MoS_2, WS_2 and ReS_2 were prepared by grinding and then probe sonication in DMF. The liquid-liquid interface particle assembly is achieved by combining the nanoflake suspensions with ODE, there are no further chemical initiators or solvents introduced to the mixture. When ODE is added and the mixture is shaken, as shown in Figure 4.1, the particles assemble at the liquid-liquid interface formed between DMF and ODE. Initially, when the ODE is added to the top of the nanoflake suspension, there is no apparent film formation at the interface between the two solvents. Shaking the mixture causes bubbles and increases the interaction surface area, allowing the ODE to interact more efficiently with the suspension. The suspended nanoflakes are drawn to the liquid-liquid interface, resulting in a coating of nanoflakes on the surface of the bubbles. When the mixture is allowed to settle and the bubbles burst, the nanoflakes are confined at the uniform planar liquid-liquid interface, as displayed in Figure 4.1.

The nanoflakes assemble at the interface and can be densely-packed to form a saturated surface due to the overall decrease in the interfacial surface energy.[8-10] Capillary forces arising from the electric field surrounding the particles at a polar/non-polar interface help to stabilise the attraction-repulsion interaction between like particles.[11] It is believed that 2D nanomaterials behave differently to spherical nanoparticles at a liquid-liquid interface, because they are confined to movement in the plane of the interface and are not able to rotate out of plane.[12] This possible planar edge-to-edge assembly results in a reduction in the liquid-liquid interfacial area, and occurs spontaneously to form a stable lower energy arrangement. The assembled films were extracted from the liquid-liquid interface for further analysis and characterisation.

For comparison, TEM analysis of the nanoflake suspensions drop-cast onto carbon coated grids (Figure 4.3a and e) shows several particles dispersed in a random fashion. When the assembled films are deposited onto TEM grids (Figure 4.3b, c, f and g) long range order is observed in the arrangement of the particles into densely packed films. It seems that edge-to-edge repulsion mostly

prevents restacking of the flakes,[13] and results in a thin film of individual particles for MoS_2 (Figure 4.3b and c) and WS_2 (Figure 4.3f and g). ReS_2 nanoflakes were found to agglomerate at the interface and not form large scale thin films, as displayed in Figure 4.4. The inset selected area electron diffraction (SAED) patterns confirm the crystallinity of the flakes in the films, with spots corresponding to the (100) and (110) planes.

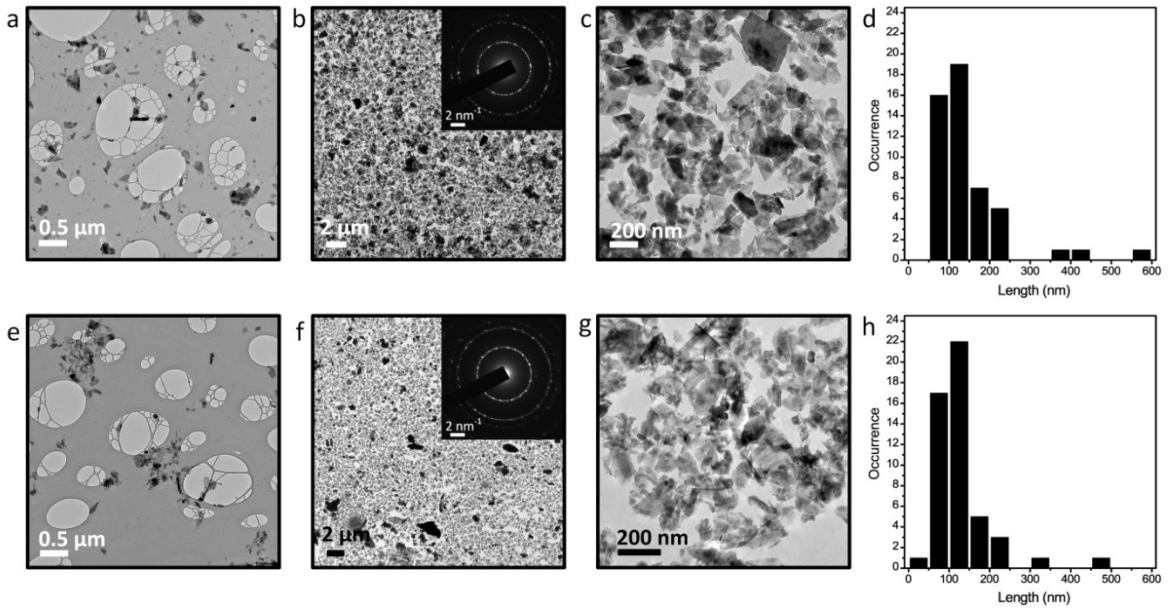

Figure 4.3 TEM analysis of a-d) MoS_2 and e-h) WS_2. a and e), drop cast exfoliated nanoflakes. b and f), low magnification of assembled films showing coverage (inset SAED patterns). c and g), higher magnification of films showing particle assembly. d and h), histograms of the lateral dimensions of the nanoflakes.

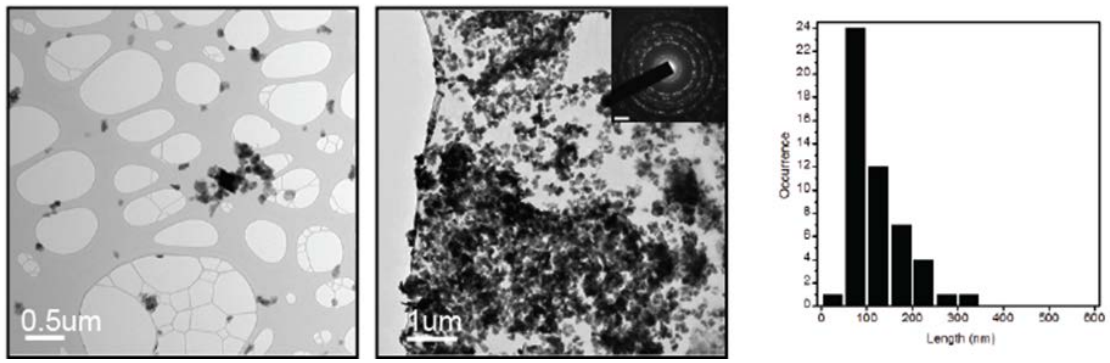

Figure 4.4 TEM of ReS_2 suspension and assembled film, showing agglomeration.

Measurements of the lateral dimensions of the exfoliated nanoflakes (Figure 4.3d and h) show that the majority of the flakes fall within the range of 50-250 nm for each material.

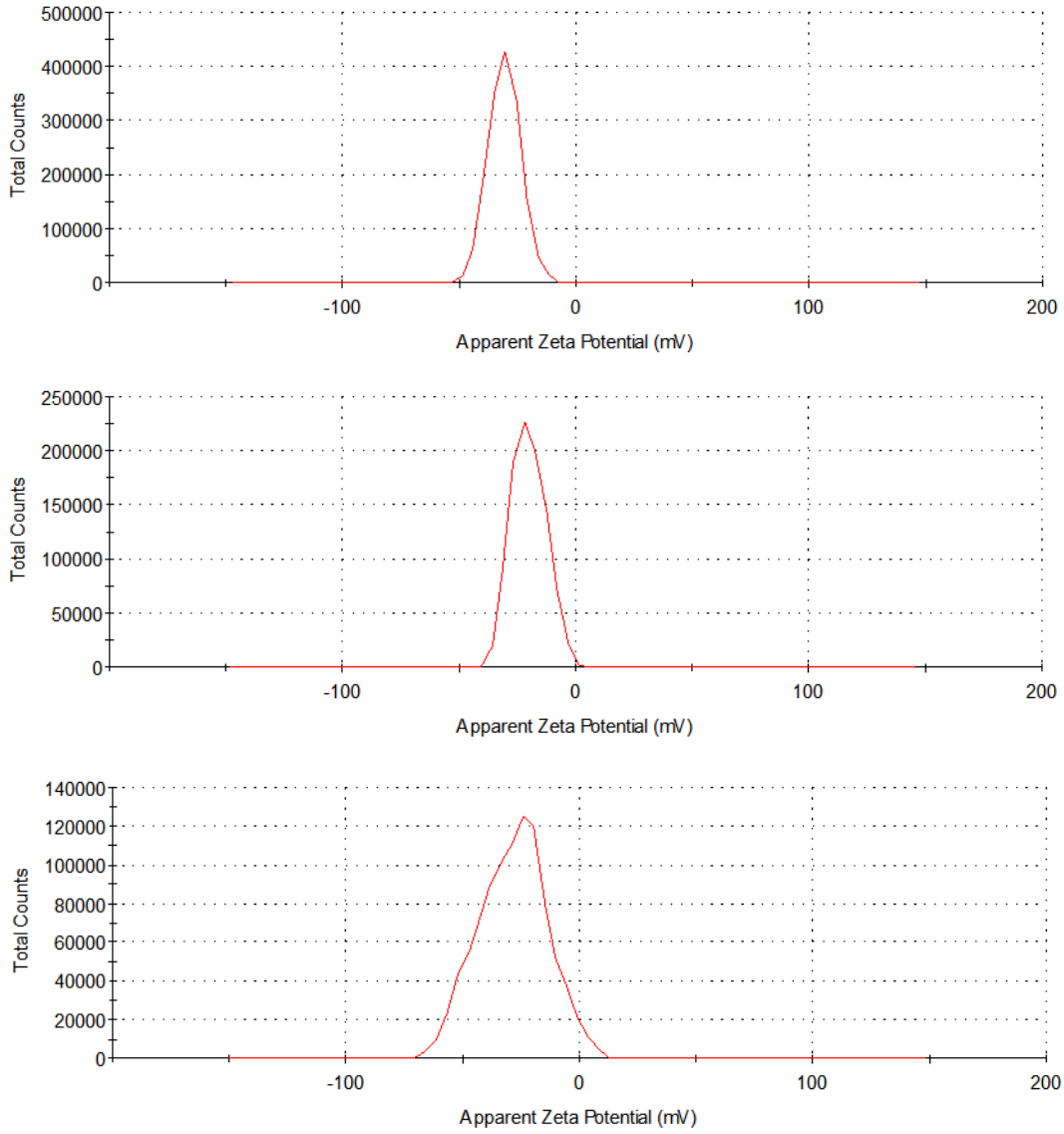

Figure 4.5 Zeta potential measurements for MoS_2, WS_2 and ReS_2 suspended in DMF.

Zeta potential measurements (Figure 4.5) were performed to further study the behaviour of the nanoflakes suspended in DMF. For MoS_2 and WS_2 sharp peaks were observed centred at values of -31.3 and -20.5 mV, respectively. The measurement for ReS_2 gave a broad peak centred at -28.4 mV, which spanned from positive values down as far as -70 mV. This broad zeta potential range indicates instability and is expected to be responsible for the agglomeration of ReS_2. The stability of the assembled films should be easily controlled by addition of stabilising surfactant ligands. However in this investigation any chemical modification was avoided to maintain the optical and electrical properties of the flakes, in order to obtain films of desired qualities for functional applications.

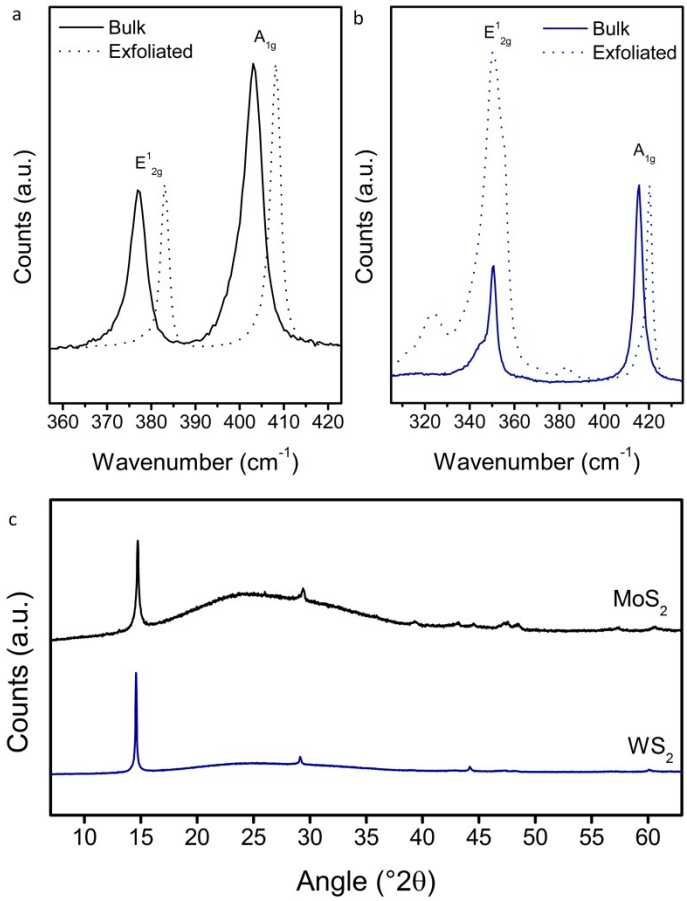

Figure 4.6 Raman spectra of a) MoS_2 and b) WS_2 bulk (solid lines) and exfoliated (dotted lines). c) XRD patterns of assembled films of MoS_2 (black) and WS_2 (blue). Data has been normalised for comparison.

The exfoliated TMDs were drop cast on Si substrates and characterised by Raman spectroscopy, as shown in Figure 4.6a and b. The exfoliated MoS_2 shows Raman peaks shifted compared to the bulk powder. Sharp peaks appear at 383.0 and 408.1 cm^{-1}, which correspond to the E^1_{2g} and A_{1g} peaks respectively. The gap between the two peaks is 26.1 cm^{-1} in the bulk, and reduces to 25.1 cm^{-1} in the exfoliated flakes. The shift of the E^1_{2g} peak to a higher wavenumber is associated with the sheet thickness reduction, however the location of the A_{1g} vibrational band in the bulk powder appears at a lower wavenumber than previously reported.[14, 15] Overall, a reduction of one wavenumber in the distance between the Raman peaks indicates that the nanoflakes should be no thicker than 5 layers.[15] The Raman peaks of WS_2 appear at 350.2 cm^{-1} for the E_{2g} and 420.1 cm^{-1} for the A_{1g} peaks, as reported previously.[16] The shift of the A_{1g} peak from 416.0 to 420.1 cm^{-1}, along with the A_{1g}: E^1_{2g} peak intensity ratio increase from 0.6 to 1.6 are indicators of ultrathin WS_2. This peak intensity ratio is

indicative of ultrathin WS_2 with no more than 2 fundamental layers.[16] As shown in Figure 4.7, the ReS_2 Raman peaks are observed at 151.8, 161.1 and 212.2 cm^{-1}, matching previously observed peaks for E_g and A_g-like vibrations.[17, 18]

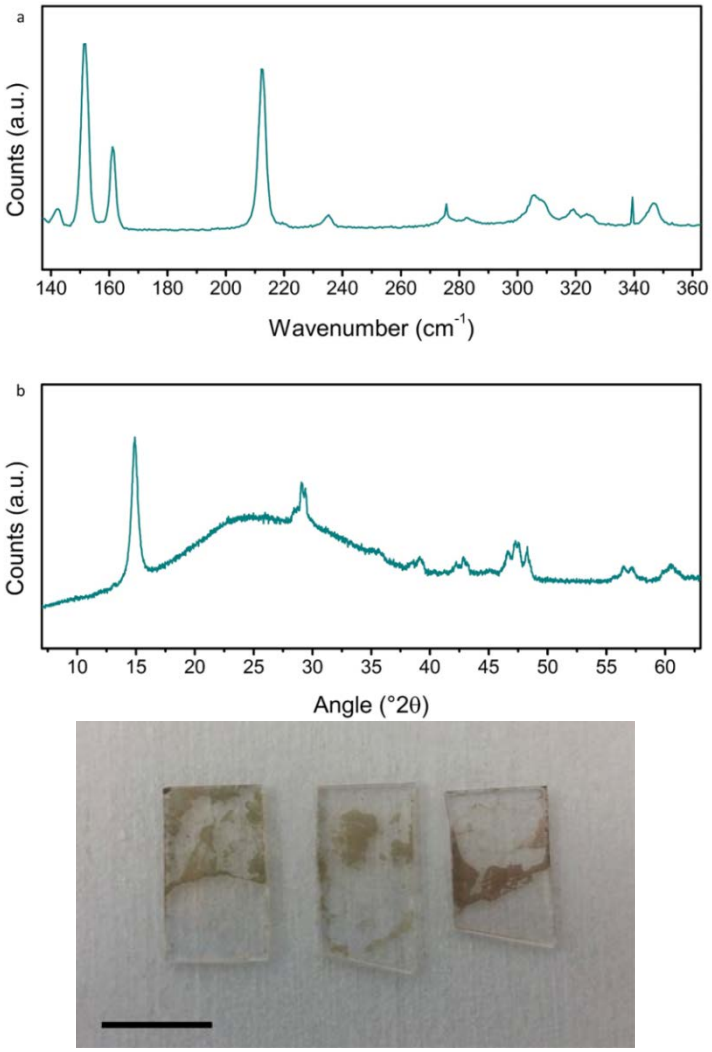

Figure 4.7 a) Raman spectrum of exfoliated ReS_2. b) XRD pattern of exfoliated ReS_2 and photo of free-formed films of MoS_2, WS_2 and ReS_2 on glass for XRD analysis, scale bar 1 cm.

A free-formed macroscopic film of each material was collected on a glass substrate, as displayed in Figure 4.7. The XRD patterns collected from the films are presented in Figure 4.6c. MoS_2 and WS_2 have prominent (002) peaks at 14.7 and 14.6°2θ respectively.[19, 20] ReS_2 has (001) peak at 14.9°2θ, as displayed in Figure 4.7b.[17] In each case, a prominent peak is observed for the basal plane of the two-dimensional material, indicating that the particle arrangement in the flat orientation is preferential for all materials.

4.3.2 Controlled film deposition

When solid substrates are dipped into the liquid-liquid interface, the assembled particles form a film as shown in Figure 4.7. However, more controlled film deposition is crucial for achieving useful uniform films. Here we make use of hydrophobic substrate patterning, as has been demonstrated in a similar approach for patterned graphene film deposition.[21]

The patterning process, as demonstrated in Figure 4.2, makes use of photolithography for controlled patterned photoresist, followed by hydrophobic treatment using PFDTES (as detailed in the Experimental section 4.2.4). Once the photoresist has been lifted-off, the hydrophobic patterned substrate is achieved. A photo of an example of a hydrophobic patterned substrate is displayed in Figure 4.8, showing the wet substrate with droplets of water confined to the non-treated areas.

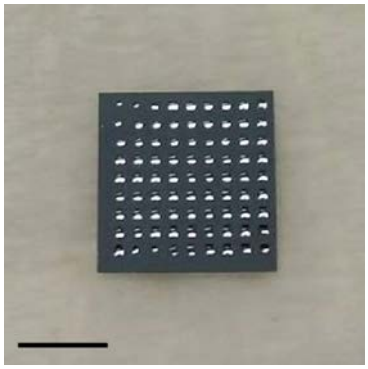

Figure 4.8 Photo of an example of a hydrophobic patterned substrate wet with water, scale bar 5 mm.

These treated substrates were dipped into the assembled film, inside a plastic tube, to achieve patterned films (Figure 4.2). The nanoflakes deposited in the non-treated areas and established densely-packed films, with well-defined edges observed at the hydrophobic boundaries (Figure 4.2 and 4.9).

The patterned films were characterised to determine the uniformity of the developed films. Optical imaging (Figure 4.9a and e) shows that large-scale films have been achieved, showing distinct horizontal edges that correspond to the hydrophobic constraints. It is observed by SEM (Figure 4.9b and f), that the films are made up from a densely-packed assembly of small nanoflakes. At this stage, it appears as though the film quality is limited by the quality of the nanoflake suspension, however

optimisation of the exfoliation process is outside the scope of this work. If large, ultrathin sheets were used, the film should be thin and have less overlapping grain edges.

AFM analysis of the thin films (Figure 4.9c and g) shows the arrangement of individual nanoflakes in the films. The step-edges are close to 20 nm high for MoS_2 and 10 nm high for WS_2 (Figure 4.9d). Both samples have a large 0 nm thickness peak, corresponding to the substrate, and WS_2 shows a narrower height distribution than MoS_2, indicating that the WS_2 film is more uniform in thickness (Figure 4.9h). As mentioned previously, optimisation of the exfoliation process for ultrathin nanoflakes should result in more uniform films being achieved.

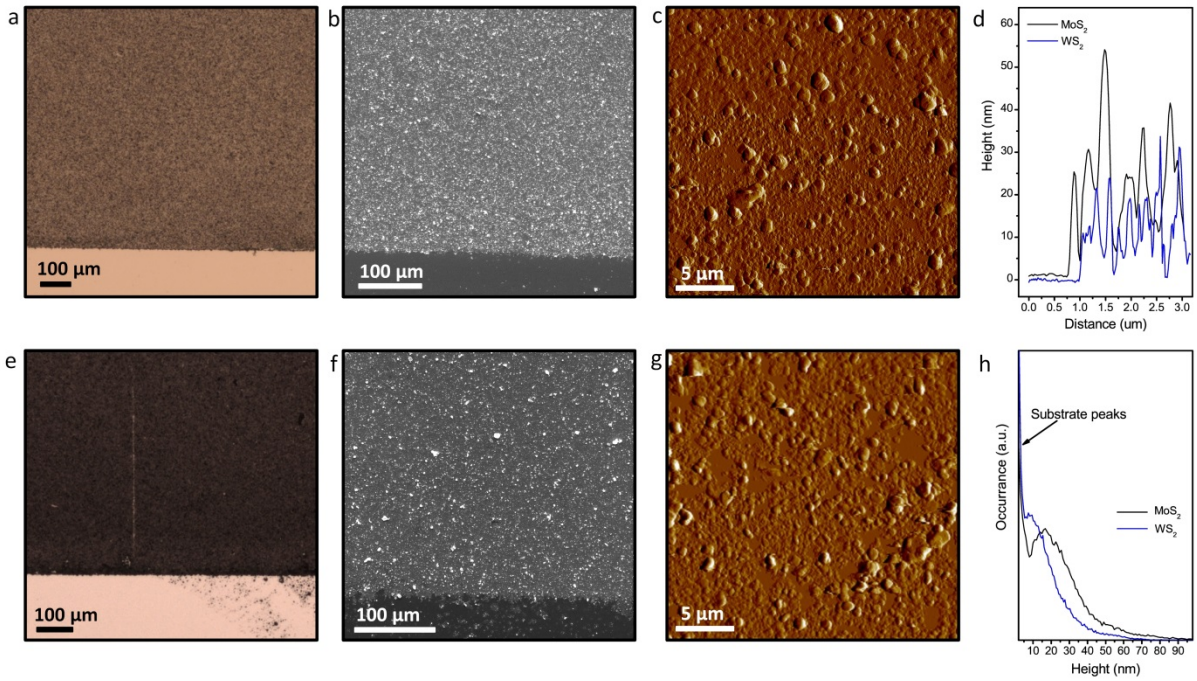

Figure 4.9 Deposited film characterisation of a-c) MoS_2 and e-g) WS_2. a and e), optical images showing a horizontal hydrophobic edge. b and f), SEM images. c and g), AFM images. d, height profiles of the film edge and h) height distribution over a 50 μm^2 area of the film for MoS_2 (black) and WS_2 (blue).

Patterned ReS_2 films are also presented in Figure 4.10, however a large scale film was not established due to particle agglomeration, as discussed previously. In Figure 4.11, MoS_2 and ReS_2 film deposition is directly compared by using substrates with the same pattern. MoS_2 is shown to spread into a thin film that evenly fills a large area, whilst ReS_2 is observed to group together into a thicker, less uniform film, which does not fill the pattern to the hydrophobic boundaries.

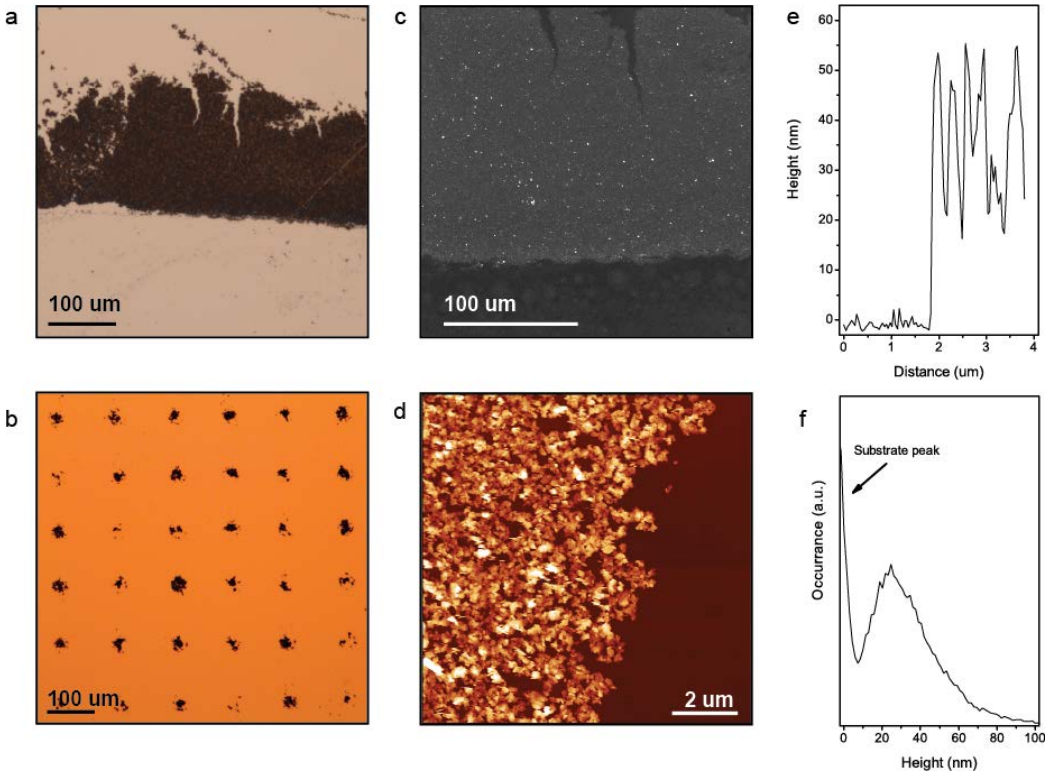

Figure 4.10 ReS_2 patterned films that don't follow the hydrophobic patterning well. a) optical image of horizontal patterned film, b) optical of spot patterned film, c) SEM image of same area as a), d) AFM image, e) AFM profile and f) AFM height statistics. The thickness of the film is much higher and has a wider height distribution than for MoS_2 and WS_2 films because of particle agglomeration.

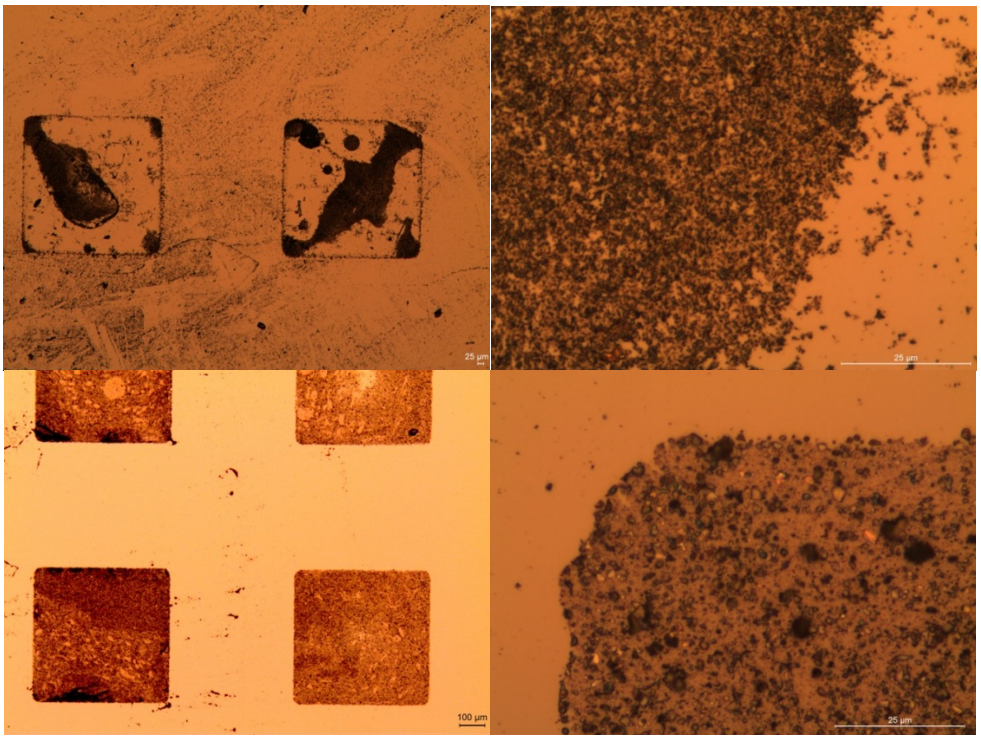

Figure 4.11 Example of the same patterned ReS_2 (top) and MoS_2 (bottom) film, showing MoS_2 forms a much larger, more uniform film.

Examples of other patterns, such as stripes and spots, are also presented (Figures 4.2 and 4.12). These images highlight the possibility of long range patterning, with films being confined within the patterned domains. The size of the domains also impacts the quality of the deposited film. When the deposition is confined to very small areas, the particles are deposited in a more random way. This is believed to reflect the behaviour of the solvent during the dipping and drying steps. In large areas, the particles are deposited and the solvent is more mobile on the substrate as it is lifted from the liquid-liquid interface. With very small patterns, the solvent becomes trapped in the confined regions and subsequent drying results in particles being deposited in a dried drop type residue. There are also discrepancies between film quality on different substrates and in regions of the same substrate (Figure 4.12), which highlights the importance of the substrates' surface properties. Robotic dip techniques might also help to control dip angle and velocity to maintain a uniform deposition.[22]

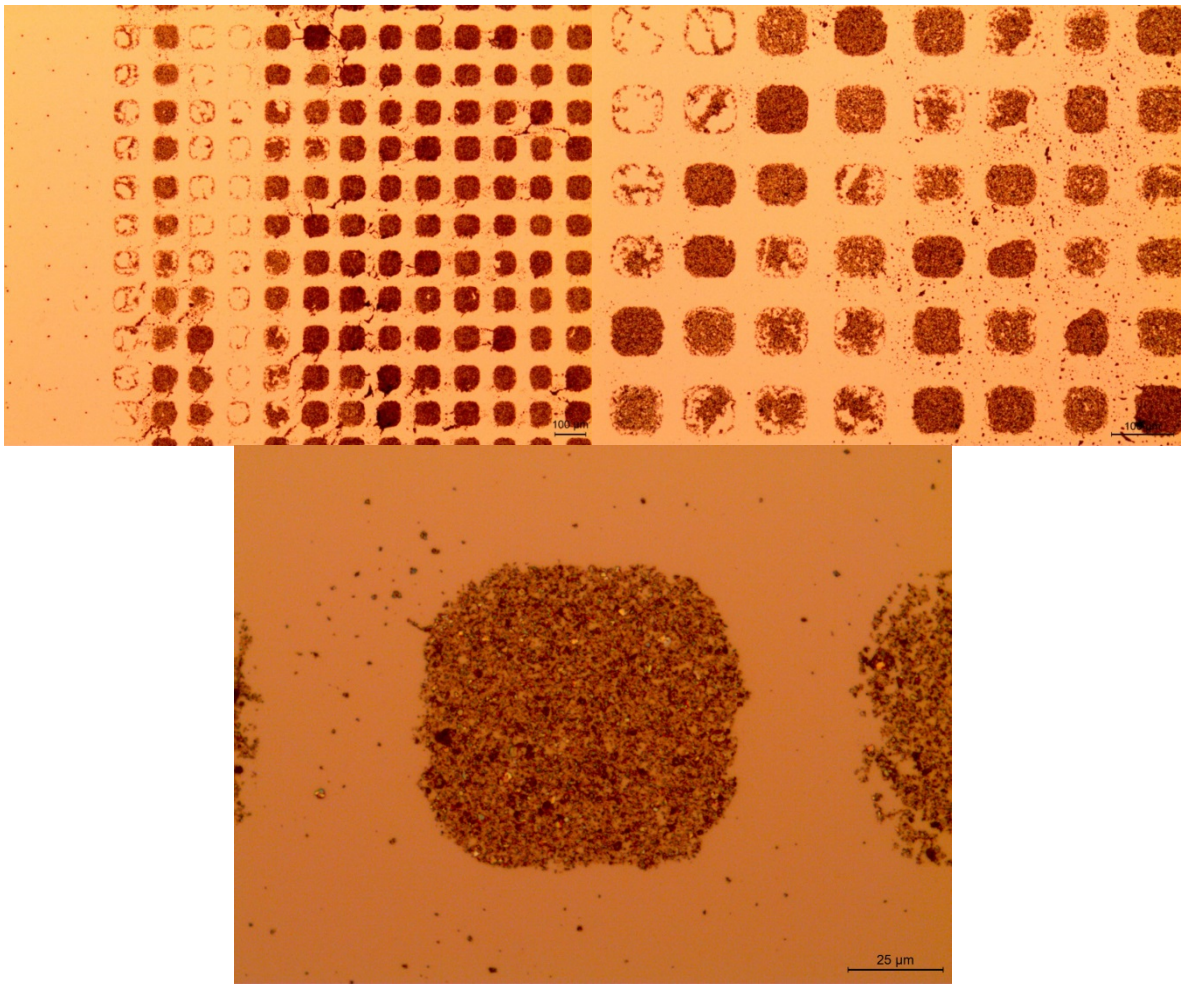

Figure 4.12 Patterned WS_2 film showing difficulty in long range deposition consistency. Dip-coating by hand could be improved by introduction of a robotic process.

4.3.3 Composite film formation

Composite films were established, by mixing two different nanoflake suspensions together, before film assembly and extraction. The Raman spectra (Figure 4.13a) collected from the composite films display vibrational peaks corresponding to each component of the films, as discussed previously. This shows that there is not one species preferentially attracted to the liquid-liquid interface, both species are present in the assembled films. The presence of both materials in the composite films was confirmed using XPS analysis, as shown in Figure 4.14.

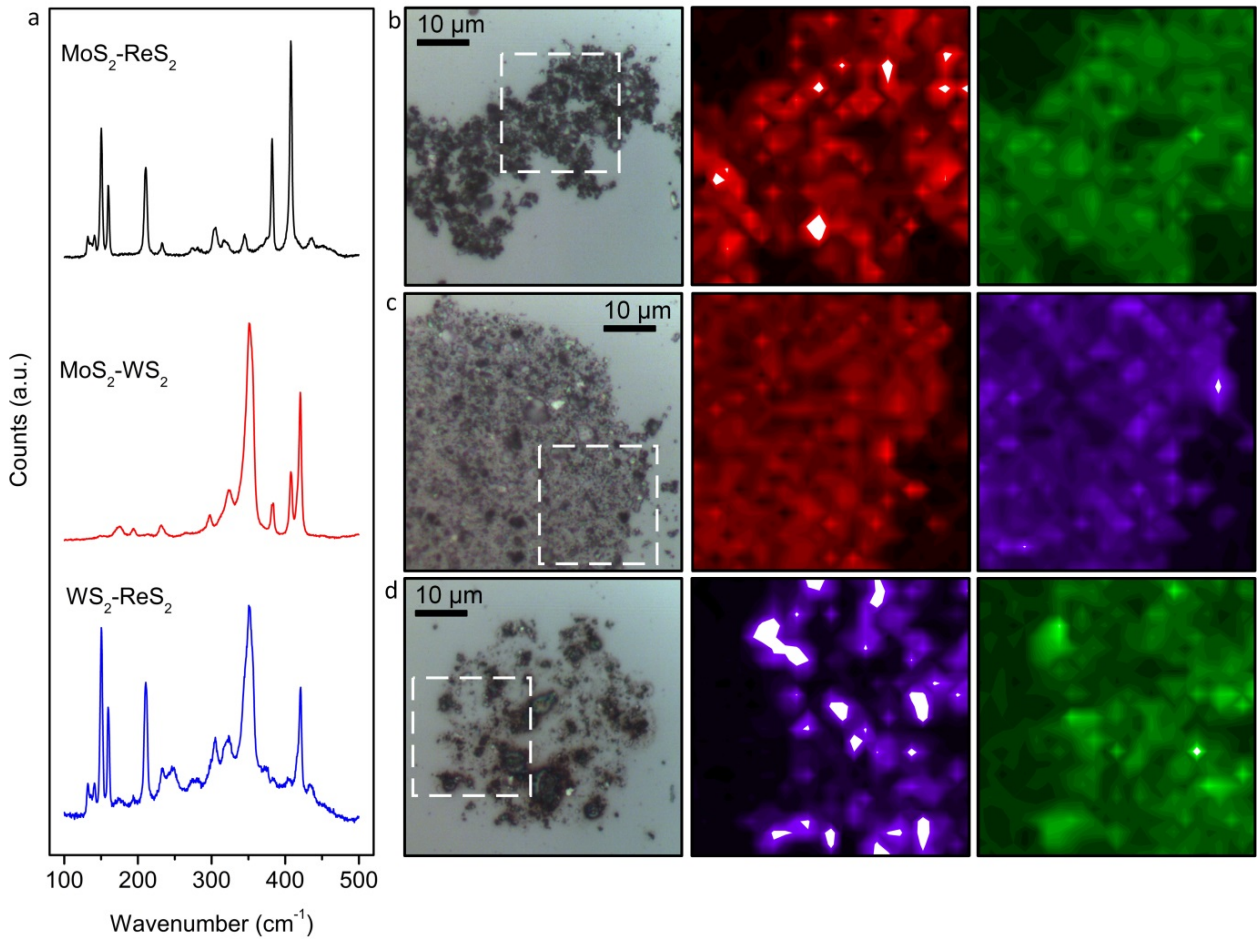

Figure 4.13 Raman spectra and maps of composite films. a) Raman spectrum of each composite. Optical image and Raman maps of material distribution in the outlined square for b) MoS_2-ReS_2, c) MoS_2-WS_2 and d) WS_2-ReS_2. Maps show MoS_2 in red, ReS_2 in green and WS_2 in purple.

Maps of the intensity of the major peak for each species (151, 351, 407 cm^{-1} for ReS_2, WS_2 and MoS_2, respectively) displayed in Figure 4.13 b-d, show that the distribution of each component within the film is uniform. There are no patches in the films, consisting of only one species, indicating that even

distribution of both materials is achieved. The films that contain ReS_2 have lower coverage and do not follow the patterning as accurately as the films which only contain MoS_2 and WS_2. It is believed that the presence of ReS_2 results in particle agglomeration, even in the composite structures. As such, the mixture of MoS_2-WS_2 (Figure 4.13c) achieves the most uniform composite thin film.

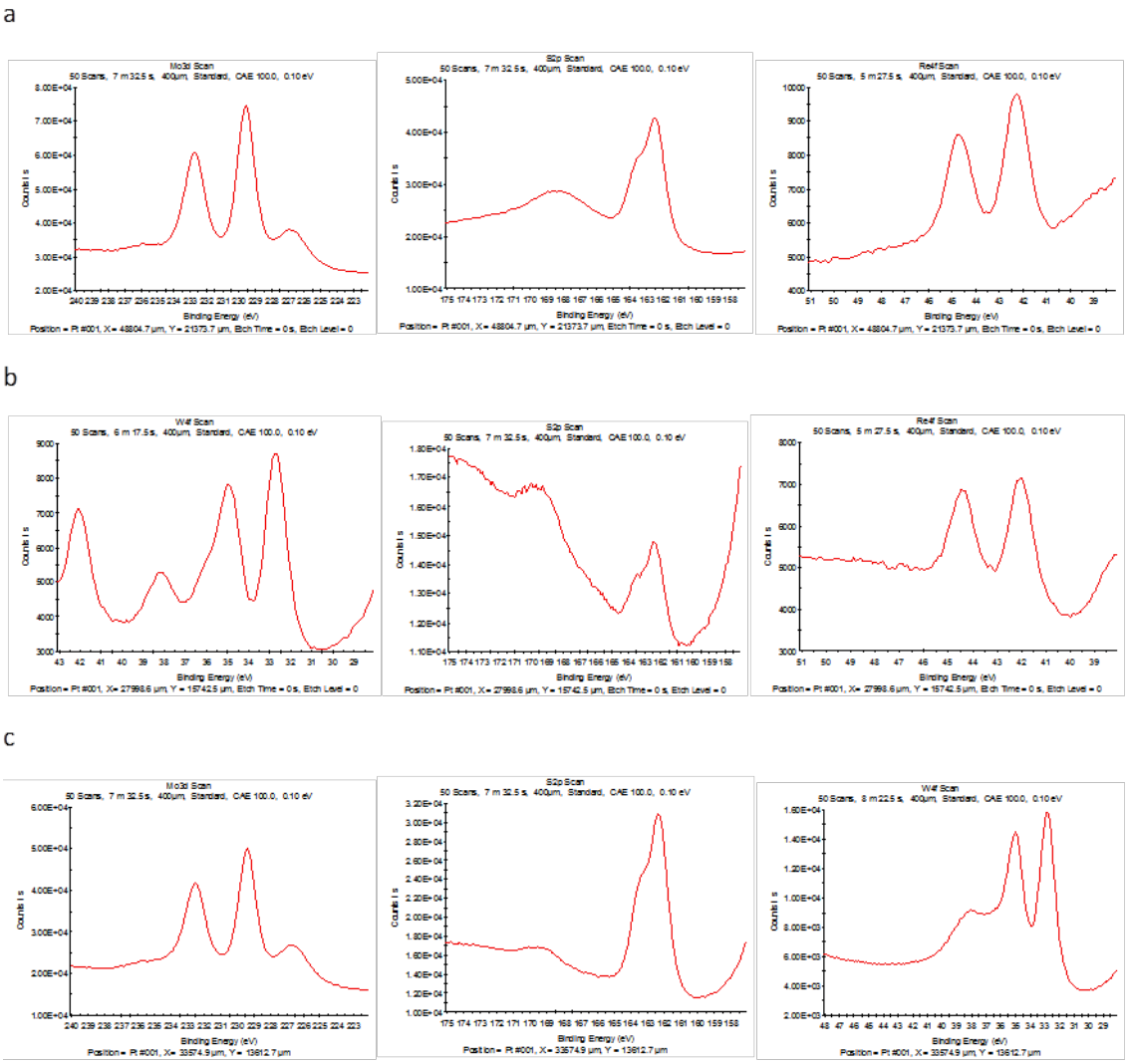

Figure 4.14 XPS of composite films. a) MoS_2-ReS_2, b) WS_2-ReS_2 and c) MoS_2-WS_2.

This new film deposition method allows for large scale controlled patterning of TMD nanoflakes into thin films. Incorporation of two different TMDs into a composite film provides the opportunity to explore heterostructures.

4.4 Conclusions

A new method to assemble films made up of 2D TMDs at a liquid-liquid interface has been achieved, through direct treatment of the exfoliated nanoflake suspensions. 2D MoS_2 and WS_2 were shown to form large scale (in the order of mm^2) thin films through dip coating of substrates into the assembled film. To maintain the properties of the nanoflakes, surfactants and chemical modifiers were not used during the exfoliation and film assembly processes. In this way, a facile and repeatable method was achieved to establish assembled 2D TMD films. Agglomeration was shown to be detrimental to ReS_2 thin film formation, however this could potentially be rectified through chemical modification. Although not studied here, further optimisation of the exfoliation conditions is expected to give rise to large ultrathin nanoflakes that could possibly easily assemble into films. In this way, 2D TMD nanoflake films of reduced thickness with fewer grain boundaries could be demonstrated. The implementation of a hydrophobic substrate patterning process, through photolithography, achieves desirable control over the confinement of film deposition. Large area uniform patterned films of densely-packed TMD nanoflakes have been achieved using a fast and simple process. The developed method for film assembly and deposition is a critical step towards the development of uniform thin films for use in catalysis, sensing and energy storage applications.

In the following chapter, the exfoliation of quasi-stratified crystals, to form new two-dimensional materials, will be explored. Ultrathin micron-scale two-dimensional sheets are produced through a reductive exfoliation method.

4.5 References

1. Yu, X.; Prevot, M. S.; Guijarro, N.; Sivula, K. Self-assembled 2D WSe_2 thin films for photoelectrochemical hydrogen production. *Nat. Commun.* **2015,** 6, 8596.

2. Fan, X.; Xu, P.; Zhou, D.; Sun, Y.; Li, Y. C.; Nguyen, M. A. T.; Terrones, M.; Mallouk, T. E. Fast and Efficient Preparation of Exfoliated 2H MoS_2 Nanosheets by Sonication-Assisted Lithium Intercalation and Infrared Laser-Induced 1T to 2H Phase Reversion. *Nano Lett.* **2015,** 15, 5956-5960.

3. Yu, X.; Prévot, M. S.; Sivula, K. Multiflake Thin Film Electronic Devices of Solution Processed 2D MoS_2 Enabled by Sonopolymer Assisted Exfoliation and Surface Modification. *Chem. Mater.* **2014,** 26, 5892-5899.

4. Tan, C.; Liu, Z.; Huang, W.; Zhang, H. Non-volatile resistive memory devices based on solution-processed ultrathin two-dimensional nanomaterials. *Chem. Soc. Rev.* **2015,** 44, 2615-2628.

5. Chan, Y. Y.; Eng, A. Y. S.; Pumera, M.; Webster, R. D. Assessments of Surface Coverage after Nanomaterials are Drop Cast onto Electrodes for Electroanalytical Applications. *ChemElectroChem* **2015,** 2, 1003-1009.

6. Clark, R. M.; Berean, K. J.; Carey, B. J.; Pillai, N.; Daeneke, T.; Cole, I. S.; Latham, K.; Kalantar-zadeh, K. Patterned films from exfoliated two-dimensional transition metal dichalcogenides assembled at a liquid-liquid interface. *J. Mater. Chem. C* **2017,** 5, 6937-6944.

7. Carey, B. J.; Ou, J. Z.; Clark, R. M.; Berean, K. J.; Zavabeti, A.; Chesman, A. S. R.; Russo, S. P.; Lau, D. W. M.; Xu, Z.-Q.; Bao, Q.; Kevehei, O.; Gibson, B. C.; Dickey, M. D.; Kaner, R. B.; Daeneke, T.; Kalantar-Zadeh, K. Wafer-scale two-dimensional semiconductors from printed oxide skin of liquid metals. *Nat. Commun.* **2017,** 8, 14482.

8. Biswas, S.; Drzal, L. T. A Novel Approach to Create a Highly Ordered Monolayer Film of Graphene Nanosheets at the Liquid−Liquid Interface. *Nano Lett.* **2009,** 9, 167-172.

9. Niu, Z.; He, J.; Russell, T. P.; Wang, Q. Synthesis of Nano/Microstructures at Fluid Interfaces. *Angew. Chem., Int. Ed.* **2010,** 49, 10052-10066.

10. Hu, L.; Chen, M.; Fang, X.; Wu, L. Oil-water interfacial self-assembly: a novel strategy for nanofilm and nanodevice fabrication. *Chem. Soc. Rev.* **2012,** 41, 1350-1362.

11. Nikolaides, M. G.; Bausch, A. R.; Hsu, M. F.; Dinsmore, A. D.; Brenner, M. P.; Gay, C.; Weitz, D. A. Electric-field-induced capillary attraction between like-charged particles at liquid interfaces. *Nature* **2002,** 420, 299-301.

12. Booth, S. G.; Dryfe, R. A. W. Assembly of Nanoscale Objects at the Liquid/Liquid Interface. *J. Phys. Chem. C* **2015,** 119, 23295-23309.

13. Kim, F.; Cote, L. J.; Huang, J. Graphene Oxide: Surface Activity and Two-Dimensional Assembly. *Adv. Mater.* **2010,** 22, 1954-1958.

14. Li, H.; Zhang, Q.; Yap, C. C. R.; Tay, B. K.; Edwin, T. H. T.; Olivier, A.; Baillargeat, D. From Bulk to Monolayer MoS_2: Evolution of Raman Scattering. *Adv. Funct. Mater.* **2012,** 22, 1385-1390.

15. Lee, C.; Yan, H.; Brus, L. E.; Heinz, T. F.; Hone, J.; Ryu, S. Anomalous Lattice Vibrations of Single- and Few-Layer MoS_2. *ACS Nano* **2010,** 4, 2695-2700.

16. Berkdemir, A.; Gutiérrez, H. R.; Botello-Méndez, A. R.; Perea-López, N.; Elías, A. L.; Chia, C.-I.; Wang, B.; Crespi, V. H.; López-Urías, F.; Charlier, J.-C.; Terrones, H.; Terrones, M. Identification of individual and few layers of WS_2 using Raman Spectroscopy. *Sci. Rep.* **2013,** 3, 1755.

17. Fujita, T.; Ito, Y.; Tan, Y.; Yamaguchi, H.; Hojo, D.; Hirata, A.; Voiry, D.; Chhowalla, M.; Chen, M. Chemically exfoliated ReS_2 nanosheets. *Nanoscale* **2014,** 6, 12458-12462.

18. Tongay, S.; Sahin, H.; Ko, C.; Luce, A.; Fan, W.; Liu, K.; Zhou, J.; Huang, Y.-S.; Ho, C.-H.; Yan, J.; Ogletree, D. F.; Aloni, S.; Ji, J.; Li, S.; Li, J.; Peeters, F. M.; Wu, J. Monolayer behaviour in bulk ReS_2 due to electronic and vibrational decoupling. *Nat. Commun.* **2014,** 5, 3252.

19. Stengl, V.; Henych, J. Strongly luminescent monolayered MoS_2 prepared by effective ultrasound exfoliation. *Nanoscale* **2013,** 5, 3387-3394.

20. Carey, B. J.; Daeneke, T.; Nguyen, E. P.; Wang, Y.; Zhen Ou, J.; Zhuiykov, S.; Kalantar-zadeh, K. Two solvent grinding sonication method for the synthesis of two-dimensional tungsten disulphide flakes. *Chem. Commun.* **2015,** 51, 3770-3773.

21. Wang, Z.; Yang, X. S.; Chen, M. Y. Assembly of Patterned Graphene Film Aided by Wetting/Nonwetting Surface on Liquid Interface. *IEEE Trans. Nanotechnol.* **2014,** 13, 589-593.

22. Darhuber, A. A.; Troian, S. M.; Davis, J. M.; Miller, S. M.; Wagner, S. Selective dip-coating of chemically micropatterned surfaces. *J. Appl. Phys.* **2000,** 88, 5119-5126.

Chapter 5

Exfoliation of quasi-stratified Bi_2S_3 crystals into micron-scale ultrathin corrugated nanosheets

5.1 Introduction

There are ongoing challenges with the optimisation of the exfoliation of layered sulphide crystals, with issues regarding yield and dimensions. In an attempt to synthesise larger ultrathin nanosheets, at a high yield, *via* exfoliation, my colleagues and I developed a reductive exfoliation process which was published in Nanoscale journal, 2016.[1]

Sonication is well-known to lead to nanosheet cracking and breakdown, a compromise between reducing sheet thickness and maintaining lateral size has to be made.[2, 3] Hence, most liquid phase protocols lead to highly polydispersed products featuring poorly defined electronic properties, since the electronic structure of MoS_2 is highly dependent on the number of layers and lateral size.[4, 5]

Furthermore, high power mechanical exfoliation techniques have been found to result in unwanted organic residues due to sonochemical degradation of solvents or surfactants used in the process.[3] While lithium intercalation procedures generally lead to larger sheet sizes, these methods result in the exfoliation of semi-metallic 1T MoS_2 layers which are not desirable for applications requiring a bandgap.[6] Thus scalable approaches that result in the dispersion of large area MoS_2 nanosheets with a narrow thickness profile, an optical bandgap and reproducible flake quality are highly sought after.

The process which has been developed by my colleagues and I to tackle the above mentioned issues is based on reductive MoS_2 exfoliation. The method utilises hydrazine salts without the need of any sonication steps, reducing the probability of sheet breakdown. Zheng *et al.* recently proposed a hydrothermal hydrazine pre-exfoliation method for the production of large area MoS_2 nanosheets.[7] Their proposed reaction proceeds in an autoclave at elevated pressures and temperatures, leading to the intercalation of hydrazine molecules into the MoS_2 host lattice. However, in their work a further intercalation step using alkali naphthalenides was found to be necessary to obtain thin layer MoS_2 nanosheets. Rather than adopting a similar multi-step exfoliation approach, and after observing that concentrated hydrazine hydrate solutions are corrosive to MoS_2 sheets at our laboratory, we instead explored the exfoliation efficacy of less alkaline hydrazine salts at relatively low concentrations. In this work, we show that thin layers of MoS_2 can be directly exfoliated from the bulk following a comparatively straightforward synthesis protocol that does not require mechanical agitation.

We developed a fast exfoliation route utilising hydrazine dihydrochloride, leading to MoS_x nanosheets with a highly monodispersed thickness profile. The lateral dimensions were limited by the size of the initial bulk crystals, and larger sheet sizes may be feasible in the future. Figure 5.1b shows a typical transmission electron microscopy (TEM) image of the synthesised nanosheets. The exfoliated MoS_x layers are of exceptionally large lateral dimension reaching several micrometres. The average lateral size determined using dynamic light scattering (DLS) and statistical analysis of TEM images (Figure 5.1a) reveals that the lateral dimensions of the exfoliated sheets correspond to roughly half of the precursor crystal size. Discrepancies between DLS data and TEM data likely arise due to differing

folding of the nanosheets. The determined sizes are low estimates and the true size of flat flakes is expected to be larger.

The nanosheets appear translucent in the TEM images, indicating their thin nature. High resolution TEM (HRTEM) images revealed a lack of crystallinity of the nanosheets (Figure 5.1c). The flat lying areas of the nanosheets feature no discernible crystal pattern, indicating lattice distortion. Imaging of folds and wrinkles at atomic resolution (Figure 5.1d) revealed increased crystallinity in these strained regions, with the spacing matching the electron diffraction patterns shown in Figure 5.1e.

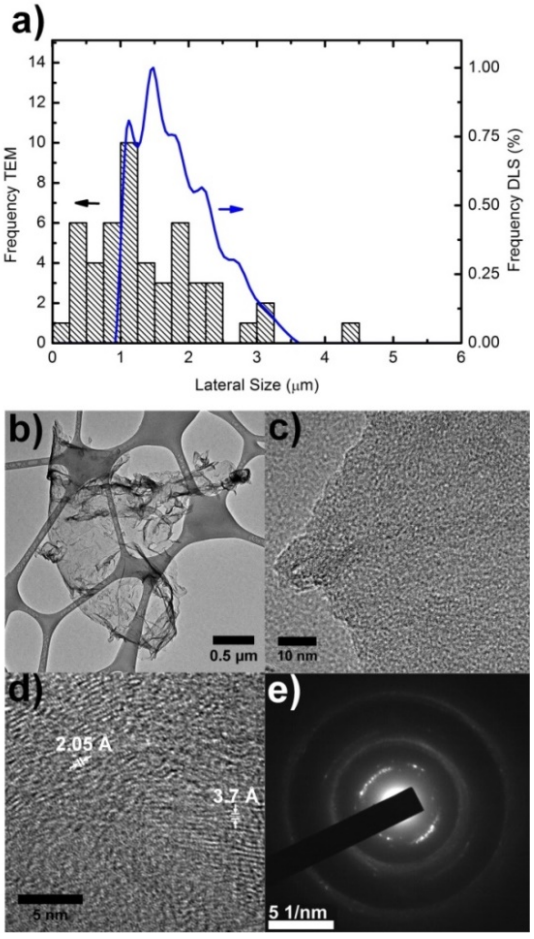

Figure 5.1 a) TEM and DLS size distributions. b) low resolution TEM image of a typical exfoliated MoS_x sheet. c) HRTEM image of a flat area. d) HRTEM image of a folded ridge; the white arrows show the atom to atom spacing with distances of 2.05 Å and 3.7 Å. e) SAED pattern of entire flake.

Atomic force microscopy (AFM) analysis revealed that the exfoliated sheets are ~1.9±0.2 nm thick (Figure 5.2). Interestingly the thickness of the product is highly monodispersed. The thickness corresponds to two fundamental layers of MoS_x, since a single layer of MoS_2 has been reported to be

0.7 to 0.9 nm thick, depending on the crystal polytype. Despite measuring the thickness of hundreds of nanosheets, all encountered flakes are found to be bilayers. This extraordinary monodispersity is setting the hydrazine based exfoliation method apart from other synthetic routes.

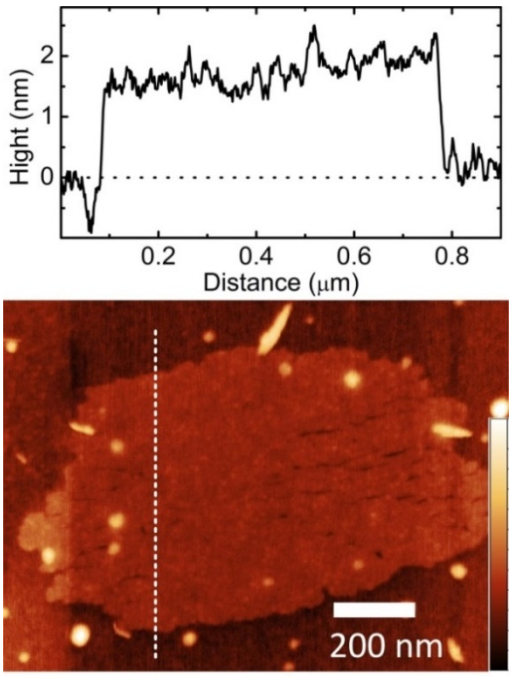

Figure 5.2 AFM profile and image of a typical MoS_x nanosheet exfoliated with hydrazine dihydrochloride. The dotted line indicates the area investigated for the height profile.

This novel synthesis method allows producing highly monodispersed substoichiometric MoS_x bilayers with highly defined physical dimensions in a fast liquid phase process. The reaction mechanism was found to be based on the reduction of the MoS_2 bulk crystal with hydrazine salts, leading to lattice deformations and sulphur loss, ultimately resulting in delamination and exfoliation.

The developed method has been demonstrated to lead to the production of MoS_x nanosheets with superior monodispersed thickness profile and exceptionally large lateral dimensions due to the elimination of the need for applying high power mechanical agitation. The synthetic route is likely suitable for the exfoliation of other layered transition metal chalcogenides and further strong organic reducing agents may be suitable to facilitate the reaction. Thus future work should establish a better understanding of the process and attempt to investigate a wider range of reagents to determine the versatility of this method.

Following successful exfoliation of layered MoS_2 crystals, the same method was investigated as a gentle alternative for exfoliation of quasi-stratified crystals such as bismuth sulphide (Bi_2S_3).

The crystal structure of Bi_2S_3 is orthorhombic, with a layered structure of atomic scale ribbons held together by van der Waals forces. This structure favours the formation of one-dimensional nanomaterials, however one report of wider, quasi two-dimensional, ribbons has been presented.[8] The existence of Bi_2S_3 in nanoribbon morphology is an indication that this material can possibly be exfoliated from its highly ordered bulk crystals into larger, planar nanosheets.

In this chapter, I demonstrate the exfoliation of highly ordered Bi_2S_3 crystals, using a hydrazine salt, to obtain large sheets of two-dimensional (2D) bismuth sulphide. The chemical exfoliation process eliminates the need for sonication of the reaction mixture and results in large sheets, despite the fact that native Bi_2S_3 is comprised of in-plane van der Waals ribbons. The sheets are fully characterised to reveal their stoichiometry and morphological properties. Subsequently, devices based on the exfoliated nanosheets are established to investigate their electrical and sensing properties.

The contents of this chapter have been published as an article in Chemistry of Materials journal.[9]

5.2 Experimental details

5.2.1 Materials

Bulk Bi_2S_3 powder (99.9%) was purchased from Strem. Hydrazine dihydrochloride (98.5%) and dimethyl formamide (DMF) (99.8%) were purchased from Sigma Aldrich.

5.2.2 Reductive exfoliation

The method used for the exfoliation of stratified Bi_2S_3 was similar to that recently developed by our group for exfoliating MoS_2.[1] 0.5 g of hydrazine dihydrochloride and 0.1 g of bismuth sulphide were mixed into 10 mL of DMF and heated to reflux at 153°C for 1 hour, with constant stirring. The mixture was then stored at −30°C for approximately 90 minutes, to solidify remaining organic side products. The solution was centrifuged at 200 RCF for 15 minutes to remove unreacted bulk Bi_2S_3.

The produced suspension was then centrifuged at 16,000 RCF for 60 minutes to sediment out the ultrathin bismuth sulphide. The ultrathin sheets were re-suspended and washed several times using fresh DMF. We avoided washing with water since the addition of water leads to the crystallisation of large amounts of bismuth oxychloride (BiOCl) which forms from excess dissolved bismuth and chloride ions (See Figure 5.3).

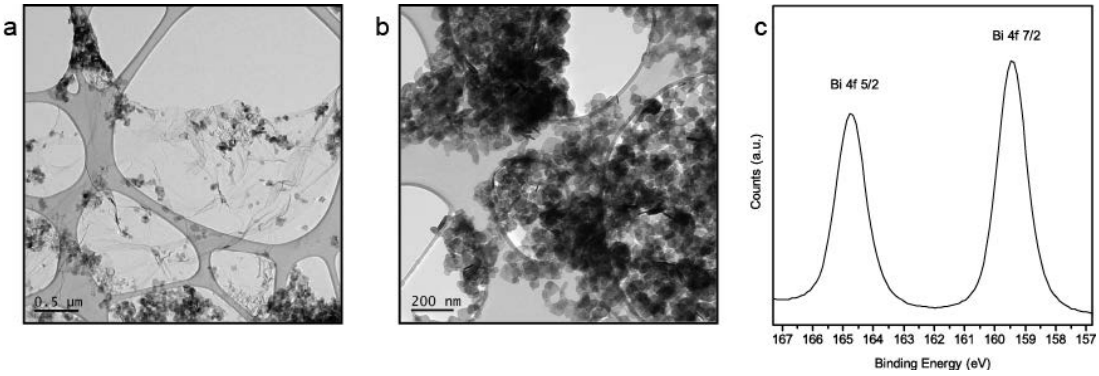

Figure 5.3 BiOCl characterisation a) Bi_2S_3 nanosheet covered in BiOCl crystals. b) Isolated BiOCl crystals. c) XPS trace of Bi 4f region, with peaks corresponding to BiOCl and no peaks for Bi_2S_3.

5.2.3 Device fabrication

The suspended nanosheets were drop casted onto highly p-doped 290 nm SiO_2/Si substrates pre-patterned with a registration scheme of Au markers. Optical and scanning electron microscopy (SEM) images were subsequently used to locate suitable sheets. Electrodes were patterned using electron beam lithography (EBL) at 25 keV (FEI XL40 SEM) using the substrate markers for the alignment, followed by deposition of 10 nm Ti and 50 nm Au using electron beam evaporation.

5.2.4 Characterisation

The suspension of ultrathin sheets in DMF was dried on silicon substrates, glass slides and transmission electron microscopy (TEM) grids for further analysis. TEM was performed on a JEOL 1010 instrument (100 keV), to determine the lateral dimensions of the sheets. High resolution TEM (HRTEM) images were collected using a JEOL 2100F instrument (200 keV). SEM was conducted using an FEI Verios instrument operating with a landing energy of 1 kV (stage bias 4 kV). Optical images were collected with a Leica DM2500M microscope with a CCD camera. Sheet thickness was determined using a Bruker Dimension Icon atomic force microscope (AFM) in tapping mode.

A map of photoluminescence (PL) spectra was obtained using a Horiba Scientific LabRAM HR evolution system with 5 s exposure using excitation wavelength of 532 nm. A Reinshaw inVia spectrometer with laser excitation of 785 nm was employed to collect the Raman spectrum of the material. The powder x-ray diffraction (XRD) pattern of the sheets was collected using a Bruker D4 Endeavour with Cu Kα radiation of 1.5406 Å.

The elemental composition was studied by x-ray photoelectron spectroscopy (XPS) using a Thermo Scientific K-alpha instrument with a monochromated Al Kα x-ray source (1486.7 eV). The bulk material was also studied using an Oxford Instruments X-Max 80 energy dispersive x-ray spectroscopy (EDX) detector connected to the SEM.

Electrical measurements were performed using a Keithley 2400 sourcemeter. Standard 2-probe DC techniques were used, at ambient temperature and pressure, with a back gate voltage applied to the highly p-doped Si substrate. Elevated temperature measurements were achieved using a Linkam stage, with a temperature controlled stub.

Photoelectron spectroscopy in air (PESA) was used for determining the valence band position of samples dried on glass substrates, using a Riken Kekei AC-2.

Gas sensing was achieved using a custom sensing chamber attached to a digital mass flow controller, which was set at a flow rate of 200 sccm. The NO_2 concentration was 10 ppm in background air. H_2S and H_2 were set to 56 ppm in N_2 and 1% in air, respectively. Water vapour was introduced at 50% relative humidity.

5.3 Results and discussion

5.3.1 Structure and morphology

Liquid phase exfoliation of bulk Bi_2S_3 was carried out, as presented in the Experimental section, and the remaining bulk powder was removed. In brief, we used hydrazine dihydrochloride facilitated exfoliation, which does not require any mechanical agitation and leads to nanosheets of large lateral dimensions. After centrifugation, large amounts of grey sediment were observed, which indicates that

there is a high yield of ultrathin material produced. These were washed and re-suspended in DMF for further analysis.

The suspended nanosheets were studied by several techniques, to determine their size and morphology. 30 different sheets on a grid were measured by TEM, as presented in the size histogram (Figure 5.4a). A range of micron-scale dimensions are observed, with the majority of sheets being 2-4 µm in length, and some reaching dimensions as large as 20 µm. The highly wrinkled nature of the sheets when dried upon the TEM grid suggests that the true dimensions, when laid flat, would be even larger. It seems that the lateral dimension is limited by the dimensions of the starting bulk powder.

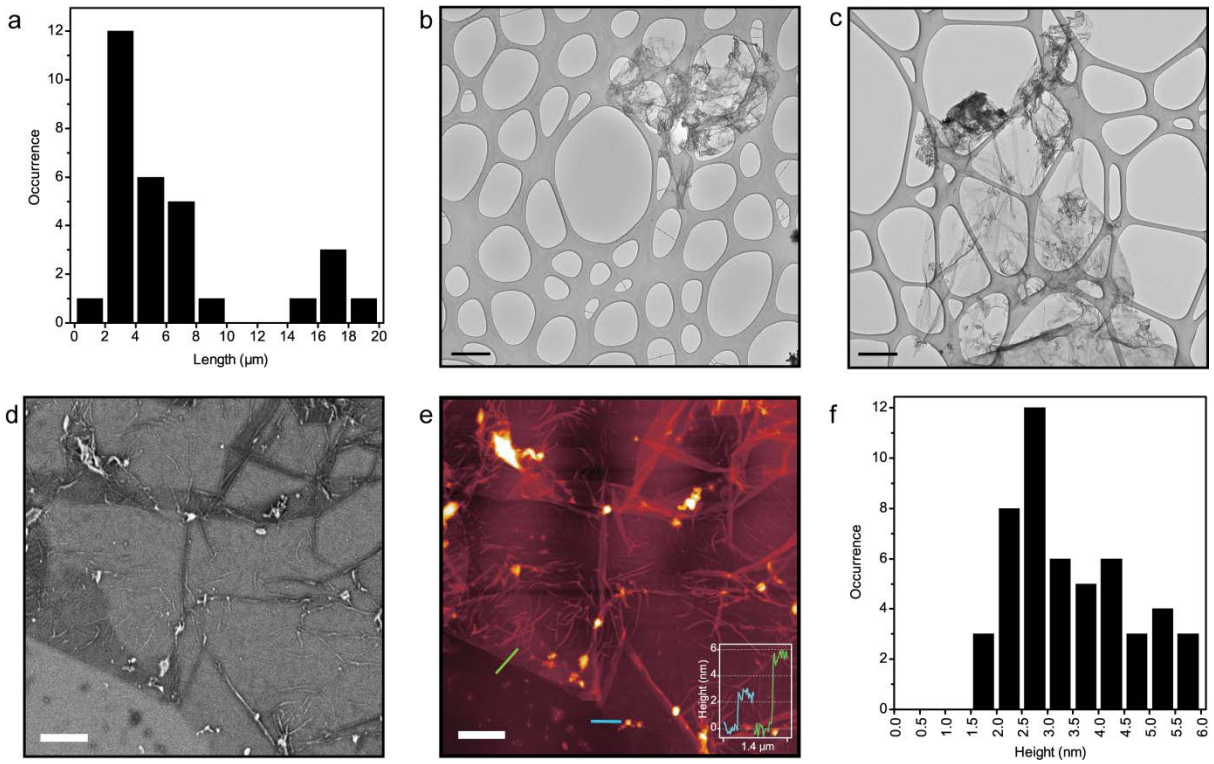

Figure 5.4 a) Size histogram of 30 sheets observed by TEM. b) TEM image of a small sheet, scale bar 0.5 µm. c) TEM image of a large sheet, scale bar 0.5 µm. d) SEM image of the edge of a sheet, scale bar 1 µm. e) AFM image of the same area shown in d), scale bar 1 µm. Inset height profiles of the blue and green lines. f) Thickness histogram prepared by measuring 50 flat and folded edges.

Example TEM images of a small and large sheet are presented in Figure 5.4b and c, additional TEM images with different degrees of wrinkling are presented in Figure 5.5. Transparent regions, where the sheets lay flat, indicate that the product is expected to be ultrathin. Additionally, the flexibility of the sheets is always associated with the low number of fundamental layers forming an ultrathin sheet.[10, 11]

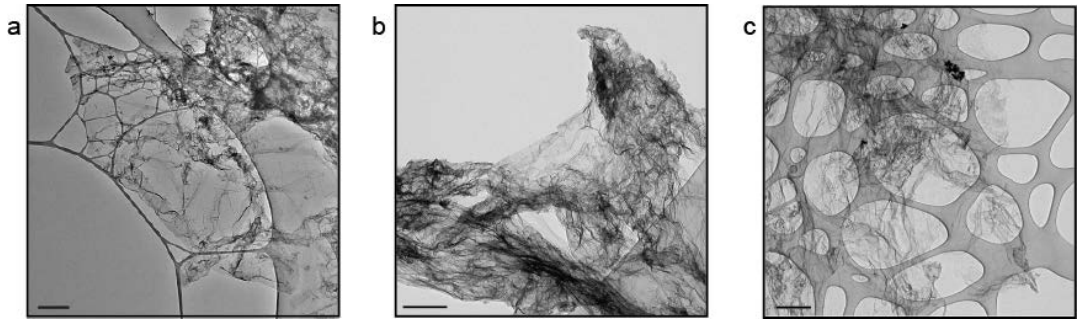

Figure 5.5 TEM images of different sheets, with different degrees of wrinkling. Scale bars all 0.5 µm.

SEM imaging was used for studying the structure of the sheets further, using settings to enhance the surface detail, enabling the observation of wrinkles and thin edges. Differences in the contrast of the SEM images show where the edge of the sheet lays flat or is folded over (See Figure 5.4d). It is also observed that some thick species have dried onto the sheet. These could be small pieces of unexfoliated material or other insoluble impurities and side products. Further optimisation of the washing process is necessary to obtain perfectly clean, uniform samples.

The thickness of the sheets was measured by AFM (Figure 5.4e and f) which show that a step at the flat edge of a sheet is 2.5 nm. The thickness of a full stoichiometric monolayer would be limited by the lattice parameter of 1.1 nm.[8] We were not able to find any step of this thickness in our samples as can be seen in Figure 5.4f. The minimum observed thickness was found to be just above 1.5 nm in all our observations (Figure 5.4f). We will associate this increase of the thickness with the development of a corrugated plane structure that will be discussed in the context of HRTEM imaging later in this section. Many folded edges are also observed, as shown by the green trace in Figure 5.4e, featuring a bilayer thickness in the order of 5 nm. Additional AFM images are presented in Figure 5.6.

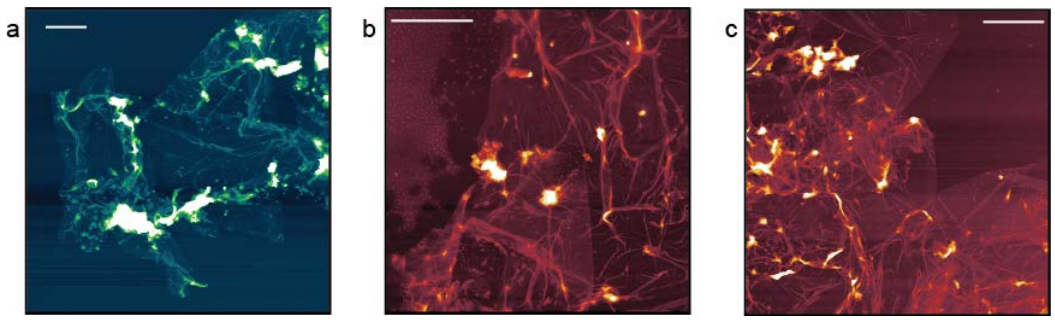

Figure 5.6 Typical AFM images, all scale bars are 2 µm.

As an example, a single sheet was analysed by a variety of techniques (SEM, AFM, optical images and photoluminescence), to determine the combined information that can be obtained for a single sheet (Figure 5.7). The observed folds and wrinkles in the material not only confirm the thinness of the sheets, but also show their strength and flexibility, since there are no signs of fracturing along the folds.

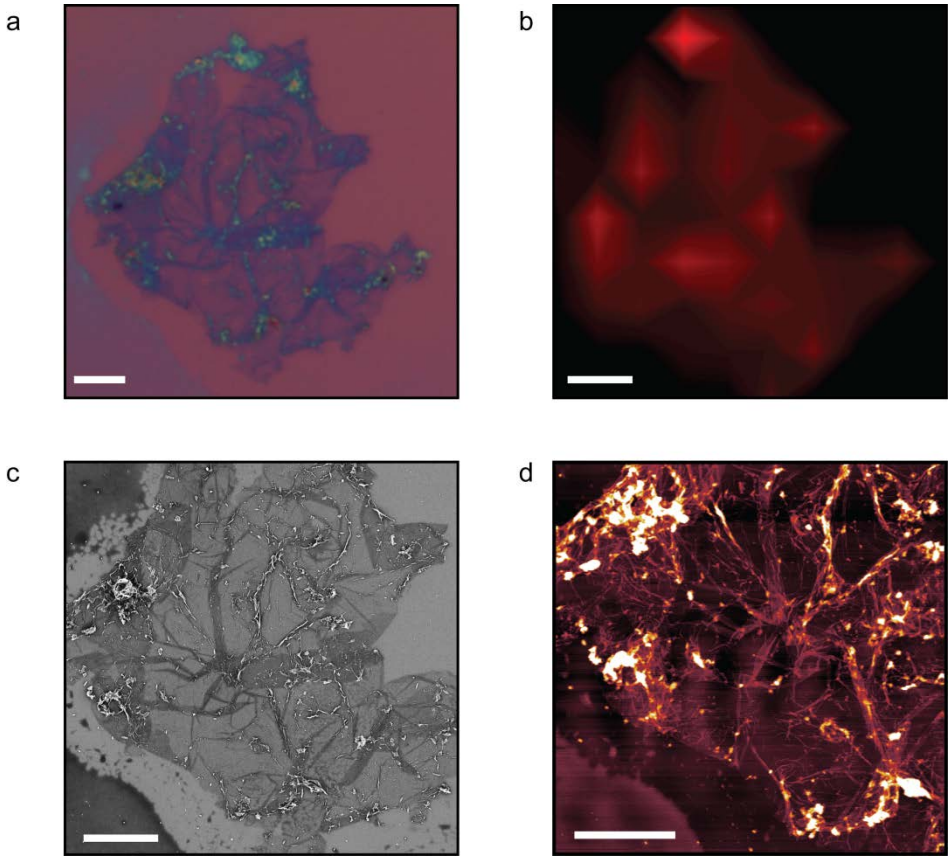

Figure 5.7 a) Optical image, b) PL map, c) SEM image and d) AFM of the same Bi_2S_3 sheet, scale bars are 5 µm. In all techniques used the thicker, folded regions of the sheets are easiest to identify. Imaging the flattest, ultrathin regions is quite challenging due to lack of contrast. As such, a combination of techniques must be used to fully identify the location and structure of the sheets, and optimisation of contrast is particularly important especially when the sheets are lying flat.

To further analyse the thickness of the exfoliated sheets, HRTEM was used, as presented in Figure 5.8. In the low magnification image, a single layer with several folds is observed (Figure 5.8a inset). Analysing folded edges of the nanosheets allows gaining insight into the local surface morphology of the nanosheets which can otherwise not be observed for flat laying regions. Higher magnification shows that the folded edges follow a zig-zag pattern (Figure 5.8a and b). This pattern is consistent

with the crystal structure of orthorhombic Bi_2S_3, with an offset herringbone arrangement of repeating units.[12] The height of the observed zig-zag, however, is close to ~1.3 nm (Figure 5.8b), indicating that the plane has been warped into deeper corrugations. Adding the depth of the observed corrugation to the lattice parameter of a single layer (1.1 nm) allows establishing an approximation for the expected layer thickness of the exfoliated sheets which is found to be ~2.4 nm for a corrugated monolayer. This number is consistent with the step height observed using AFM in Figure 5.4f, indicating that monolayer bismuth sulphide is synthesised. As can be seen in Figure 5.8a the crystal lattice has been highly distorted, although some areas of localised crystallinity can still be identified.

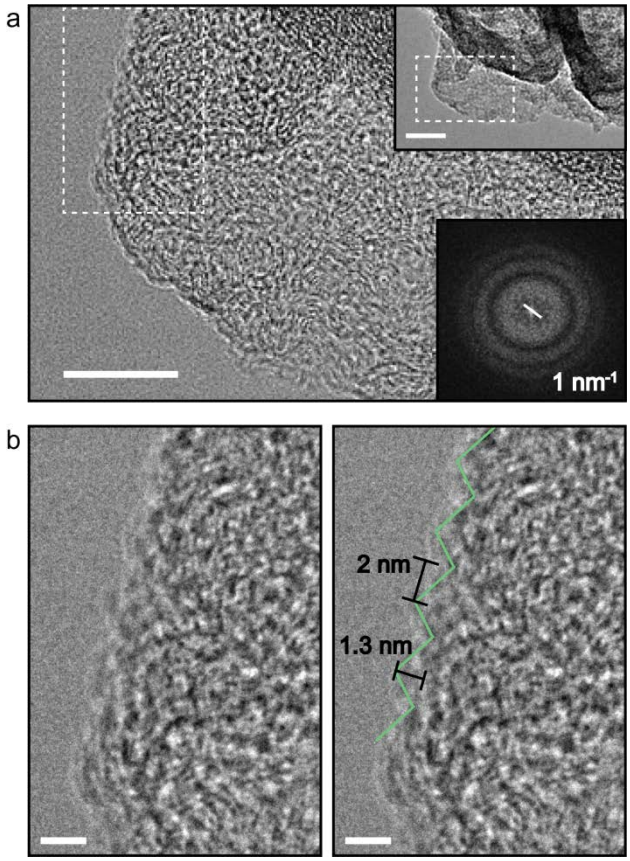

Figure 5.8 a) HRTEM of a nanosheet, scale bar 10 nm. Inset top, lower magnification, scale bar 20 nm. Inset bottom, Fourier transform pattern showing spots at 1 nm^{-1}. b) Higher magnification of a) showing zig-zag edge with corrugations of 1.3 nm depth and a lateral peak-to-trough distance of 2 nm, scale bar 2 nm.

We, hence, speculate that the reductive exfoliation process alters the in-plane crystal structure of the bismuth sulphide, by possibly introducing sulphur vacancies and allowing the ribbon-like units to interact in an alternate arrangement. The assumption regarding the presence of sulphur vacancies will

be further explored using XPS in section 5.3.2. These vacancies cause a repeating unit with corrugations of 1.3 nm along the c-axis, resulting in a monolayer with a uniform height of 2.4 nm and folded edges with double this height. The spacing between the corrugations is observed to be ~2 nm, and is identified as spots in the Fourier transform (Figure 5.8a inset) at a diameter of ~1 nm^{-1}. The observation of a repeating unit, with directionality, implies that the nanosheets would possess anisotropic properties and these will be studied in future investigations.

5.3.2 Composition

The exfoliated sheets were characterised and compared to the bulk starting material to determine the composition of the products. Photoluminescence was observed from the sheets when a 532 nm laser excitation was used. The emission shows a peak centered at 629 nm and a second, broader peak at 689 nm (Figure 5.9a). The observed photoluminescence is in the same energy range as previously reported luminescence from Bi_2S_3 nanobelts.[13] It has been suggested that crystal defects may create deep trap states that provide alternate recombination pathways resulting in the observed photoluminescence.[14-16] The intensity of the photoluminescence emission is directly proportional to the thickness of the material (see Figure 5.7b). We do not see enhanced emission for ultrathin regions, as has been reported for other two-dimensional materials.[4] This is probably due to the fact that the bulk material already possesses a direct bandgap, and thus no bandgap cross-over can be observed when the thickness of the crystal is reduced.

The Raman spectra (Figure 5.9b) show similar patterns for bulk Bi_2S_3 and thin layers. The peak locations closely match previously reported values,[17] the transverse A_g, in-plane, peaks occur at 188 and 240 cm^{-1}, and the longitudinal B_{1g} vibrations are at 168 and 265 cm^{-1}.[18] However, the relative peak intensity of the main B_{1g} peaks is increased in the exfoliated sample, which has previously been reported for Bi_2S_3 quantum dots.[19] This indicates that the longitudinal vibrations are altered compared to bulk crystals of Bi_2S_3.

An exfoliated sample dried on glass shows an XRD pattern that corresponds well to the bulk powder (Figure 5.9c). The broad feature between 15-35° is a background signal associated with the glass

substrate. All peaks are indexed to crystal planes of orthorhombic Bi_2S_3 (JCPDS 17-0320). The bulk material features major contributions from (130), (310) and (020) peaks. The exfoliated material is expected to show preferential orientation in the (010) and parallel planes, which would increase the peak intensities for these directions. The absence of these intense peaks can be attributed to the highly wrinkled nature of the sheets when dried on a substrate, resulting in random orientation. Additionally, the overall peak intensities have significantly decreased for all peaks, which further confirms the distortion of the crystal lattice during the chemical exfoliation, in agreement with the HRTEM analysis.

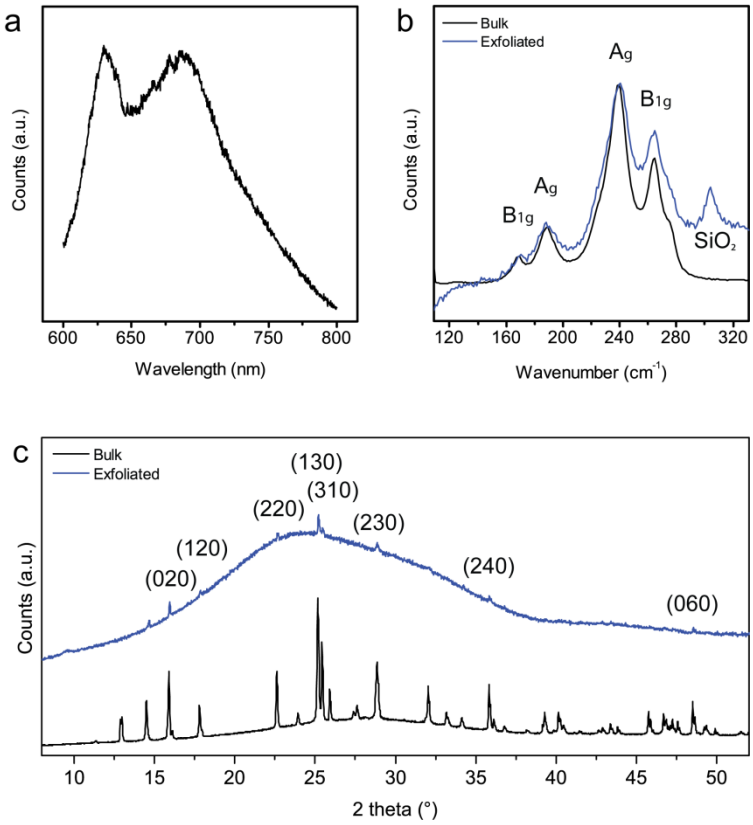

Figure 5.9 a) Photoluminescence spectrum of a sheet. b) Raman spectra of exfoliated and bulk material. c) XRD patterns of exfoliated and bulk material with main peaks indexed. Data has been normalised for ease of comparison.

The XPS data (Figure 5.10a) of the bulk Bi_2S_3 reference, measured between 145 and 175 eV binding energy, show a Bi 4f doublet with the S 2p doublet inside the Bi 4f doublet gap. These peaks were fitted for the bulk material (Figure 5.11a) and sensitivity factors were calibrated to yield the expected

Bi to S atomic ratio of 40:60 for Bi_2S_3. The atomic ratio of the precursor Bi_2S_3 material was confirmed using EDX during SEM imaging, giving a ratio of ~38:62, as shown in Figure 5.11b.

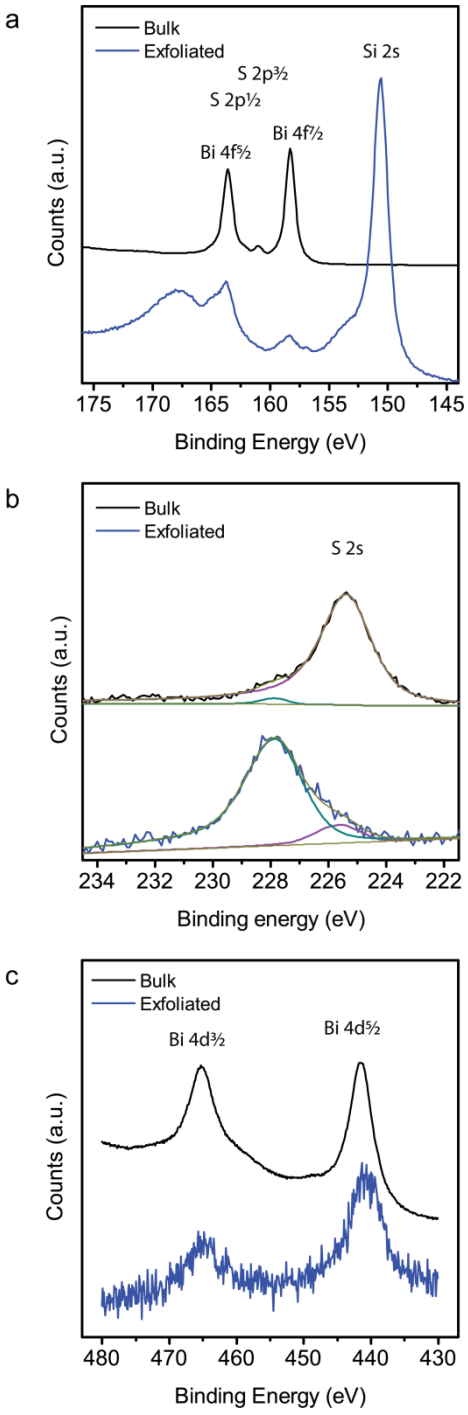

Figure 5.10 XPS binding energy windows for a) Bi 4f, b) S 2s and c) Bi 4d, for exfoliated (blue) and bulk material (black). Data has been normalised for ease of comparison.

For the exfoliated sample (Figure 5.10a, blue line), broadening of the Bi 4f peaks to higher binding energies indicates that some Bi in the sample exists in a sulphur-deficient state.[20] The stoichiometric

analysis of the sample is found to be complicated due to the overlapping of the Bi 4f and S 2p peaks which are also found to be comparatively weak. Furthermore, interference from the substrate's Si 2s signal is observed. As a result, it is inaccurate to use this energy window for peak fitting.

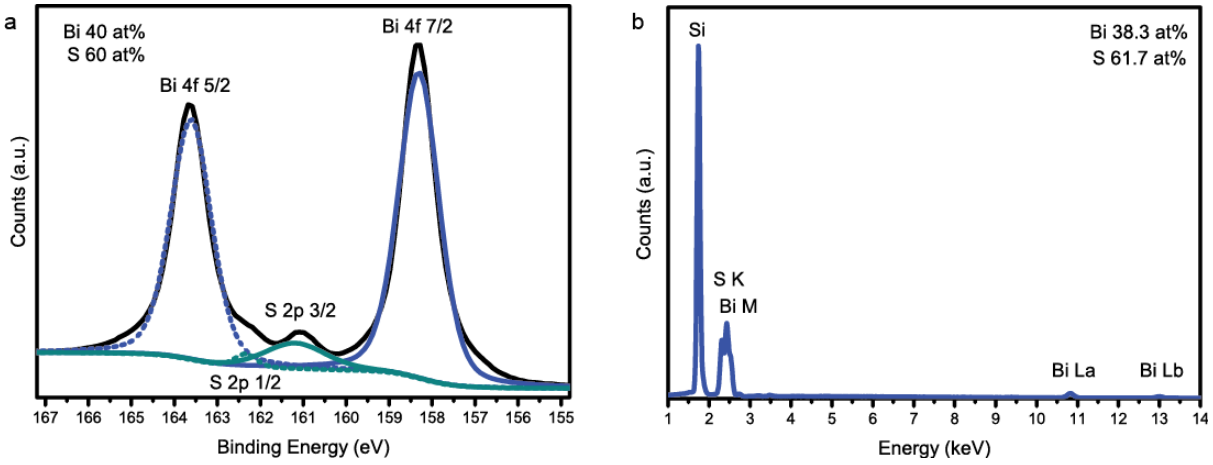

Figure 5.11 Bulk material a) XPS and b) EDX atomic percentage calculations.

As an alternative, the less prominent S 2s and Bi 4d energy windows (Figure 5.10b and c) are used, since these peaks are found to be more defined while not being affected by any overlapping signals from other elements. The S 2s peak corresponding to elemental sulphur at 227.9 eV (green line) and the Bi_2S_3 S 2s peak at 225.6 eV (purple line) are fitted, and the peak corresponding to Bi_2S_3 is used for the atomic ratio calculation.[21-24] Oxidation of the material is ruled out by closer observation of the O 1s region and extended Raman spectrum (Figure 5.12). The Raman spectrum does not show any evidence of peaks at 450 or 530 cm^{-1} which would indicate the presence of Bi_2O_3.[25, 26] Moreover, the symmetrical O 1s peak is assigned to the SiO_2 substrate with no evidence of a shoulder or peak at higher energy levels, which would be observed for Bi_2O_2S and Bi_2O_3.[27-29] The Bi 4d doublet is also integrated and the atomic ratio between Bi and S in the exfoliated material is found to be 43:57, corresponding to a chemical formula of $Bi_2S_{2.6}$. This indicates that the product is not fully stoichiometric Bi_2S_3, but rather that there is a large amount of sulphur vacancies introduced to the sheets during the exfoliation process. The lost sulphur atoms are likely reduced to elemental sulphur during the hydrazine based exfoliation procedure, giving rise to the associated distinct XPS signal (Figure 5.10b) and potentially the observed residues mentioned in the SEM discussion.

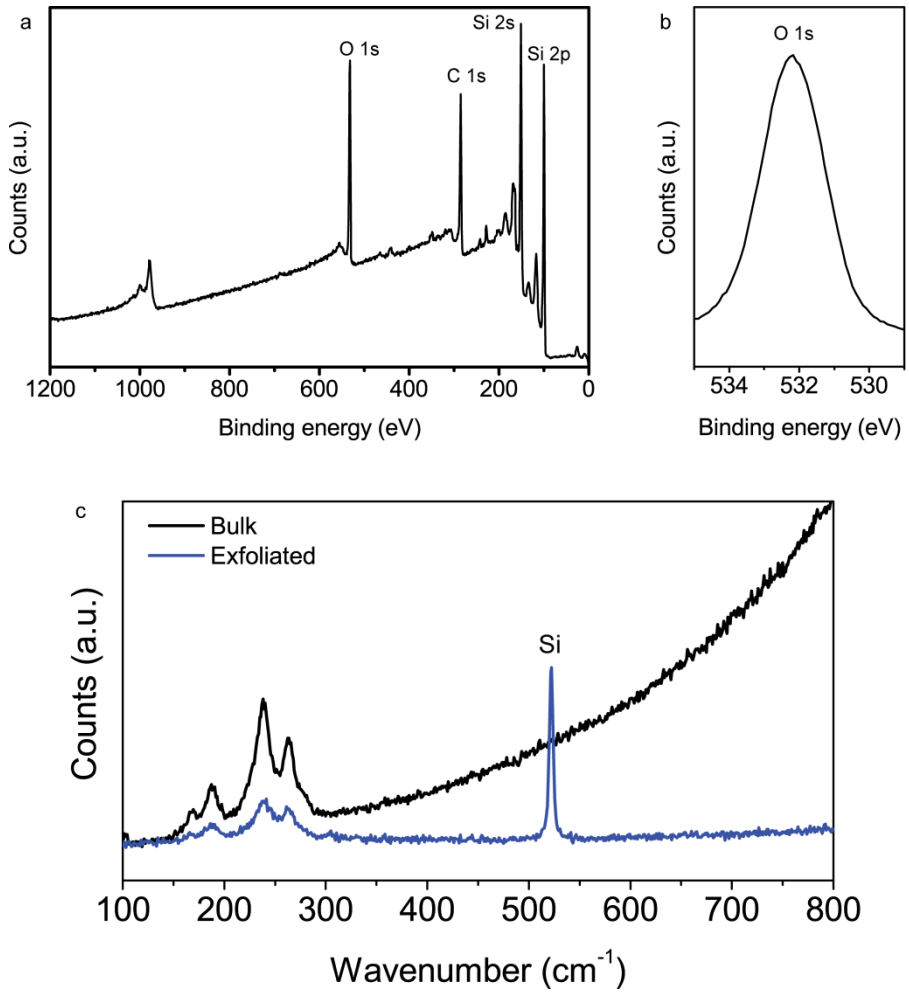

Figure 5.12 a) Survey XPS and b) O 1s energy region for exfoliated nanosheets. c) Extended Raman specta, showing no signs of Bi_2O_3 peaks at 450 or 530 cm^{-1}.

The determined elemental ratio indicates that most fundamental building blocks of the ribbon structure (Figure 5.13c) have lost one sulphur atom. The loss of one sulphur atom per bismuth sulphide unit provides a suitable hypothesis for the origin of the observed corrugated 2D sheet formation. If the sulphur loss preferentially involved the terminal sulphur atoms (highlighted in Figure 5.13d), cross linking of the individual ribbons and 2D sheet formation can be rationalised due to the formation of sulphur bridges. The van der Waals gap in c-axis direction is only 3.16 Å wide while the distance between the nanoribbons in the a-axis is 3.45 Å. The sulphur to bismuth bond lengths in bulk Bi_2S_3 are found to be between 2.5 Å and 3.0 Å and predominantly between 2.5 Å and 3.2 Å in simulated quantum confined Bi_2S_3 systems, indicating that 2D cross linking rather than the formation

of a three dimensional system is preferred.[30] As previously discussed, these vacancies, in combination with the formation of sheets, are the possible causes of the in-plane corrugation.

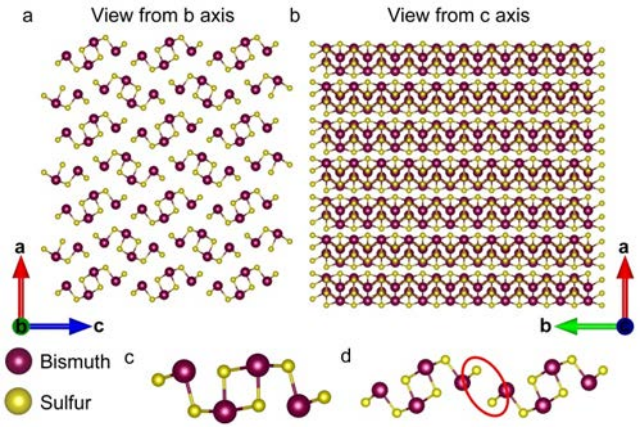

Figure 5.13 Crystal structure of Bi_2S_3,[31] a) view from the b axis showing the cross-section of the individual ribbons, b) view from the c axis highlighting the layered structure, c) structure of one individual Bi_2S_3 unit and d) structure of two neighbouring Bi_2S_3 ribbons. The red circle indicates the location where the loss of one sulphur atom could lead to the cross-linking of individual ribbons resulting in sheet formation, as discussed in the context of the XPS analysis.

The presence of Bi ions in the reaction mixture (as indicated in the Experimental section by the formation of BiOCl) along with the altered atomic ratio, suggests that the harsh reaction conditions cause some breakdown of the material during the exfoliation process. This resulting substoichiometry is consistent with previous characterisation of hydrazine assisted exfoliation of MoS_2.[1]

5.3.3 Electrical properties

Back-gated devices were established to facilitate the electrical characterisation of the exfoliated sheets. Optical and SEM imaging (Figure 5.14) were employed to locate the dispersed nanosheets on a substrate after drop casting the suspension. Large sheets that lay reasonably flat on the pre-patterned SiO_2/Si substrate are selected for electrode deposition. The thinnest and flattest part of the sheets were identified and measured with respect to the markers and EBL was used to pattern the electrodes, an example of which is shown in Figure 5.15a. A total of four operational structures was fabricated which displayed consistent properties. The location was then studied by AFM (Figure 5.15b) to determine the thickness of the sheet, wrinkles and also to confirm the height of the Au/Ti electrodes.

The sheet was found to be ~3 nm thick, with wrinkles reaching 6 nm of height (Figure 5.15c). This indicates that the electrical measurements were collected for single layer sheets.

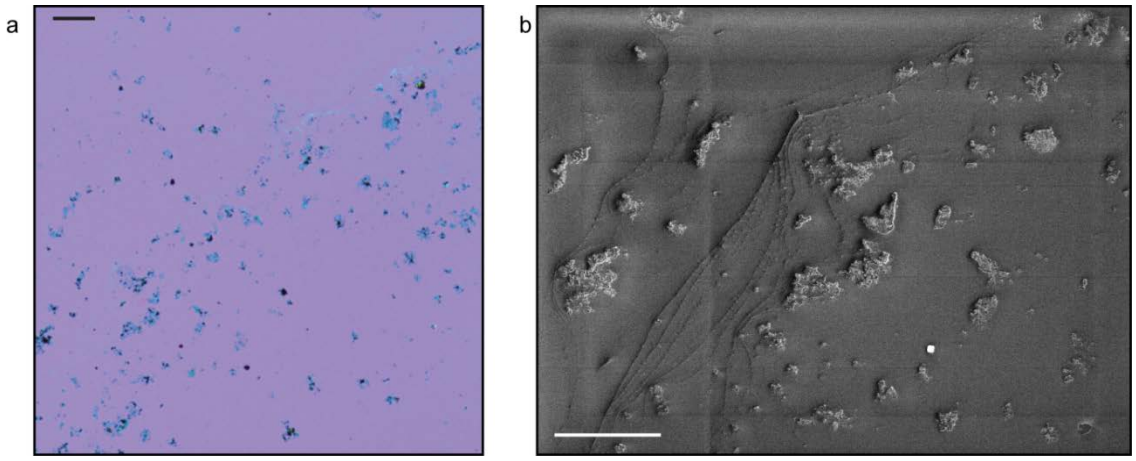

Figure 5.14 Low magnification images of the dropcasted suspension: a) Optical and b) SEM at the scale bars of 100 µm. It is easiest to use optical microscopy to see the contrast between thin nanosheets (blue) and thicker residues (black). In low magnification SEM, the thin sheets are not distinguishable from the substrate. Using a marked substrate and identifying flat nanosheets by optical microscopy, then locating the same region by high magnification SEM is necessary to obtain suitable SEM images of ultrathin sheets (as seen in Figure 5.7).

The devices were measured with various applied back-gate voltages and the current-voltage (I-V) curves were collected across the drain (an example is presented in Figure 5.15d). Non-ohmic contacts are observed, likely due to the chemical processing of the nanosheets, resulting in mobilities limited to the order of 10^{-3} cm^2/Vs. The enhanced current at negative gate voltage suggests that the sample has p-type nature. Bi_2S_3 is usually reported as an n-type material,[32, 33] and this p-doping is likely due to altered properties resulting from chemical preparation of the sheets and the resulting substoichiometry. The sample displays weak transconductance and does not switch off at gate voltages up to 80 V, where leakage typically occurs, indicating metallic doping of the material. Reports of metal-like conduction in substoichiometric Bi_2S_3 have attributed this phenomenon to sulphur vacancies in the material.[34-36] Annealing substoichiometric Bi_2S_3 in a sulphur atmosphere was shown to decrease the electrical conductivity by reducing the carrier concentration, as a result of the reduced number of sulphur vacancies.[36] In order to improve the materials performance in logic devices, more work should be carried out, to improve the contacts and to also tune the material's sulphur content in order to obtain a higher mobility in this p-type material.

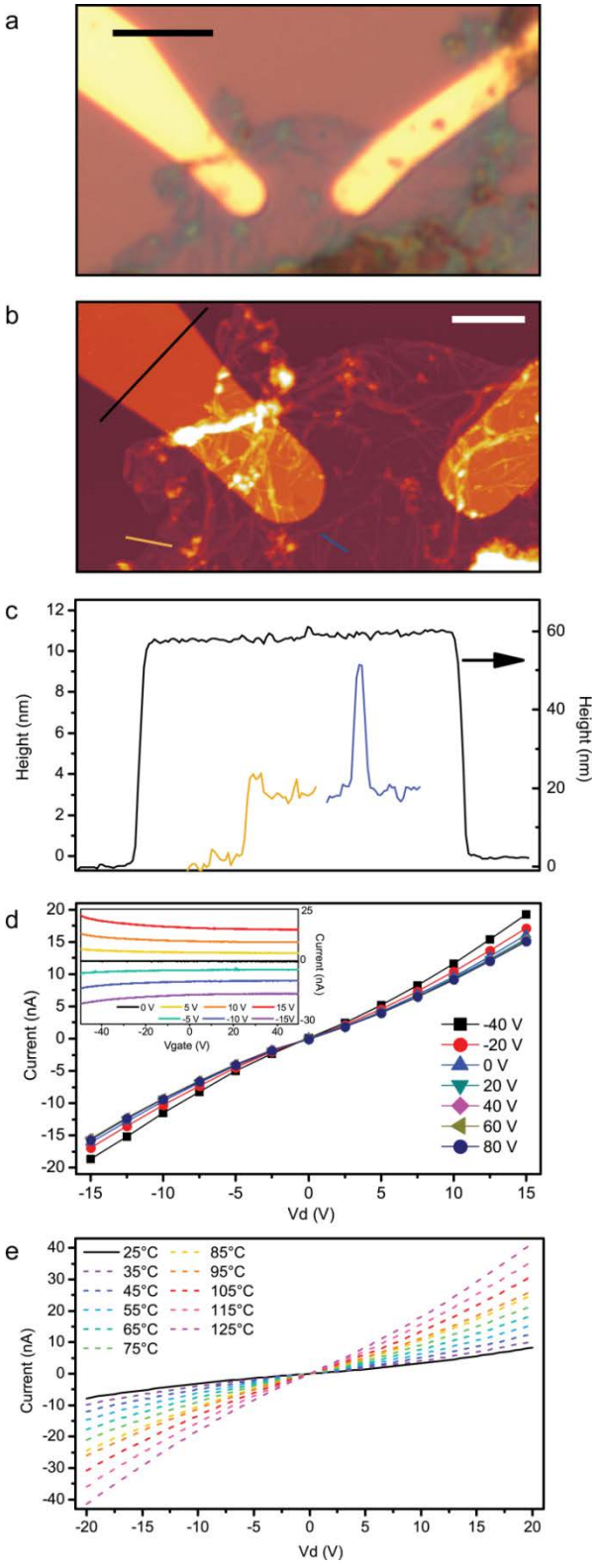

Figure 5.15 Electrodes deposited on an exfoliated nanosheet. a) Optical image, scale bar 5 µm. b) AFM image of the same device, scale bar 2 µm. c) Height profiles of lines in b), showing thicknesses of the sheet, wrinkles and electrodes. d) I-V curves of device using various applied gate voltages. Inset, I-Vgate curves of device with various drain voltages. e) I-V curves of device at various temperatures.

To further investigate the electrical properties of the nanosheets, the valence band position and Fermi level of the material were determined using PESA and valence XPS investigation (Figure 5.16). PESA found the material's valence band position to be 5.2 eV. This is consistent with the reported value of 5.13 eV, calculated for the (010) surface of Bi_2S_3.[37] The extremely small gap between the Fermi level and the valence band (~0.1 eV) indicates the presence of excess holes in the valence band and is indicative of high p-doping, which is in agreement with the electrical measurements.

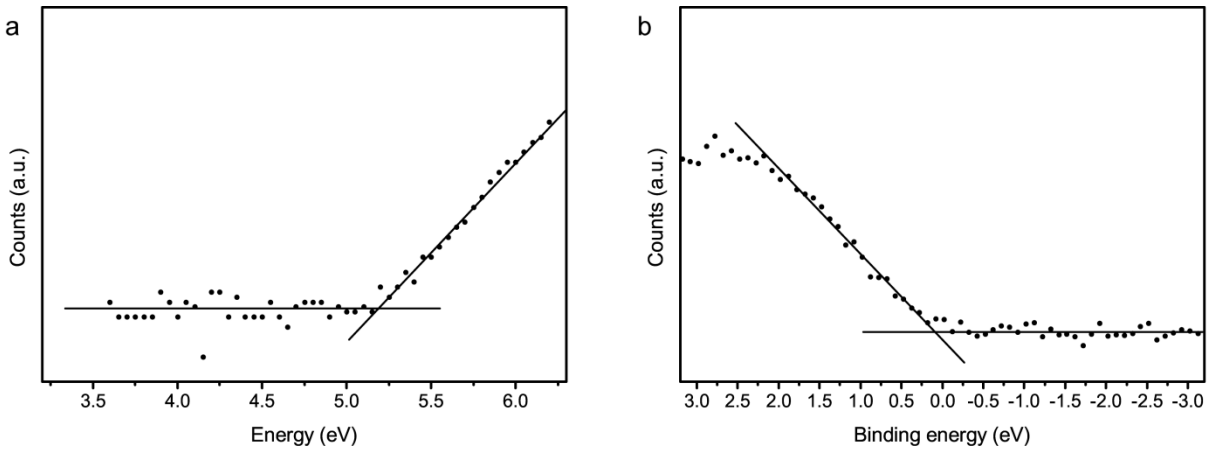

Figure 5.16 a) PESA and b) valence XPS of nanosheets.

The device's response to elevated temperature was also studied. I-V curves collected from 25-125°C (Figure 5.15e) show that the current increases near-linearly with increasing temperature. This translates into a negative temperature co-efficient where the resistivity changes from ~290 to ~55 Ωcm^{-1} when the temperature is increased from 25°C up to 125°C. This order of change in resistivity with temperature is comparable to that reported previously for n-type Bi_2S_3.[34] The change in resistivity is relatively linear which means that the device can be efficiently used for room temperature sensing applications.

5.3.4 Gas sensing

The device was also investigated for the use as a room temperature gas sensor. The I-V curve was collected, at room temperature, before and after exposure to 10 ppm NO_2 for 15 minutes (Figure 5.17). The I-V curve indicates an increased conductivity of the nanosheet, leading to an increased current by a response factor of 1.8 after exposure to NO_2 gas. The increase in conductivity with

adsorbed NO_2 is observed since the material is a p-type semiconductor and NO_2 acts as an electron acceptor.[38] The sensor shows a fast response, but a slow recovery, as highlighted in Figure 5.18.

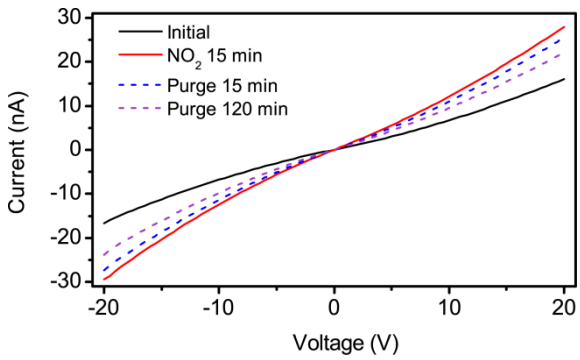

Figure 5.17 I-V curve of device before (black) and after (red) exposure to NO_2 gas for 15 minutes at room temperature and subsequent purging (dashed).

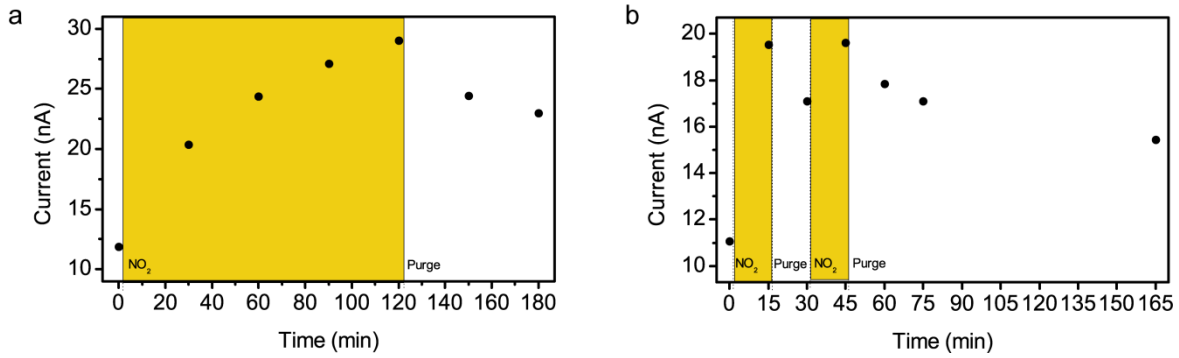

Figure 5.18 Sensor's current response to NO_2 gas over time a) long time exposure to gas and b) shorter term on-off exposures to gas.

After purging the sample for two hours with synthetic air, the device still showed an elevated conductivity. This slow recovery time indicates that the gas molecules strongly interact with the device and the adsorption is not quickly reversed. However, when measured after resting overnight, the device completely returned to its original state, which shows that no permanent bonding between the gas and the device occurred and that the nature of the interaction is probably physisorption. Similar slow recovery times are widely reported for other forms of physisorption based NO_2 sensors including two-dimensional MoS_2 and carbon based devices. [39, 40]

Bi_2S_3 nanowires and WS_2 nanosheets have shown promise as humidity sensors.[41, 42] As such, the sensor's response to water vapor was also investigated, to determine if the humidity of the

environment will interfere with the sensor's response to NO_2 gas. The current signal was found to decrease on the transition from a dry environment to 50% relative humidity, as shown in Figure 5.19. This indicates that the sensor may show a weaker signal when measured in a humid environment, but the humidity will not interfere to give a false-positive response to NO_2 gas.

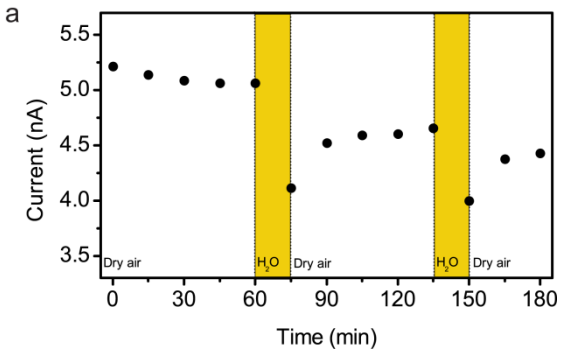

Figure 5.19 Sensor's current response to water vapour over time.

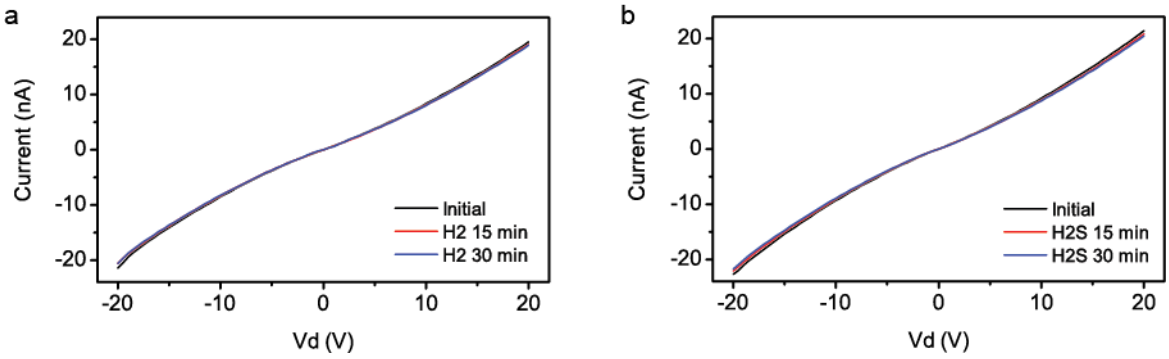

Figure 5.20 Selectivity for NO_2: nearly no response to a) H_2 and b) H_2S.

A previous report on gas sensing using a Bi_2S_3 nanowire shows moderate response and recovery time for interaction with H_2 gas.[43] As such, our sensor was also exposed to H_2 and H_2S gases, however, no response was detected (Figure 5.20). This discrepancy is attributed to the way the gases interact with the two different materials. Yao *et al.*[43] use n-type one-dimensional nanowires and do not report sulphur vacancies in their material. Hence, it is predicted that our material does not interact with H_2 due to the different structure of the used bismuth sulphide based materials. Furthermore, these measurements indicate that substoichiometric p-type nanosheets have a good selectivity for NO_2 gas sensing.

5.4 Conclusions

A new two-dimensional form of bismuth sulphide was developed, using a hydrazine salt based liquid phase exfoliation process. Since no mechanical force was required during this process, micron-scale ultrathin corrugated nanosheets could be obtained, despite the fact that the ribbon-like entities are held together by weak van der Waals forces along the planar structures in the bulk sample. The synthesised corrugated sheets were as large as 20 µm across and as thin as 2.5 nm. Sulphur vacancies introduced during the exfoliation process altered the stoichiometry of the material, resulting in a chemical formula of $Bi_2S_{2.6}$. The loss of sulphur atoms likely facilitated the cross linking of the individual bismuth sulphide ribbons, leading to the formation and exfoliation of corrugated 2D nanosheets. Further work on the characterisation of the highly anisotropic material is expected to show interesting altered properties along the corrugations. A metallic electrical response, with weak transconductance, was displayed and hence, future studies will investigate means to control the sulphur content to tune the material's electronic properties. A near-linear response to temperatures from 25-125°C highlights the potential use of this material in temperature measurement systems. The material also showed promise as a selective NO_2 gas sensor, with a fast response time and a response factor of 1.8. This is a first report on hydrazine salt assisted exfoliation of a highly ordered compound into corrugated planes, despite the fact that the precursor crystal was not naturally made of uniform covalently bound fundamental planes. The method can be adopted for the formation of future planar morphologies from crystals that are only quasi-stratified and, hence, lead to many novel possibilities in exfoliation processes for new two-dimensional materials.

In the following chapter, I discuss potential future studies that would build on the work presented in this thesis.

5.5 References

1. Daeneke, T.; Clark, R. M.; Carey, B.; Ou, J. Z.; Weber, B.; Fuhrer, M. S.; Bhaskaran, M.; Kalantar-zadeh, K. Reductive exfoliation of substoichiometric MoS_2 bilayers using hydrazine salts. *Nanoscale* **2016,** 8, 15252-15261.

2. Coleman, J. N.; Lotya, M.; O'Neill, A.; Bergin, S. D.; King, P. J.; Khan, U.; Young, K.; Gaucher, A.; De, S.; Smith, R. J.; Shvets, I. V.; Arora, S. K.; Stanton, G.; Kim, H.-Y.; Lee, K.; Kim, G. T.; Duesberg, G. S.; Hallam, T.; Boland, J. J.; Wang, J. J.; Donegan, J. F.; Grunlan, J. C.; Moriarty, G.; Shmeliov, A.; Nicholls, R. J.; Perkins, J. M.; Grieveson, E. M.; Theuwissen, K.; McComb, D. W.; Nellist, P. D.; Nicolosi, V. Two-Dimensional Nanosheets Produced by Liquid Exfoliation of Layered Materials. *Science* **2011,** 331, 568-571.

3. Nguyen, E. P.; Carey, B. J.; Daeneke, T.; Ou, J. Z.; Latham, K.; Zhuiykov, S.; Kalantar-zadeh, K. Investigation of Two-Solvent Grinding-Assisted Liquid Phase Exfoliation of Layered MoS_2. *Chem. Mater*. **2015,** 27, 53-59.

4. Mak, K. F.; Lee, C.; Hone, J.; Shan, J.; Heinz, T. F. Atomically Thin MoS_2: A New Direct-Gap Semiconductor. *Phys. Rev. Lett.* **2010,** 105, 136805.

5. Gan, Z. X.; Liu, L. Z.; Wu, H. Y.; Hao, Y. L.; Shan, Y.; Wu, X. L.; Chu, P. K. Quantum confinement effects across two-dimensional planes in MoS_2 quantum dots. *Appl. Phys. Lett.* **2015,** 106, 233113.

6. Eda, G.; Yamaguchi, H.; Voiry, D.; Fujita, T.; Chen, M.; Chhowalla, M. Photoluminescence from Chemically Exfoliated MoS_2. *Nano Lett.* **2011,** 11, 5111-5116.

7. Zheng, J.; Zhang, H.; Dong, S.; Liu, Y.; Tai Nai, C.; Suk Shin, H.; Young Jeong, H.; Liu, B.; Ping Loh, K. High yield exfoliation of two-dimensional chalcogenides using sodium naphthalenide. *Nat. Commun.* **2014,** 5, 2995.

8. Chen, G.; Yu, Y.; Zheng, K.; Ding, T.; Wang, W.; Jiang, Y.; Yang, Q. Fabrication of Ultrathin Bi_2S_3 Nanosheets for High-Performance, Flexible, Visible–NIR Photodetectors. *Small* **2015,** 11, 2848-2855.

9. Clark, R. M.; Kotsakidis, J. C.; Weber, B.; Berean, K. J.; Carey, B. J.; Field, M. R.; Khan, H.; Ou, J. Z.; Ahmed, T.; Harrison, C. J.; Cole, I. S.; Latham, K.; Kalantar-zadeh, K.; Daeneke, T. Exfoliation of Quasi-Stratified Bi_2S_3 Crystals into Micron-Scale Ultrathin Corrugated Nanosheets. *Chem. Mater.* **2016,** 28, 8942-8950.

10. Pereira, V. M.; Castro Neto, A. H.; Liang, H. Y.; Mahadevan, L. Geometry, Mechanics, and Electronics of Singular Structures and Wrinkles in Graphene. *Phys. Rev. Lett.* **2010,** 105, 156603.

11. Deng, S.; Berry, V. Wrinkled, rippled and crumpled graphene: an overview of formation mechanism, electronic properties, and applications. *Mater. Today* **2016,** 19, 197-212.

12. Aresti, M.; Saba, M.; Piras, R.; Marongiu, D.; Mula, G.; Quochi, F.; Mura, A.; Cannas, C.; Mureddu, M.; Ardu, A.; Ennas, G.; Calzia, V.; Mattoni, A.; Musinu, A.; Bongiovanni, G. Colloidal Bi_2S_3 Nanocrystals: Quantum Size Effects and Midgap States. *Adv. Funct. Mater.* **2014,** 24, 3341-3350.

13. Salavati-Niasari, M.; Ghanbari, D.; Davar, F. Synthesis of different morphologies of bismuth sulfide nanostructures via hydrothermal process in the presence of thioglycolic acid. *J. Alloys Compd.* **2009,** 488, 442-447.

14. Sträter, H.; ten Haaf, S.; Brüggemann, R.; Jakob, G.; Nilius, N.; Bauer, G. H. Detailed photoluminescence study of vapor deposited Bi_2S_3 films of different surface morphology. *Phys. Status Solidi B* **2014,** 251, 2247-2256.

15. Reshchikov, M. A.; Morkoç, H. Luminescence properties of defects in GaN. *J. Appl. Phys.* **2005,** 97, 061301.

16. Xiong, G.; Pal, U.; Serrano, J. G. Correlations among size, defects, and photoluminescence in ZnO nanoparticles. *J. Appl. Phys.* **2007,** 101, 024317.

17. Lu, F.; Li, R.; Li, Y.; Huo, N.; Yang, J.; Li, Y.; Li, B.; Yang, S.; Wei, Z.; Li, J. Improving the Field-Effect Performance of Bi_2S_3 Single Nanowires by an Asymmetric Device Fabrication. *ChemPhysChem* **2015,** 16, 99-103.

18. Zhao, Y.; Chua, K. T. E.; Gan, C. K.; Zhang, J.; Peng, B.; Peng, Z.; Xiong, Q. Phonons in Bi_2S_3 nanostructures: Raman scattering and first-principles studies. *Phys. Rev. B* **2011,** 84, 205330.

19. Zumeta-Dubé, I.; Ortiz-Quiñonez, J.-L.; Díaz, D.; Trallero-Giner, C.; Ruiz-Ruiz, V.-F. First Order Raman Scattering in Bulk Bi_2S_3 and Quantum Dots: Reconsidering Controversial Interpretations. *J. Phys. Chem. C* **2014,** 118, 30244-30252.

20. Bernechea, M.; Cao, Y.; Konstantatos, G. Size and bandgap tunability in Bi_2S_3 colloidal nanocrystals and its effect in solution processed solar cells. *J. Mater. Chem. A* **2015,** 3, 20642-20648.

21. Grigas, J.; Talik, E.; Lazauskas, V. X-ray Photoelectron Spectra and Electronic Structure of Bi_2S_3 Crystals. *Phys. Status Solidi B* **2002,** 232, 220-230.

22. Malakooti, R.; Cademartiri, L.; Akçakir, Y.; Petrov, S.; Migliori, A.; Ozin, G. A. Shape-Controlled Bi_2S_3 Nanocrystals and Their Plasma Polymerization into Flexible Films. *Adv. Mater.* **2006,** 18, 2189-2194.

23. Gao, X.; Huang, G.; Gao, H.; Pan, C.; Wang, H.; Yan, J.; Liu, Y.; Qiu, H.; Ma, N.; Gao, J. Facile fabrication of Bi_2S_3/SnS_2 heterojunction photocatalysts with efficient photocatalytic activity under visible light. *J. Alloys Compd.* **2016,** 674, 98-108.

24. Liufu, S.-C.; Chen, L.-D.; Yao, Q.; Wang, C.-F. Bismuth Sulfide Thin Films with Low Resistivity on Self-Assembled Monolayers. *J. Phys. Chem. B* **2006,** 110, 24054-24061.

25. Moniz, S. J. A.; Blackman, C. S.; Carmalt, C. J.; Hyett, G. MOCVD of crystalline Bi_2O_3 thin films using a single-source bismuth alkoxide precursor and their use in photodegradation of water. *J. Mater. Chem.* **2010,** 20, 7881-7886.

26. Vila, M.; Diaz-Guerra, C.; Lorenz, K.; Piqueras, J.; Alves, E.; Nappini, S.; Magnano, E. Structural and luminescence properties of Eu and Er implanted Bi_2O_3 nanowires for optoelectronic applications. *J. Mater. Chem. C* **2013,** 1, 7920-7929.

27. Zhang, X.; Liu, Y.; Zhang, G.; Wang, Y.; Zhang, H.; Huang, F. Thermal Decomposition of Bismuth Oxysulfide from Photoelectric Bi_2O_2S to Superconducting $Bi_4O_4S_3$. *ACS Appl. Mater. Interfaces* **2015,** 7, 4442-4448.

28. Pacquette, A. L.; Hagiwara, H.; Ishihara, T.; Gewirth, A. A. Fabrication of an oxysulfide of bismuth Bi_2O_2S and its photocatalytic activity in a Bi_2O_2S/In_2O_3 composite. *J. Photochem. Photobiol., A* **2014,** 277, 27-36.

29. Weng, B.; Xu, F.; Xu, J. Synthesis of hierarchical $Bi_2O_3/Bi_4Ti_3O_{12}$ p-n junction nanoribbons on carbon fibers from (001) facet dominated TiO_2 nanosheets. *RSC Adv.* **2014,** 4, 56682-56689.

30. Calzia, V.; Malloci, G.; Bongiovanni, G.; Mattoni, A. Electronic Properties and Quantum Confinement in Bi_2S_3 Ribbon-Like Nanostructures. *J. Phys. Chem. C* **2013,** 117, 21923-21929.

31. *Bi_2S_3 Crystal Structure: Datasheet from "LINUS PAULING FILE Multinaries Edition – 2012" in SpringerMaterials (http://materials.springer.com/isp/crystallographic/docs/sd_1921795)*, Springer-

Verlag Berlin Heidelberg & Material Phases Data System (MPDS), Switzerland & National Institute for Materials Science (NIMS), Japan.

32. Chmielowski, R.; Péré, D.; Bera, C.; Opahle, I.; Xie, W.; Jacob, S.; Capet, F.; Roussel, P.; Weidenkaff, A.; Madsen, G. K. H.; Dennler, G. Theoretical and experimental investigations of the thermoelectric properties of Bi_2S_3. *J. Appl. Phys.* **2015,** 117, 125103.

33. Song, H.; Zhan, X.; Li, D.; Zhou, Y.; Yang, B.; Zeng, K.; Zhong, J.; Miao, X.; Tang, J. Rapid thermal evaporation of Bi_2S_3 layer for thin film photovoltaics. *Sol. Energy Mater. Sol. Cells* **2016,** 146, 1-7.

34. Liufu, S.-C.; Chen, L.-D.; Yao, Q.; Wang, C.-F. Assembly of one-dimensional nanorods into Bi_2S_3 films with enhanced thermoelectric transport properties. *Appl. Phys. Lett.* **2007,** 90, 112106.

35. Chen, B.; Uher, C.; Iordanidis, L.; Kanatzidis, M. G. Transport Properties of Bi_2S_3 and the Ternary Bismuth Sulfides $KBi_{6.33}S_{10}$ and $K_2Bi_8S_{13}$. *Chem. Mater.* **1997,** 9, 1655-1658.

36. Mizoguchi, H.; Hosono, H.; Ueda, N.; Kawazoe, H. Preparation and electrical properties of Bi_2S_3 whiskers. *J. Appl. Phys.* **1995,** 78, 1376-1378.

37. Zhao, Y.; Zhu, X.; Huang, Y.; Wang, S.; Yang, J.; Xie, Y. Synthesis, Growth Mechanism, and Work Function at Highly Oriented {001} Surfaces of Bismuth Sulfide Microbelts. *J. Phys. Chem. C* **2007,** 111, 12145-12148.

38. Ou, J. Z.; Ge, W.; Carey, B.; Daeneke, T.; Rotbart, A.; Shan, W.; Wang, Y.; Fu, Z.; Chrimes, A. F.; Wlodarski, W.; Russo, S. P.; Li, Y. X.; Kalantar-zadeh, K. Physisorption-Based Charge Transfer in Two-Dimensional SnS_2 for Selective and Reversible NO_2 Gas Sensing. *ACS Nano* **2015,** 9, 10313-10323.

39. Donarelli, M.; Prezioso, S.; Perrozzi, F.; Bisti, F.; Nardone, M.; Giancaterini, L.; Cantalini, C.; Ottaviano, L. Response to NO_2 and other gases of resistive chemically exfoliated MoS_2-based gas sensors. *Sens. Actuators, B* **2015,** 207, 602-613.

40. Iqbal, N.; Afzal, A.; Cioffi, N.; Sabbatini, L.; Torsi, L. NO_x sensing one- and two-dimensional carbon nanostructures and nanohybrids: Progress and perspectives. *Sens. Actuators, B* **2013,** 181, 9-21.

41. Kunakova, G.; Meija, R.; Bite, I.; Prikulis, J.; Kosmaca, J.; Varghese, J.; Holmes, J. D.; Erts, D. Sensing properties of assembled Bi_2S_3 nanowire arrays. *Phys. Scr.* **2015,** 90, 094017.

42. Mayorga-Martinez, C. C.; Ambrosi, A.; Eng, A. Y. S.; Sofer, Z.; Pumera, M. Metallic 1T-WS_2 for Selective Impedimetric Vapor Sensing. *Adv. Funct. Mater.* **2015,** 25, 5611-5616.

43. Yao, K.; Gong, W. W.; Hu, Y. F.; Liang, X. L.; Chen, Q.; Peng, L. M. Individual Bi_2S_3 Nanowire-Based Room-Temperature H_2 Sensor. *J. Phys. Chem. C* **2008,** 112, 8721-8724.

Chapter 6

Conclusions

6.1 Concluding remarks

The primary objectives of this PhD research, as outlined at the beginning of this thesis, were to develop new morphologies of metal sulphide nanomaterials and explore their unique properties. The contents of this thesis have contributed to knowledge regarding the liquid-phase synthesis of metal sulphide nanomaterials through investigation of safer, faster, more efficient and simpler reaction methods.

Various synthesis techniques were developed, fully investigated and optimised throughout this research, resulting in significant contribution to the advancement of the area of metal sulphide nanomaterials. Detailed discussions of the outcomes of the three separate stages of this project are as follows:

6.1.1 Stage 1

In this investigation, an aqueous exfoliation of MoS_2 was achieved through the use of a biocompatible surfactant. The exfoliated nanoflakes were further broken-down into quantum dots through a hydrothermal process, as well as simultaneous growth of ZnS to form hybrid quantum dots.

The photoluminescence intensity was shown to be lowest for large MoS_2 nanoflakes, the break-down to quantum dots increased the emission and the hybrid quantum dots were shown to have the greatest emission intensity. Incorporation of the ZnS introduced a second peak in the photoluminescence emission spectrum, with the peak height ratio dependent on the molar ratio of zinc precursor used in the hydrothermal reaction. The photoluminescence quantum yield was calculated to be 1.96%, which is higher than the emission for pristine monolayer MoS_2.

The photoluminescent emission was shown to be excitation-wavelength-independent, which indicates that the particles have a relatively narrow size distribution. This makes the developed hybrid quantum dots more useful, because the emission is much more stable and intense.

This work provided evidence that the optical emission from MoS_2 nanomaterials can be controlled and enhanced to useful levels by size confinement as well as through hybridisation. In addition, biocompatible methods of preparation can be achieved through use of aqueous surfactant solutions.

6.1.2 Stage 2

A facile alternative method for the formation of transition metal dichalcogenide (TMD) films has been developed. A fast sonication-assisted exfoliation was used for creating a stable suspension of TMD nanoflakes in dimethyl formamide, without incorporating any other chemicals or surfactants. A liquid-liquid assembly was then achieved by mixing octadecene directly with the suspension. The assembly was spontaneous, without the addition of any chemical initiators. Upon settling, the TMD nanoflakes were shown to assemble into an isolated film.

The application of a patterned hydrophobic coating on Si substrates created a desirable control over the films deposition behaviour. Large-scale uniform films have been established, with hydrophobic constraints to control the area of the patterned films.

The orientation of the nanoflakes was confirmed by x-ray diffraction analysis. The intensity of the basal plane 002 peak for both MoS_2 and WS_2 indicated that the flakes lay flat on the surface. Atomic force microscopy shows that the films were quite thin, however, there was a lot of roughness caused by small overlapping flakes. Ultimately the film quality could be improved by using a suspension of large ultrathin flakes, and the method is currently limited by the exfoliation process and the quality of the resulting nanoflake suspension.

The outcome of this stage was the introduction of a facile two-dimensional material assembly technique. It has been shown that it is not necessary to introduce additional chemical modification and processing steps in the manipulation of exfoliated nanoflake suspensions. In addition, substrate surface modification, through hydrophobic treatment, provides a useful tool for control over film patterning.

6.1.3. Stage 3

The final stage of this PhD thesis was focussed on producing micron-scale nanosheets from quasi-stratified crystals of bismuth sulphide (Bi_2S_3). Bi_2S_3 has been exfoliated for the first time, into a two-dimensional morphology.

During the reductive exfoliation, the isolated ribbons were cross-linked into two-dimensional sheets with sulphur vacancies. The stoichiometry of the resulting nanosheets was determined by x-ray photoelectron spectroscopy and calculated to be $Bi_2S_{2.6}$.

The sulphur vacancies in the material caused severely altered electrical properties, resulting in highly p-type behaviour with metallic conductivity. The material was shown to have a selective response to NO_2 gas, with no response detected from H_2S or H_2 gasses. The sensor showed a fast response and a slow recovery, which indicated that a reversible physisorption process occurs.

This stage introduced the possibility of exfoliation of quasi-stratified crystals, which usually form one-dimensional nanostructures. The new reductive exfoliation method presents a mechanically gentle alternative, which results in relatively large micron-scale nanosheets by preventing fracturing and break-down.

6.2 Future studies

The research presented in this thesis has contributed significant progress in the field, evidenced by the publication of several journal articles. As research interest in the field of metal sulphide nanomaterials continues to grow, this thesis provides a basis for several new branches of future investigations. The preliminary findings introduce scope for further studies based upon the outcomes of this research.

6.2.1 Hybrid quantum dots

Following work on the synthesis of hybrid quantum dots with enhanced photoluminescence, optical sensing applications should be further studied. In future, the sensitivity of the hybrid quantum dots in aqueous chemical sensing should be investigated. With the appearance of dual emission peaks, the option of internal calibration becomes a possibility.

It might also be possible to extend this investigation to incorporate different sulphide materials into new hybrid structures, by using different chemical precursors in the hydrothermal synthesis. A selection of new quantum dots covering a wide emission range, with selectivity to many ions, could help to create a broad spectrum optical sensor array.

6.2.2 Films made from two-dimensional flakes

The facile method for patterned film deposition is currently limited by the quality of the nanoflake suspension and also by the dip extraction process. Optimisation of the exfoliation process has been extensively studied in the past and a suitable solvent profile for exfoliation as well as liquid-liquid interface formation can be achieved. Future studies would ideally focus on making films with less grain boundaries, by incorporating large, ultrathin nanosheets.

It would also be useful to further introduce and study the behaviour of surfactant molecules in the exfoliation and assembly processes. Through the use of surfactants, the exfoliation can be enhanced, to produce a high yield of ultrathin nanosheets, however the properties of the resulting films could be altered and this would need thorough investigation and optimisation.

The deposition of the films, with incorporated two-dimensional flakes, should also be greatly improved by the incorporation of a robotic dip technique. As such, future studies on the optimisation of dip velocity and angle optimisation would be beneficial to the overall film formation.

If a uniform coverage is achieved, thin films could be deposited at targeted locations on a substrate. Future studies should include incorporation of these films into a range of devices and testing their suitability for use in catalysis, sensing and energy storage applications.

6.2.3 Ultrathin micron-scale nanosheets

The reductive exfoliation of stratified and quasi-stratified crystals has been shown to produce micron-scale ultrathin nanosheets. This process could be applicable to a wide variety of different sulphide materials, and future investigation of the method is thought to be highly relevant to the advancement of two-dimensional materials synthesis.

The conversion to substoichiometric material is also highly interesting for emerging applications. Further studies for maintaining control over the stoichiometry of the material could result in two-dimensional nanosheets with tuneable properties.

At this stage, the yield of the exfoliation is low. Future optimisation of the exfoliation process, to produce more highly concentrated suspensions of micron-scale nanosheets, is thought to be key to achieving solution processed nanosheets with quality comparable to chemical vapour deposited two-dimensional materials. If a high yield of micron-scale nanosheets is achieved, this would be an ideal candidate for incorporation into the liquid-liquid assembly process to produce large scale films with fewer overlapping boundaries.

6.3 List of publications

6.3.1 First-author publications

R. M. Clark, K. J. Berean, B. J. Carey, N. Pillai, T. Daeneke, I. S. Cole, K. Latham and K. Kalantar-zadeh, Patterned films from exfoliated two-dimensional transition metal dichalcogenides assembled at a liquid-liquid interface, *J. Mater. Chem. C*, 2017, 5, 6937-6944

R. M. Clark, J. C. Kotsakidis, B. Weber, K. J. Berean, B. J. Carey, M. R. Field, H. Khan, J. Z. Ou, T. Ahmed, C. J. Harrison, I. S. Cole, K. Latham, K. Kalantar-zadeh and T. Daeneke, Exfoliation of quasi-stratified Bi_2S_3 crystals into micron-scale ultrathin corrugated nanosheets, *Chem. Mater.*, 2016, 28, 8942-8950

R. M. Clark, B. J. Carey, T. Daeneke, P. Atkin, M. Bhaskaran, K. Latham, I. S. Cole and K. Kalantar-zadeh, Two-step synthesis of luminescent MoS_2-ZnS hybrid quantum dots, *Nanoscale*, 2015, 7, 16763-16772

6.3.2 Co-author publications

B. J. Carey, J. Z. Ou, **R. M. Clark**, K. J. Berean, A. Zavabeti, A. S. R. Chesman, S. P. Russo, D. W. M. Lau, Z.-Q. Xu, Q. Bao, O. Kevehei, B. C. Gibson, M. D. Dickey, R. B. Kaner, T. Daeneke and K. Kalantar-zadeh, Wafer-scale two-dimensional semiconductors from printed oxide skin of liquid metals, *Nat. Commun.*, 2017, 8, 14482

T. Daeneke, N. Dhar, P. Atkin, **R. M. Clark**, C. J. Harrison, R. Brkljaca, N. Pillai, B. Y. Zhang, A. Zavabeti, S. J. Ippolito, K. J. Berean, J. Z. Ou, M. S. Strano and K. Kalantar-zadeh, Surface water dependent properties of sulphur-rich molybdenum sulphides: Electrolyteless gas phase water splitting, *ACS Nano*, 2017, 11, 6782-6794

T. Daeneke, **R. M. Clark**, B. J. Carey, J. Z. Ou, B. Weber, M. S. Fuhrer, M. Bhaskaran and K. Kalantar-zadeh, Reductive exfoliation of substoichiometric MoS_2 bilayers using hydrazine salts, *Nanoscale*, 2016, 8, 15252-15261

Y. Wang, E. D. Gaspera, B. J. Carey, P. Atkin, K. J. Berean, **R. M. Clark**, I. S. Cole, Z.-Q. Xu, Y. Zhang, Q. Bao, J. Z. Ou, T. Daeneke and K. Kalantar-zadeh, Enhanced quantum efficiency from a mosaic of two dimensional MoS_2 formed onto aminosilane functionalised substrates, *Nanoscale*, 2016, 8, 12258-12266

P. Atkin, T. Daeneke, Y. Wang, B. J. Carey, K. J. Berean, **R. M. Clark**, J. Z. Ou, A. Trinchi, I. S. Cole and K. Kalantar-zadeh, 2D WS_2/carbon dot hybrids with enhanced photocatalytic activity, *J. Mater. Chem. A*, 2016, 4, 13563-13571